Seismic Risk Assessment of the Thin and Lightly Reinforced Concrete Wall Building System

by

Gustavo Adolfo Araújo Rodríguez

A thesis submitted in partial satisfaction of the
requirements for the
Master's degree in Civil Engineering
in the
Graduate Division
of the
Universidad del Norte, Barranquilla, Colombia

Advisor:
Professor Carlos A. Arteta

January 2021

Seismic Risk Assessment of the Thin and Lightly Reinforced Concrete Wall Building System

Abstract

Seismic Risk Assessment of the Thin and Lightly Reinforced Concrete Wall Building System

by

Gustavo Adolfo Araújo Rodríguez

Master's degree

in

Engineering – Civil and Environmental Engineering

University del Norte, Barranquilla, Colombia

Professor Carlos A. Arteta, Advisor

Industrialized construction of very thin and lightly reinforced concrete (RC) walls buildings is a common construction practice in Northern South America. RC walls are listed in many building codes (e.g., American Code ACI 318, Colombian Code NSR-10) as an acceptable lateral load-resisting system and are frequently used for buildings in regions of intermediate and high seismicity. However, the Colombian building typology is significantly different from the traditional ductile cast-in-place RC walls used in countries like the United States, New Zealand or even Chile. The Colombian thin-wall building typology comprises concrete walls with thickness in the range 80 mm $\leq t_w \leq$ 150 mm, reinforced with low reinforcement ratios ($\rho_l < 0.4\%$) and low axial load ($P \leq 0.10 f'_c A_g$), conforming the gravitational- and lateral-load resisting system. To hasten the construction process, non-ductile electro-welded meshes have replaced traditional reinforcing bars as longitudinal and transverse reinforcement. Until now, there has been no evidence from the field of the seismic behavior of these very thin RC wall systems to evaluate whether they perform as expected under the provisions of design codes like ACI 318 or the NSR-10 codes. However, recent experimental tests on isolated specimens suggest that thin RC walls have limited ductility capacity, with lower-than-expected performance. This study presents a methodology to assess the seismic risk of thin-wall building archetypes using nonlinear hazard-consistent dynamic analyses. A case study is presented with geometric features and reinforcement configuration of buildings compatible with the Colombian building typology in high-risk seismic zones. The seismic response of the structures is evaluated in terms of local (at the section level of the elements) and global (general behavior of the structure) deformation capacity and demand in the inelastic range. Analysis results are used to develop fragility curves and quantify the vulnerability and the seismic risk of such thin RC wall building systems.

To my parents and my sister,

for their support and trust in me.

Acknowledgments

First of all, I want to thank my parents Gustavo and Ela and my sister Daniela for all the support they gave me during my master's studies. They are my main motivation in life and I will never be able to repay them for all the sacrifices they have made for me since I was a child.

I am very grateful to Professor Carlos Arteta, who introduced me to the world of research and taught me everything I know about reinforced concrete structures. Professor Carlos became a second father to me, and together we carried out this research. I thank him for having been my guide, not only professionally, but also personally.

Among all the professors at Universidad del Norte who contributed to my professional development. I would like to make a special mention to Professor Andrés Guzmán. He was my professor of structural analysis in my undergraduate program. His course was the first step to start enjoying structural engineering.

I want to thank my friends from the Civil Engineering department: Melany Gil, Andrés Torregroza, Alexander Arciniegas, Oswaldo Guerrero, César Pájaro, Jefferson Piedrahita, Sebastián Quintero, Julio Sánchez, Carlos Canchila and Tayrin Hurtado. Thank you for providing a pleasant work space and collaborating so much. I appreciate all the times you helped me run the numerical simulations presented in this document.

I thank with all my heart Laura Ospina, who accompanied me throughout this process and gave me the encouragement I needed when everything seemed to be getting dark. I will always value her love and care.

Throughout my two years of studies I received financial support from many people and entities. When I was about to start my graduate studies, I was given a new computer to work with. The donors did not know me, but they had every intention of supporting a person with limited resources like me. I want to thank each one of them using the same pseudonyms with which they signed the gift card at that time: Hugol, El Flaco, Lotti, El Chato, Capi González, Omito and Charles. This research is also yours.

I would also like to thank Dr. Raimundo Abello, Carlos Clavijo, and the entire teams of the Project Management and the Research and Development offices at Universidad del Norte. My graduate studies were financed by two projects in collaboration with these departments.

This research would not have been possible without the financial support of Ingenia Structural Co. I thank Andrés Galán, legal representative of this company, for having trusted me. At Ingenia I was also able to put into practice the knowledge acquired with Professor Arteta. There were several projects in which I am proud to have participated.

The research presented in this thesis was also supported in part by the Escuela de Ingeniería de Antioquia, Universidad del Norte, Universidad de Medellín and Universidad Militar Nueva Granada through the INV-ING-2743 Project, which is carried out within the activities of the Colombian Earthquake Engineering Research Network (CEER). I also thank Computer and Structures, Inc. for providing an ETABS® license to conduct this

research. Opinions, findings, conclusions and recommendations in this document are those of the author and do not necessarily represent those of the sponsors.

Table of Contents

Table of Figures

Table of Tables

Introduction

Reinforced concrete (RC) walls are listed in many design codes (e.g., ACI 318) as an acceptable lateral load-resisting system and are frequently used in buildings in regions of moderate and high seismicity, especially in intermediate and high-rise buildings. In Colombia and other Latin American countries, the use of thin RC walls in residential buildings has been extended to conform both the architectural and structural layout (Carrillo & Alcocer, 2011; Gonzales & Lopez-Almansa, 2010; Mejia et al., 2004; Yañez, 2006). This system, known widespread as industrialized or tunnel form construction, allows the constructor engineer to reduce costs in finishes and hasten construction processes compared to traditional systems (Carrillo et al., 2015). With this objective in mind, over the years, engineers have opted for increasingly reduced wall thicknesses and low reinforcement steel ratios. Traditional ductile reinforcement is also typically replaced with cold-drawn wires of limited ductility. These buildings have been constructed in regions of low, moderate, and high seismicity in Colombia following NSR-10 provisions (Comité AIS 100, 2010). NSR-10 is the current version of the Colombian building code and its prescriptions for concrete design are adapted from ACI 318-08 (2008).

Experimental observations have shown that thin and lightly-reinforced RC wall buildings are vulnerable to high lateral displacements demands due to seismic action, especially when detailed with reinforcement of limited ductility (Blandón et al., 2018; Hube et al., 2014; Quiroz et al., 2013; Rosso et al., 2016). However, a comprehensive assessment of the seismic risk to which these structures are subjected requires that their structural vulnerability be contrasted with the seismic hazard at the site. Quantitatively, the seismic risk can be expressed as the product between the vulnerability and the seismic hazard (Wang, 2009). Considered in this way, the vulnerability of the industrialized thin RC wall building system does not necessarily imply that the associated seismic risk is high. For example, in Turkey, little damage was reported in buildings with an industrialized wall system similar to that used in Latin America during the Kocaeli (M_w 7.4) and Duzce (M_w 7.2) earthquakes in 1999 (Balkaya & Kalkan, 2004; Kalkan & Yüksel, 2008). In contrast, buildings with special structural walls exhibited undesirable modes of failure during the 2010 Chile (M_w 8.8) and 2011 New Zealand (M_w 6.2) earthquakes (Elwood et al., 2014; Jünemann et al., 2015; Wallace, 2012).

For the specific case of Colombia, no significantly large earthquake events have occurred in the past 20 years. The last significantly destructive earthquake event in Colombia was the M_w 6.1 Armenia earthquake in 1999, back when the thin RC wall building system was not popular in the country. To counteract this lack of evidence from the field, this article presents a methodology for evaluating the seismic risk of thin wall buildings based on the results of several numerical analyses. The proposed methodology stands out for consistently operating the seismic hazard and vulnerability to produce an objective quantification of the seismic risk.

As a case-study example, this study assesses the seismic performance of three archetype thin RC wall buildings integrating the results of nonlinear static and dynamic analyses in OpenSees (McKenna et al., 2010) in a hazard-consistent methodology. The geometric features and reinforcement configuration of the buildings are representative of

common Colombian construction practice for various ranges of building heights and wall thicknesses in high seismic hazard zones. The seismic response of the above-mentioned structures is evaluated in terms of local (at the section level of the elements) and global (general behavior of the structure) deformation capacity and demands in the inelastic range. Analysis results are used to develop fragility curves and quantify the vulnerability of thin RC wall building systems, as well as the probability of exceedance of different engineering demand parameters (EDP-risk).

Scope

This research discusses the limited rotation capacity of thin lightly reinforced walls with the aim of having a better understanding of its causes and implications in the seismic behavior of medium- and high-rise buildings. The discussion is opened with recent field and laboratory observations of damaged thin RC wall elements and ends with a risk-based assessment of the expected behavior of three Colombian-code-compliant thin RC wall building archetypes using a state-of-the-art methodology. The intention is to provide the engineering community with an understanding of the parameters that influence the seismic behavior of thin RC wall buildings and provide a practical methodology to quantify the risk of exceedance of certain engineering demand parameters (EDPs).

Objectives

The general objective of this investigation is to evaluate the vulnerability of thin RC wall buildings through a risk-based methodology. Three specific objectives are: (i) to propose a mathematical model able to reproduce the response of thin RC wall elements in laboratory, while keeping simplicity and numerical robustness; (ii) to define a seismicity model for the city of Armenia (site of interest for the study) in Colombia for risk-based assessment of RC structures implementing recent developments in performance-based earthquake engineering (PBEE); (iii) to investigate the implications of the limited ductility capacity of thin wall elements in the seismic response of mid- and high-rise RC wall buildings and (iv) to estimate their associated seismic vulnerability and risk in terms of EDP fragility and risk curves.

Organization

The thesis comprises seven chapters describing the seismic response of industrialized thin RC wall buildings. Recent laboratory data is analyzed to provide an insight on the performance limit states of thin RC walls. It also introduces a hazard-consistent methodology to assess the vulnerability and quantify the risk to which such systems are exposed.

Chapter 1 provides a description of the major characteristics of the thin RC wall building inventory in Colombia and discusses the provisions of the current Colombian building code for such systems. It also presents a database comprising tested wall panels with similar characteristics to the Colombian inventory. These experimental findings are used to estimate the performance limit state values of the walls that constitute the case-study lateral force-resisting system.

Chapter 2 introduces three different building archetypes representative of the Colombian inventory. These buildings are designed following the local NSR-10 regulation and typical engineering practice. The seismic response of these archetypes will be analyzed in the next chapters.

Chapter 3 presents a methodology to assess the vulnerability and quantify the seismic risk of thin RC wall buildings with a hazard-consistent basis. A seismic hazard model for the city of Armenia, where the archetypes are located, is proposed. Along with this hazard model, the Conditional Scenario Spectra (CSS) concept is extended to consider multiple types of source mechanisms and scenarios. The result is a set of ground motions that cover a wide range of intensities and are useful to perform structural fragility analysis. These ground motions also have assigned occurrence rates that allow for the direct estimation of annual rates of exceedance of any EDP of interest.

Chapter 4 proposes a simple 2D numerical model to simulate the nonlinear response of thin RC walls. The model is validated against experimental data from wall panels representative of the Colombian inventory.

Chapter 5 provides results from nonlinear static (pushover) analyses to estimate the overstrength and displacement capacity of the building archetypes in study. Damage is evaluated at the global and local level of response, identifying the onsets of material limit states and the localization of damage in the bottom story.

Chapter 6 presents the result of implementing the CSS methodology to compute the fragility curves and seismic risk of the building archetypes. The seismic risk is presented in terms of the annual rate of exceedance of specific EDPs and is contrasted against the design objectives of the Colombian Earthquake-Resistant Construction Regulation, NSR-10.

Chapter 7 studies the influence of the stiffness and structural period of wall building systems in the estimated vulnerability and seismic risk. A series of modifications are done to the original building archetypes to generate potential wall building configurations with reduced wall density.

Research Significance

The modeling techniques proposed here, while simple, allow the engineers to adequately simulate the seismic response of reinforced concrete elements with limited ductility capacity. Similarly, the seismicity model developed during this study represents a significant advance in the number of tools available for the application of performance-based earthquake engineering in Colombia. Lastly, the results obtained from the risk evaluation of the archetype buildings give an insight in the deficiencies of the thin wall building system and can be useful for the proposal of more adequate provisions for the design of this type of structures.

Chapter 1 – Observations on Thin RC Wall Buildings[1]

RC wall buildings are a very popular construction system in areas of high seismic hazard. Over the years, engineers have pushed design limits producing slender walls subjected to high flexural demands. Moreover, in many Latin American countries, a construction system with very thin walls and with different reinforcement detailing than those that have been verified in past laboratory testing or field experience has become common in residential mid- and high-rise buildings. This chapter provides a description of the major characteristics of this structural system as implemented in some regions of Colombia and discusses the provisions of the current Colombian building regulations for such systems. Finally, recent experimental findings on thin RC walls with similar characteristics are used to estimate the performance limit state values of this system.

1.1 Description of the Colombian thin RC wall building typology

The Colombian building typology consists of very thin concrete walls, with thicknesses t_w ranging from 80 mm to 150 mm (Arteta et al., 2017). **Figure 1.1** shows pictures of some typical thin RC wall buildings in Armenia, Colombia, a city in the high-seismicity Coffee Region. One of the principal features of these buildings is that RC walls constitute both the architectural and structural plan, resulting in highly redundant lateral load-resisting systems. The reduced thickness of these elements prevents the conception of special boundary elements in most cases, so the concrete is not effectively confined. Another characteristic of these buildings is their reinforcement steel configuration. To reduce costs and hasten construction, walls are designed with limited quantities of reinforcement that are usually supplied as a single curtain of cold-drawn welded wire meshes (WWM), with additional reinforcing bars at the wall boundaries when required by seismic demand. Results from laboratory tests (Carrillo et al., 2019) have shown that the mechanical behavior of WWM differs significantly from the conventional reinforcing steel for which the provisions in ACI 318 and NSR-10 were conceived. In general, WWMs have much higher yield strength ($f_y \geq 600$ MPa on average) with absence of clearly defined yield plateau, and exhibit almost null strain hardening and limited deformation capacity ($\varepsilon_{su} < 1.5\%$, on average). These previously described geometric and mechanical characteristics result in buildings with a lateral load-resisting system composed of elements with limited ductility.

Arteta et al. (2017) and Sánchez (2019) conducted an inventory of 28 thin RC wall buildings in the city of Armenia, Colombia. This city is in a highly seismic zone that was severely affected by the 1999 Coffee Region Earthquake. This work was later extended by the Colombian Earthquake Engineering Research Network (CEER) to 177 buildings, including other important cities in Colombia like Bogotá, Medellín and Cali (Arteta et al., 2018). The database compiled by these authors contains information regarding the location of the building, year of construction, number of floors, total height, floor plan dimensions,

[1] This chapter uses figures and text from Arteta et al. (2018), a report in which the author is acknowledged as a main contributor.

ratio of the wall shear area to the total floor plan area (wall area index), soil type, seismic hazard level, axial load demands due to permanent loads, material nominal properties, and geometry and reinforcement detailing of the structural elements. This document highlights the main findings of the research conducted by these authors. The statistical characterization of the building inventory in Armenia is of particular interest to this research, and is presented herein apart from that of the other cities. More details are available in the original sources.

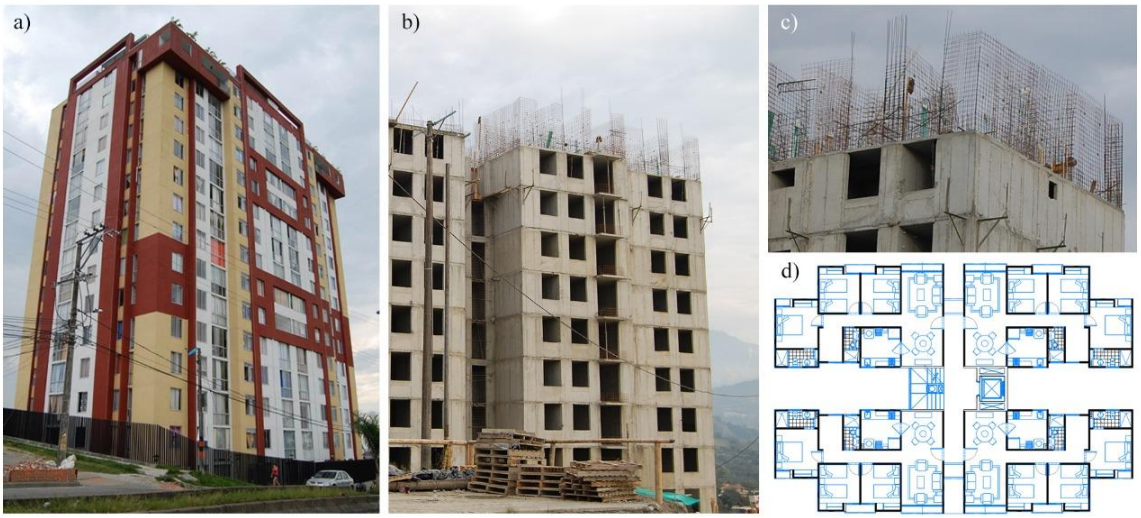

Figure 1.1 - (a) Typical thin RC wall building, (b) construction process, (c) steel reinforcement in form of WWM and (d) typical architectural plan (courtesy of J. Sánchez and C. Arteta).

1.1.1 Number of stories

Figure 1.2 shows the distribution of the number of stories in the building inventory of Armenia and the one extended to the rest of the cities mentioned above. Both databases show that thin RC wall buildings rarely exceed 17 stories. In Armenia, almost 30% of the buildings have 5 stories or less while about 60% are evenly distributed between 9 and 17 stories (**Figure 1.2a**). In the other cities, buildings with more than 12 stories are less common and 5- and 8-story buildings are typical (**Figure 1.2b**).

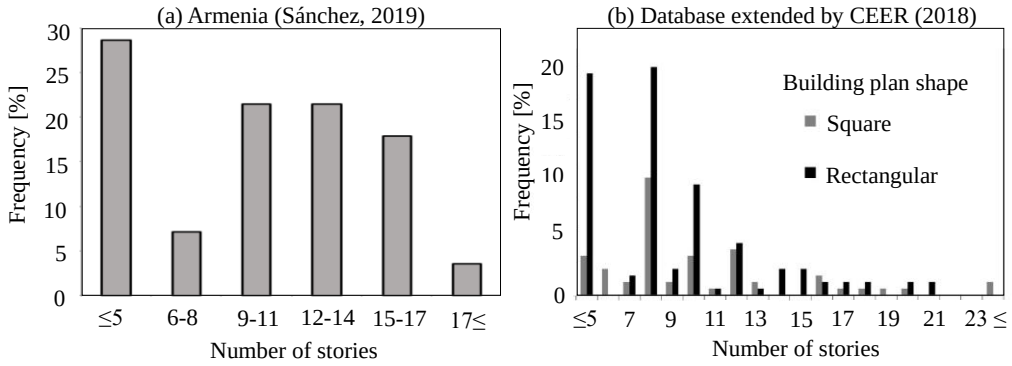

Figure 1.2 – Distribution of number of stories in thin RC wall buildings in some of the main Colombian cities: (a) only Armenia (adapted from Sánchez, 2019) and (b) Armenia, Bogotá, Cali and Medellín (adapted from Arteta et al., 2018).

1.1.2 Wall area index

The wall area index (WAI) is the ratio of the total wall shear area in a specific direction to the floor area of the building. It can sometimes be defined using the sum of the areas of all floors or of a specific floor plan. This research uses the area of the first floor. The WAI has been related to the seismic performance of wall buildings in several investigations (Jünemann et al., 2015; Lagos et al., 2012; Wallace, 1994; Wood, 1991). The influence of the WAI on the vulnerability and risk of thin RC wall buildings is explored in **Chapter 7**. **Figure 1.3** shows the distribution of this parameter in the building inventories of the cities mentioned above. The WAI is calculated for the two main directions of the buildings, where the longest floor plan dimension is called longitudinal and the corresponding orthogonal direction is called transverse. Buildings in the inventory in Armenia have WAI values in the longitudinal direction in the range of 1 to 4%, and 1 to 5% in the transverse direction, with typical values of 3 to 4% in both directions (**Figure 1.3a**). The extended building inventory for the other cities has lower WAI values, with typical values of 1 to 2% in the longitudinal direction and 2 to 3% in the transverse direction (**Figure 1.3b**).

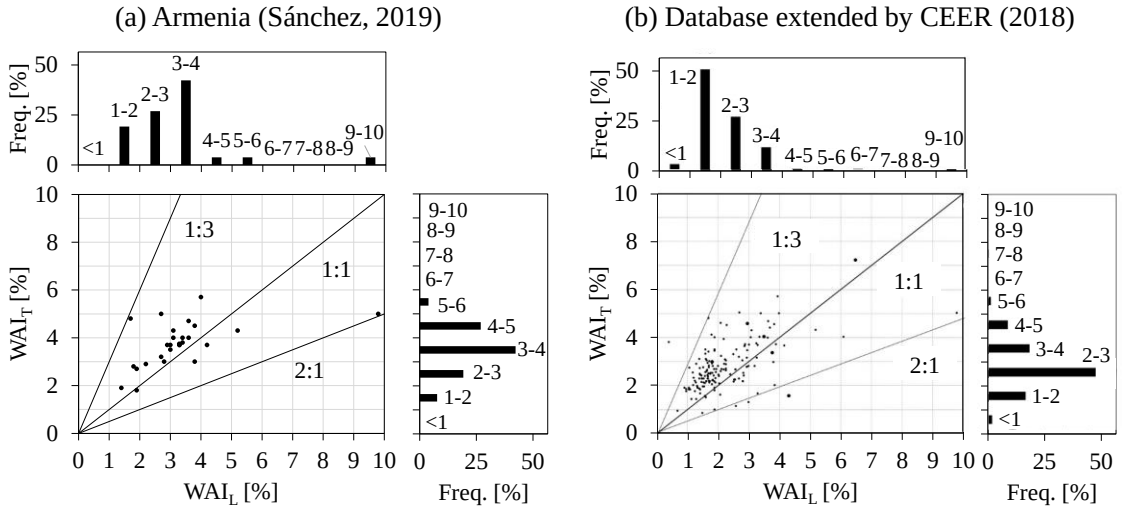

Figure 1.3 – Distribution of the first-story wall area index in the longitudinal (WAI_L) and transverse (WAI_T) direction observed in thin RC wall buildings in some of the main Colombian cities: (a) only Armenia (data from Sánchez, 2019) and (b) Armenia, Bogotá, Cali and Medellín (adapted from Arteta et al., 2018).

1.1.3 Wall cross-section, axial-flexural demands and reinforcement

Additionally, the authors analyzed the geometric and reinforcement characteristics of individual walls from both inventories. **Table 1.1** presents the most relevant characteristics. The data analysis shows that the walls in industrialized buildings tend to be relatively wide ($l_w \geq 3.0$ m) and thin ($80 \leq t_w \leq 150$ mm), and have cross-sections with wide flanges ($l_f \geq 1.5$ m). These characteristics result in walls with a slenderness ratio h_u/t_w (where h_u is the unsupported height of the wall near the base) typically greater than 16, which is the upper limit established in ACI 318 (2019) for walls expected to sustain large flexural-compression demand. Finally, both inventories show that thin RC walls in Colombia usually have axial load ratios P/f'_cA_g less than 10%, web reinforcement ratio ρ_l close to 0.25% and shear-span ratios M/Vl_w between 1.0 and 3.0.

Table 1.1 – Typical geometric features and reinforcement detailing of thin RC wall buildings in Colombia.

Parameter	Armenia		CEER's Inventory	
	Range	Expected	Range	Expected
Wall length, l_w [m]	1.9 – 7.6	4.0 – 5.0	1.0 – 8.0	3.0 – 5.0
Flange width, l_f [m]	0.65 – 5.3	1.5 – 2.5	Not reported	
Wall thickness, t_w [mm]	80 – 200	120 – 150 [a]	80 – 200	80 – 150 [a]
Aspect ratio, h_w/l_w	2 – 16	5 – 7	4 – 25	4 – 14
Slenderness ratio, h_u/t_w	12 – 30	16 – 20 [a]	8 – 28	20 – 28 [a]
Axial load ratio, P/f'_cA_g [%]	2 – 11	5 – 8 [a]	0 – 15	0 – 10 [a]
Shear span ratio, M/Vl_w	0.6 – 3.8	1.5 – 2.5	1.0 – 6.0	1.0 – 3.0
Web longitudinal reinforcement, ρ_l [%]	0.2 – 0.7	0.25 – 0.30	0.2 – 0.7	0.20 – 0.30

[a] This parameter is strongly related to building height.

As Colombian construction practice differs significantly from the RC wall buildings for which ACI 318-08 and NSR-10 provisions were conceived, it is important to establish whether these recommendations are applicable for the Colombian RC wall building typology. In particular, after the 2010 Chile and 2011 New Zealand earthquakes, Wallace (2012) noted the shortcomings of the then current version of ACI 318 (i.e. 318-11) with respect to the seismic design of thin RC walls and that more stringent limits should be imposed on the detailing of RC wall boundary elements, slenderness and maximum allowed drift ratios. In Peru, a country where the industrialized thin wall building system is also popular, the National Building Regulations (E.030, 2018) created a special category for these structures, recognizing that buildings with this structural system are characterized by not being able to sustain significantly large inelastic deformations. Peruvian regulations essentially limit the use of this system to "low-risk buildings" (equivalent to Risk Category II in ASCE 7-16) with maximum 8 stories.

1.2 Colombian building code provisions for the design of structural walls

The Colombian Regulation for Earthquake-Resistant Construction, NSR-10 (Comité AIS 100, 2010), lists reinforced concrete walls as one of the code-approved systems to resist the combined action of gravity and seismic loads. NSR-10 §A.3 contains the general requirements for the seismic design of RC wall building systems. In this section, structural walls in NSR-10 are classified into three categories according to their energy dissipation capacity: (i) minimum or ordinary (abbreviated as DMI in Spanish), (ii) intermediate (DMO) and (iii) special (DES). The NSR-10 differs in this aspect of ACI 318-08 in that the intermediate category does not exist in ACI 318 for structural walls. NSR-10 §A.3 states that structural walls must be designed using the elastic seismic forces reduced by the response modification coefficient, R. The values of R and the overstrength factor Ω_0 depend on the seismic hazard zone in which the structure is located and the required energy dissipation capacity. **Table 1.2** shows the values of the basic design coefficients R_0 and Ω_0 stipulated by NSR-10 for RC wall building systems.

Table 1.2 – Seismic design coefficients for structural walls according to NSR-10 §A.3.

Energy dissipation capacity	R_0	Ω_0	Design limitations according to seismic hazard		
			High	Moderate	Low
Special (DES)	5.0	2.5	Allowed up to a height of 50 m	Allowed for all heights	Allowed for all heights
Intermediate (DMO)	4.0	2.5	Not allowed	Allowed up to a height of 50 m	Allowed for all heights
Ordinary (DMI)	2.5	2.5	Not allowed	Not allowed	Allowed up to a height of 50 m

The provisions contained in NSR-10 for the structural design of these elements are adapted from ACI 318-08. However, as noted previously, the thin walls that compose the structural layout of an industrialized building have characteristics that differentiate them from traditional walls. The general design requirements for ordinary RC walls are introduced in NSR-10 §C.14 and special seismic provisions are included in §C.21. **Table 1.3** presents some of the most relevant features.

Table 1.3 – Minimum requirements for geometry and reinforcement detailing of ordinary structural concrete walls according to NSR-10 §C.14 and §C.21 (adapted from Sánchez (2019)).

Minimum thickness	$t_w \geq$	max(100 mm, h_w/25)
Vertical reinforcement	$\rho_l \geq$	0.0012 if $d_b \leq$ 16 mm or WWM 0.0012 if $d_b >$ 16 mm
Horizontal reinforcement	$\rho_t \geq$	0.0020 if $d_b \leq$ 16 mm or WWM 0.0025 if $d_b >$ 16 mm
Vertical and horizontal spacing	s_l or $s_t \leq$	min(3t_w, 450 mm)
Number of curtains of reinforcement	$N_{curtains} \geq$	1 if $t_w <$ 250 mm 2 if $t_w \geq$ 250 mm

The requirements for the detailing of intermediate and special structural walls are contained in NSR-10 §C.21.4 and §C.21.9, respectively. These are intended to guarantee the ductile behavior of the structure in the inelastic range. One of the main requirements is the use of special wall boundary elements (SBEs) in walls with high flexural-compressive demands. SBEs are a portion of the wall edge where the longitudinal reinforcement is enclosed in closely-spaced transverse reinforcement to confine the concrete and restrain rebar buckling. For RC walls designed to have a single critical section, NSR-10 (as well as ACI 318-08) requires SBEs in walls where the depth of the compression zone c satisfies **Equation (1.1)**, where l_w is the length of the wall, h_w is the total height from the base to the roof and δ_u is the design tip displacement. The value of c is computed from a section-response analysis using the nominal moment capacity M_n and factored axial load P_u associated to δ_u. The value of δ_u/h_w in **Equation (1.1)** must not be less than 0.7%. Alternatively, NSR-10 §C.21.9.6.3 allows to verify if SBEs are required using a limiting stress-based approach. According to this procedure, SBEs are required if the compressive stress demand at the wall boundary exceeds 20% of the nominal compressive strength of the concrete (i.e. if $\sigma > 0.2f'_c$). The stress demand is estimated by means of a linear elastic model using gross cross section properties and factored load combinations that include earthquake effects. This is the approach preferred by most structural engineers. Where compressive demands are lower and SBEs are not required, NSR-10 §C.21.9.6.5 requires ordinary boundary element transverse reinforcement if the longitudinal reinforcement ratio at the wall boundary is greater than $2.8/f_y$ [MPa] to prevent rebar buckling.

$$c \geq \frac{l_w}{600(\delta_u/h_w)} \tag{1.1}$$

The requirement in **Equation (1.1)** follows a displacement-based design approach and is based on certain assumptions whose validity in the Colombian context is debatable. To understand the basics behind **Equation (1.1)**, consider the plastic hinge model of a T-shaped RC wall cantilever in **Figure 1.4**. The model assumes all the lateral tip displacement is due to plastic rotation at the plastic hinge, neglecting any elastic contribution outside it. This simple approach allows to relate the global- and local-behavior EPDs (e.g. tip displacement and compression zone depth) (Arteta, 2015). The tip displacement of the wall δ_u is given by **Equation (1.2)**, where $\theta_{p,u}$ is the plastic rotation at the hinge and h_w is the height of the wall. Assuming a uniform curvature distribution along an expected value of the plastic hinge length l_p, the plastic rotation can be expressed in terms of the curvature at the critical section ϕ_u, the compression depth c, and the compressive strain of the most extreme fiber ε_{cu} following **Equation (1.3)**. The formulations in **Equations (1.2)** and **(1.3)** are combined to estimate the demand imposed at the cross-section level by a given roof drift ratio. Assuming a limit compressive strain $\varepsilon_{cu} = 0.003$ and a plastic hinge length $l_p = l_w/2$, the limiting compression zone depth c_{limit} is as expressed in **Equation (1.4)**. The simple plastic hinge model described here-in was used to develop the current NSR-10 provisions for SBE detailing. Note that **Equation (1.1)** is the result of applying number rounding to **Equation (1.4).**

$$\delta_u = \theta_{p,u} h_w \tag{1.2}$$

$$\theta_{p,u} = \phi_u l_p = \left(\frac{\varepsilon_{cu}}{c}\right) l_p \tag{1.3}$$

$$c_{limit} = \frac{(\varepsilon_{cu} = 0.003)(l_p = l_w/2)}{\delta_u/h_w} = \frac{l_w}{667(\delta_u/h_w)} \tag{1.4}$$

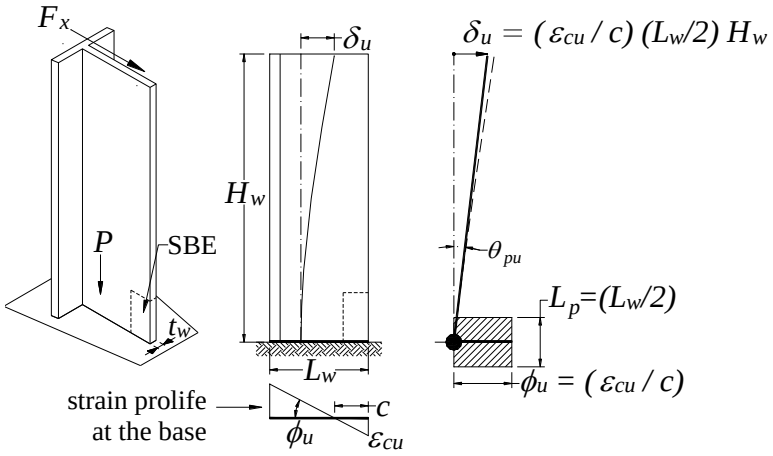

Figure 1.4 - Plastic hinge model relating global to local demand parameters on a T-shaped wall (Arteta, 2015).

When analyzing the procedure described above to develop **Equation (1.1)**, it is evident that the results obtained are sensitive to the values used for the tip displacement and the plastic hinge length. In NSR-10 no distinction is made, however, with respect to

whether the value of δ_u/h_w should come from an analysis with cracked sections or gross sections, since both types of analysis are allowed in the regulation, being typical the latter in engineering offices. The original equation in ACI 318-08 is meant to be used along with cracked-section modeling. Moreover, the lower limit of 0.7% in the value of δ_u/h_w requires a moderate deformation capacity in the structural walls. Recent experimental research (Segura & Wallace, 2018a) suggests that excessively slender walls are expected to have drift capacity less than 1.0%, limiting the applicability of **Equation (1.1)**. It has also been experimentally observed that damage in poorly detailed slender walls is concentrated in the range $2t_w \leq l_p \leq 3t_w$, which directly limits displacement capacity and would activate the requirement of SBEs under lower flexural demands (Blandón & Bonett, 2019; Segura & Wallace, 2018b; Takahashi et al., 2013; Wallace, 2011; Welt, 2015).

Other considerations for the design of special structural walls are contained in **Table 1.4**. Regarding the analysis of L, T or C-shaped wall sections, **Table 1.4** indicates that the influence of the flange reinforcement should be considered when studying the flexural-axial demands on the thin web edge of the wall by means of an effective flange width. This is because along with the axial load, the amount of flange reinforcement significantly influences the computed compression depth c and compressive strains at the web edge.

Although the inclusion of SBEs is a good engineering practice in high seismic risk zones, the reduced thickness of the thin Colombian walls does not allow their design in most cases, and if constructed, their effectiveness is uncertain according to the results by Arteta (2015). When it is concluded that SBEs are required in a thin wall section by applying **Equation (1.1)**, structural engineers increase the specified concrete compressive strength f'_c so that the computed stresses are less than $0.2f'_c$ (NSR-10 §C.21.9.6.3). Vertical and horizontal reinforcement is usually provided in the form of a single curtain, using small diameter deformed bars or WWM. Again, the value of f'_c is often increased so that factored shear force demands V_u are less than the limit in **Table 1.4**.

The intention of NSR-10 regulations with the recommendations in **Table 1.3** and **Table 1.4** is to guarantee the ductile behavior of structural walls. However, the geometric and reinforcing characteristics of the Colombian building inventory call into question their effectiveness. The research reported here aims to evaluate whether the performance of thin RC wall buildings meets NSR-10 objectives under design seismic excitation and provide an estimation of their vulnerability, as well as the risk to which these structures are exposed.

Table 1.4 – Additional requirements for geometry and reinforcement detailing of special structural walls according to NSR-10 §C.21.

Vertical reinforcement	$\rho_l \geq$	0.0025
Horizontal reinforcement	$\rho_t \geq$	0.0025
Number of curtains of reinforcement	$N_{curtains} \geq$	2 if $V_u \geq 0.17A_{cv}\sqrt{f'_c}$
Effective flange width on each side of the web		The lower of one-quarter of the height from the section under consideration to the top of the wall, the actual width and half the distance to adjacent wall webs
Transverse reinforcement at the wall boundary	$A_{sh} \geq$	$0.09(f'_c/f_{yt})(s\ b_c)$

1.3 Experimental limit states of thin RC walls

The failure modes observed in recent earthquakes aroused the interest of the engineering community in the study of the seismic behavior of thin RC walls. Since then, tests have been conducted on various types of RC walls according to the construction practice of each country. Few experiments, however, match the characteristics of the Colombian building typology. Most of the experimental data available for industrialized walls in the literature correspond to shear-dominated low-rise buildings (Carrillo & Alcocer, 2011; Quiroz et al., 2013). Alarcon et al. (2014) tested taller specimens, representative of the Chilean construction typology. Their experimental campaign focused on evaluating the effect of high axial loads ($0.15 \leq P/f'_cA_g \leq 0.35$) in the seismic behavior of RC walls with unconfined boundaries. However, as discussed in **Section 1.1**, thin RC wall buildings in Colombia have axial load demands that rarely exceed $0.10f'_cA_g$ under static gravity loading (e.g. under load combination 1.0D+0.25L). Riva and Franchi (2001) conducted a series of experimental tests on rectangular walls reinforced with traditional, and hot-rolled and cold-drawn WWM. The response of their specimens may be considered an upper bound of the expected behavior of the industrialized system evaluated herein. More recently, Almeida et al. (2017), Blandón et al. (2018), and Blandón et al. (2020) tested a series of full-scale thin wall specimens that were, with the latter two closely resembling the construction practice in Colombia.

The specimens from Blandón et al. (2018) exhibited a deformation capacity below the 1.43% design drift limit imposed by the NSR-10 for concrete structures. The tested walls had a 100-mm thick T-shaped cross-section with minimal web reinforcement in the form of a single curtain of cold-drawn WWM or hot-rolled deformed bars and additional unconfined boundary reinforcement. Typical failure modes included rupture of reinforcing steel due to tensile strain concentration at the base, lap splice failure due to bar slippage, concrete crushing concentrated in a short-height region, and rebar buckling (**Figure 1.5a, b**). In all cases, current NSR-10 provisions proved to be insufficient.

The reduced thickness of the RC walls that conform the structural layout of industrialized buildings raised initial concerns among the engineering community after the global out-of-plane instability failures observed in much thicker and better detailed walls after the 2010 Chile and 2011 New Zealand earthquakes. However, none of the specimens tested by Blandón et al. (2018) experienced out-of-plane buckling in their web boundaries. This is primarily because in order for out-of-plane buckling to occur at a wall boundary, the latter must have experienced extensive cracking due to previous cycles of tension and

compression. Experimental evidence suggests that reduced reinforcement steel quantities at the wall edges, and the elastoplastic behavior of cold-drawn wires prevents the propagation of cracks along the height of the wall. **Figure 1.6** shows a comparison between the cracking patterns observed in one of the walls tested by Blandón et al. (2018) and another thin RC wall specimen tested by Rosso et al. (2016) and Almeida et al. (2017). The latter specimen is an 80-mm thick T-shaped wall that was also designed according to Colombian engineering practice, but including ductile web and boundary reinforcement. **Figure 1.6a** shows that the cracking pattern of the first wall was composed of three main cracks located at the base, mid-height, and top of the wall that extended along almost the entire length of the wall section. The concentration of tensile strains ends up limiting the drift capacity of the wall, since it promotes early reinforcement rupture. On the other hand, the wall reinforced with ductile bars in **Figure 1.6b** exhibited more distributed cracks over height, with some major cracks extending along the wall web section and other cracks limited to the wall boundary. The ductile reinforcement prevented tensile strain concentration but promoted out-of-plane buckling (**Figure 1.5c**) due to the reduced wall thickness, limiting the drift ratio capacity of the wall to 0.70%.

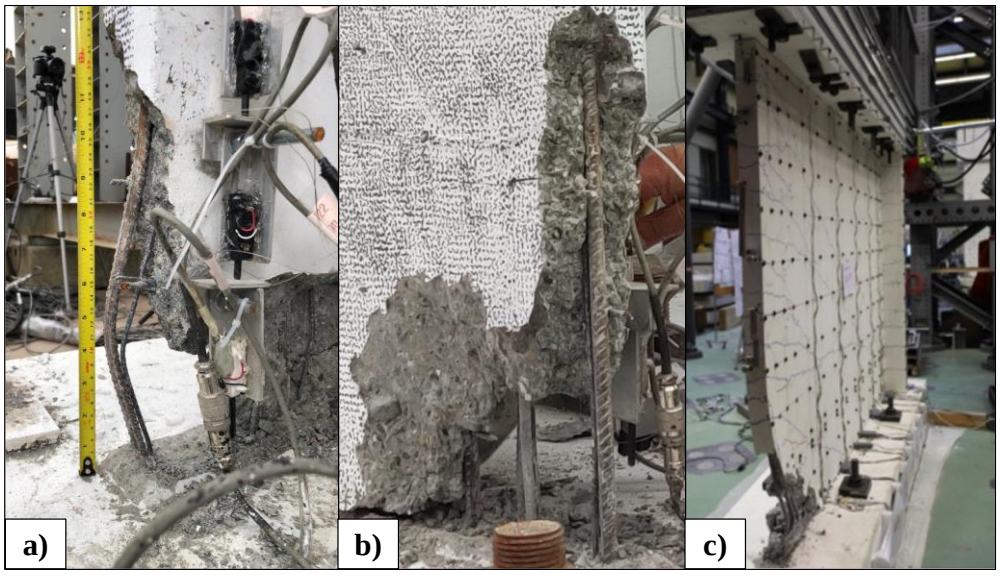

Figure 1.5 - Experimentally-observed damage in thin RC walls: (a) rebar buckling, (b) unconfined concrete spalling, and (c) out-of-plane instability (Blandón et al., 2020; Rosso et al., 2016).

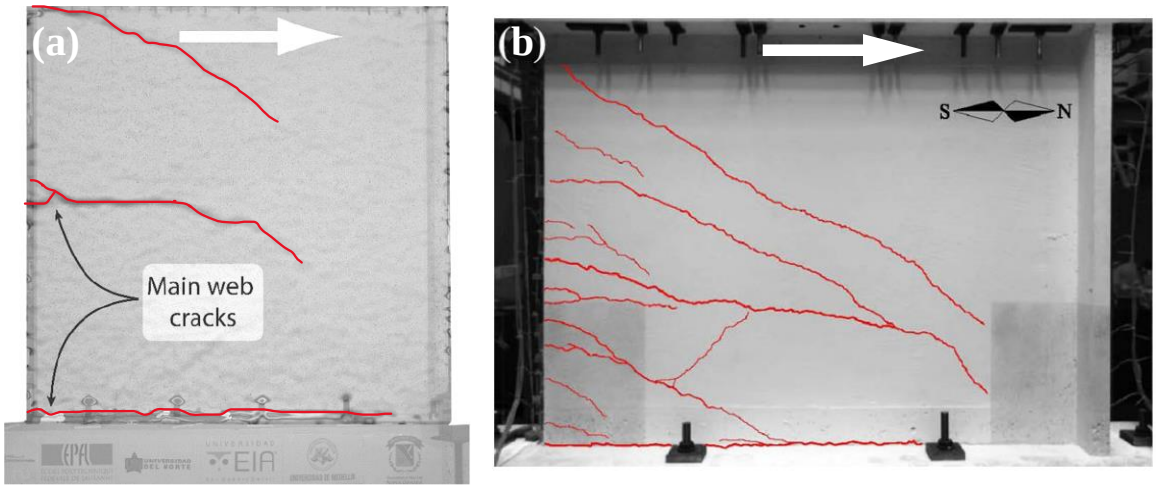

Figure 1.6 – Crack patters observed in thin RC wall web boundaries reinforced with (a) cold-drawn WWW (Blandón et al., 2018) and (b) ductile hot-rolled rebars (Rosso et al., 2016).

Table 1.5 presents a compilation of the main features of the specimens from Riva and Franchi (2001), Blandón et al. (2018) and Almeida et al. (2017). The database also includes the specimens from Segura and Wallace (2018b), which have special boundary elements detailed according to the ACI 318-14 and represent the traditional cast-in-place RC wall system. The set is composed by rectangular walls and T-shaped walls with web boundaries tested in compression. The rotation capacity of these walls is analyzed in terms of their unbraced height h_u, thickness t_w, length l_w and compression depth c. Three nondimensional parameters based on the previous geometric measurements were identified as strongly correlated to the rotation capacity of the walls θ_u, namely the cross-section aspect ratio (l_w/t_w), the compression zone aspect ratio (c/t_w) and the product of the previous two (cl_w/t_w^2). Here, θ_u is defined as the first-story drift ratio corresponding to a loss of lateral load capacity of 20%. The choice of the first-story drift ratio is supported by experimental evidence showing that the structural damage in thin RC walls concentrates in a very small region of the first story. The first-story drift is also easy to estimate using any structural analysis software and eliminates the variability associated to the definition of a plastic hinge length.

Figure 1.7 shows the relationship between the expected rotation capacity of a wall and its different geometric characteristics. The results in **Figure 1.7a** suggest that walls with a larger cross-section aspect ratio tend to have a reduced rotation capacity. The building inventory assembled by Arteta et al. (2017) indicates that walls with $l_w/t_w > 25$ are very common in Colombia. From the data set, 5 tests were performed on walls with such slender cross sections and all of them exhibited a rotation capacity $\theta_u < 1.0\%$. While there is a strong correlation in the data between l_w/t_w and θ_u, the first is not always a good predictor of performance. This is evident in the tests from Riva and Franchi (2001), whose specimens share the same value of l_w/t_w but have significantly different θ_u. Segura and Wallace (2018a) showed that c/t_w correlates well with the drift capacity of slender walls, as the reduced compressive damage zone observed in thin RC walls is more closely related to t_w than l_w. **Figure 1.7b** suggests that walls with $c/t_w > 3$ are likely to have $\theta_u < 1.5\%$. Sánchez and Arteta (2017) estimated the expected compression depth of a wall in Colombia as shown in **Equation (1.5)**. For a 10-story wall ($h_w = 25$ m) with $l_w/t_w > 20$, the predicted

c/t_w is larger than 5. We can associate the results from **Figure 1.7a** and **Figure 1.7b** using the parameter cl_w/t_w^2 (Abdullah & Wallace, 2019). The combined parameter accounts for the impact of geometry, reinforcement detailing, axial load and material properties. **Figure 1.7c** indicates that walls with $cl_w/t_w^2 > 50$ are prone to have $\theta_u < 1.0\%$. In general, these trends in the experimental database from **Table 1.5** suggests that the expected first-story drift ratio capacity of very thin RC walls is between 0.5% and 1.0%.

$$\frac{c}{l_w} = (0.0076\text{m}^{-1})h_w + 0.066 \tag{1.5}$$

Table 1.5 – Review of experimental tests on thin RC walls under cyclic loading.

Author	ID	Shape	t_w [mm]	h_u [mm]	l_w [mm]	c [mm]	P [kN]	θ_u [%]	Add. Bound. Rebars	Web Reinf.	Confined Bound.
Riva and Franchi (2001)	B16R8-1	Rect.	150	2500	1200	201	0	2.22	Yes	Rebar	Yes
	B16R8-2	Rect.	150	2500	1200	201	0	2.94	Yes	Rebar	Yes
	HR12C-1	Rect.	150	2500	1200	307	600	2.70	No	Hot rolled WWM	No
	CD12C-1	Rect.	150	2500	1200	329	600	1.96	No	Cold drawn WWM	No
	HR12C-2	Rect.	150	2500	1200	307	600	2.33	No	Hot rolled WWM	No
	CD12C-2	Rect.	150	2500	1200	329	600	2.33	No	Cold drawn WWM	No
	B14HR8S	Rect.	150	2500	1300	240	0	2.86	Yes	Hot rolled WWM	Yes
	B14HR8U	Rect.	150	2500	1300	276	0	3.45	Yes	Hot rolled WWM	Yes
	B14CD8S	Rect.	150	2500	1300	258	0	2.13	Yes	Cold drawn WWM	Yes
	B14CD8U	Rect.	150	2500	1300	299	0	2.17	Yes	Cold drawn WWM	Yes
	HR12S	Rect.	150	2500	1300	285	0	2.78	No	Hot rolled WWM	Yes
	HR12U	Rect.	150	2500	1300	356	0	2.94	No	Hot rolled WWM	Yes
	CD12S	Rect.	150	2500	1300	315	0	1.43	No	Cold drawn WWM	Yes
	CD12U	Rect.	150	2500	1300	379	0	2.04	No	Cold drawn WWM	Yes
Segura and Wallace (2018b)	WP1	Rect.	152	2134	2286	526	1201	1.59	Yes	Rebar	Yes
	WP2	Rect.	152	2134	2286	480	1201	1.52	Yes	Rebar	Yes
	WP3	Rect.	152	2134	2286	480	1201	1.51	Yes	Rebar	Yes
	WP4	T-shaped	152	2134	2286	686	1201	1.31	Yes	Rebar	Yes
	WP6	Rect.	191	2134	2286	411	1501	2.69	Yes	Rebar	Yes
	WP7	Rect.	229	2134	2286	400	1802	2.98	Yes	Rebar	Yes
Blandón et al. (2018)	W4	T-shaped	100	2400	2500	359	470	0.86	No	Rebar	No
	W5	T-shaped	100	2400	2500	374	470	0.97	No	Cold drawn WWM	No
	W6	T-shaped	100	2400	2500	322	470	0.85	Yes	Rebar	No
	W7	T-shaped	200	2400	2500	178	490	1.21	Yes	Rebar	No
(Almeida et al., 2017)	TW1	T-shaped	80	2000	2700	285	303	0.75	Yes	Rebar	No
	TW4	T-shaped	80	2000	2700	285	303	0.75	Yes	Rebar	No
	TW5	Rect.	150	2500	1200	201	0	2.22	Yes	Rebar	Yes

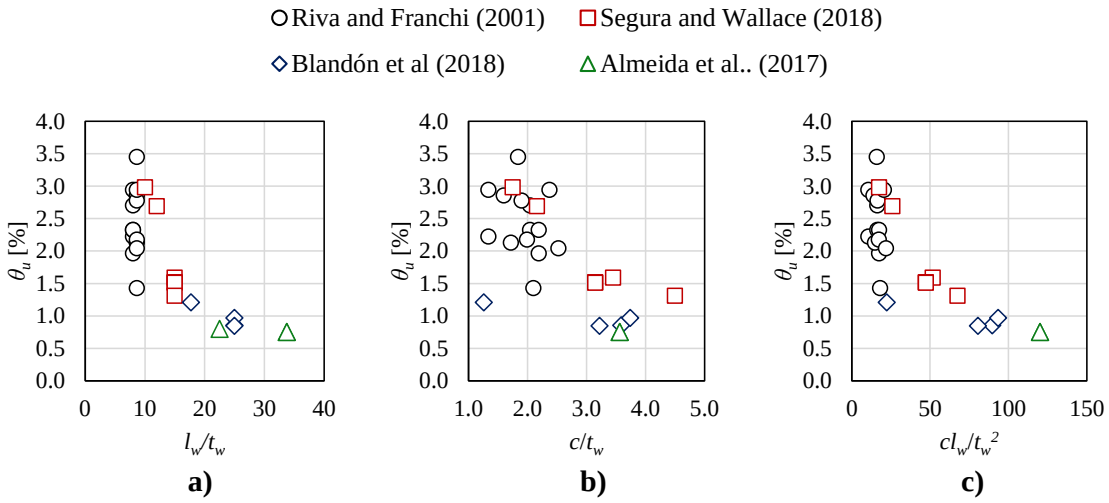

Figure 1.7 - Rotation capacity as a function of (a) the cross-section aspect ratio, (b) the compression aspect ratio and (c) a combination of (a) and (b).

Chapter 2 – Building Archetypes

This chapter describes the geometry and design criteria of the building archetypes that will later be used as a case study to estimate the vulnerability and risk of the thin RC wall building system. The design of the wall elements follows typical Colombian engineering practices. At the end, there is a discussion of some of the issues structural engineers often encounter during the design process of RC walls subjected to high axial-flexural demands and how these issues are addressed following the NSR-10 design prescriptions.

2.1 Description of the building archetypes

Three case-study buildings are selected to investigate the seismic performance of thin RC wall building systems. All the buildings share the same structural plan presented in **Figure 2.1**, varying the thickness of the walls and the number of stories. Typical floor plan has an area of 458 m^2. The buildings are assumed to be located in the city of Armenia, one of the most seismically active areas in Colombia, as their structural plan is a simplified version of an actual 10-story building in this city. RC walls are connected through a rigid diaphragm comprising a 120-mm thick slab.

Table 2.1 presents a summary of the main geometrical characteristics of the three case-study buildings. The buildings have 5, 10 and 15 stories, with typical interstory height of 2.50 m. The purpose of selecting three buildings whose most significant variation is the number of stories is to study the performance of low, moderate and relatively high-rise buildings. However, the configuration of some of the taller buildings in Colombia may differ from that in the case study. Nevertheless, the results from buildings of increasing height help understand the impact of the structural period in the seismic risk. For example, Cando et al. (2020) found that tall RC wall structures with reduced stiffness are subjected to reduced seismic risk in Chile. This is so because of the trade between higher vulnerability and lower seismic hazard for longer structural periods, as is demonstrated later in this document (**Chapter 6** and **Chapter 7**). The number of stories of each building coincides with the statistical trends of the building inventory in the city (**Figure 1.2a**). The required wall thickness is directly related to the number of stories. The WAI of the building archetypes in the longitudinal direction is in the range of 2.5 to 3.8 %, while in the transverse direction it is in the range of 2.7 to 4.1%. This is consistent with the typical values for the city of Armenia presented in **Figure 1.3a**, where values of WAI in the transverse direction tend to be higher.

Table 2.1 – Geometrical characteristics of the building archetypes.

ID	Number of stories	t_w [mm]	h_p [m]	WAI_L [%]	WAI_T [%]	f'_c [MPa]	Do walls have special boundary elements?
B05	5	100	2.50	2.53	2.72	21	No
B10	10	120	2.50	3.04	3.27	35	No
B15	15	150	2.50	3.80	4.09	35	Yes

t_w: wall thickness. h_p: interstory height. WAI_L: longitudinal wall area index. WAI_T: transverse wall area index. f'_c: concrete compressive strength.

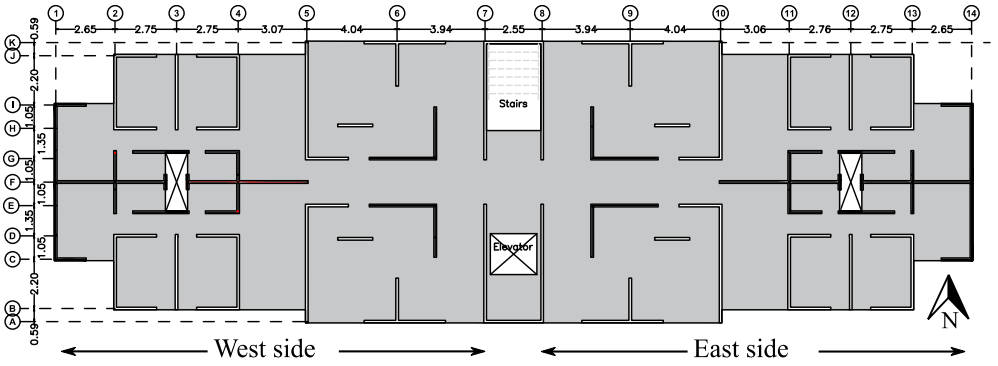

Note: walls colored in black represent elements of special interest for this study. Units: meters

Figure 2.1 - Typical floor plan of the building archetypes.

2.2 Linear model and design forces

For all the case-study structures, the superimposed dead load on the slab is assumed as D = 1.60 kN/m^2, while the live load is assumed as L = 1.80 kN/m^2. Specified concrete compressive strength for each of the buildings is presented in **Table 2.1**. Two types of reinforcing steel are considered in the walls: cold-drawn wire meshes (Φ7.5-8.5 mm @ 150 mm) and hot rolled deformed bars (Φ12-19 mm). Nominal yield strength of the wire mesh and the deformed bars is $f_{y,nWM}$ = 490 MPa and $f_{y,nRB}$ = 420 MPa, respectively.

The building archetypes are analyzed and designed using a linear-elastic model in ETABS® (Computers and Structures, Inc., 2019). An effective in-plane bending stiffness $EI_{eff} = 0.50EI_g$ is considered to account for the effects of cracking. The use of cracked properties allows the engineer to limit inter-story drift ratios up to 1.0%/0.7 = 1.43%, according to NSR-10 §A.6. The seismic mass is estimated as that provided by the entire dead load and 25% of the live load (1.0D+0.25L), lumped at every floor level, as suggested by the TBI guidelines (PEER, 2017). The modulus of elasticity is assumed as $E_c = 3900\sqrt{f'_c}$ [MPa]. **Table 2.2** summarizes the structural periods of each building, estimated using Eq. NSR-10 A.4.2-3 and a linear modal analysis on ETABS®. The 5-story building has cracked periods in the range 0.20 s ≤ T ≤ 0.24 s, the 10-story building in the range 0.54 s ≤ T ≤ 0.59 s, and the 15-story building has periods close to 1.0 s.

Design seismic forces are estimated using an elastic response spectrum analysis, following NSR-10 §A.2 requirements. The case-study buildings are classified as Category I (residential occupancy) and are located in Armenia (Colombia) on a stiff soil site (Site Class D). The obtained elastic design spectrum is presented in **Figure 2.2**. The base shear computed using the response spectrum analysis is scaled to match at least the 80% of the elastic shear demand estimated using the equivalent lateral load (ELL) method (NSR-10 §A.5.4.5). According to NSR-10 Table A.2.3-2, Armenia is located in a high seismic hazard zone. This requires the archetype buildings to have a lateral force resisting system conformed by special RC walls (**Table 1.2**). Under this assumption, elastic forces are reduced by a response modification factor R = 5.0 to obtain the corresponding pier design forces. The computed design base shear, the seismic weight of each building and the roof drift ratio demands are presented in **Table 2.2**. Story drifts demands are shown in **Figure 2.3** for both directions of analysis, including orthogonal effects according to NSR-10

§A.3.6.3. The maximum design story drifts typically occur within the middle third of the height, all being less than the drift limit proposed in NSR-10 §A.6.4.1.

Table 2.2 – Fundamental periods and elastic base shears of the building archetypes from modal analysis.

ID	Fundamental period (NSR-10) C_uT_a [s](1)	Modal analysis (ETABS®) (2)		Seismic weight W [kN]	Design base shear (3) $V_{EW,\,NS}$ [kN]	Design base shear coefficient C_s [-]	Roof drift ratio, δ_u / h_w [%]	
		T_{EW} [s]	T_{NS} [s]				*EW*	*NS*
B05	0.39	0.23	0.19	17400	2262	0.13	0.12	0.10
B10	0.66	0.59	0.54	37700	4901	0.13	0.43	0.41
B15	0.89	1.01	0.98	63100	6460	0.10	0.66	0.65

(1) $T = C_uT_a = C_uC_th^{\alpha}$, with C_u = 1.2 and C_t = 0.049 and α = 0.75.
(2) These periods account for cracked or effective properties.
(3) Computed from modal spectrum analysis. It includes reduction by R and scaling to 80% of the ELL base shear.

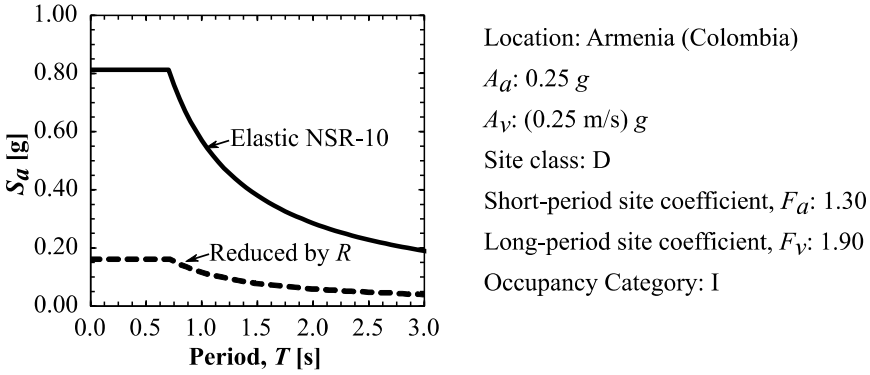

Figure 2.2 - Estimated elastic design spectrum for the case-study buildings.

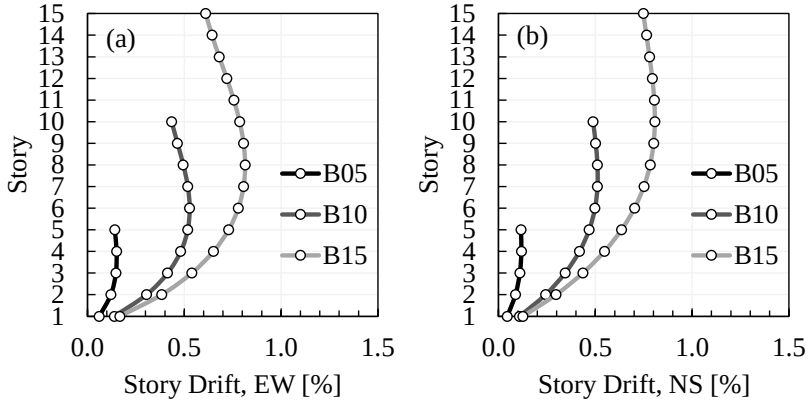

Figure 2.3 - Story drift ratio demand for the case-study buildings in the (a) longitudinal (EW) and (b) transverse (NS) dimension.

2.3 Wall design

The walls in the building archetypes are designed to have a single critical section at the base and minimum reinforcement ratio in the web section in the longitudinal and transverse direction ($\rho_{web,long} = \rho_{web,transv} = 0.0025$). Typical web reinforcement is provided in the form

of cold-drawn WWM except more reinforcement is required by flexural demands. If additional reinforcement is needed to satisfy seismic demands, it is provided as hot rolled deformed boundary rebars. Because the structures are located in a high seismic hazard zone, RC walls must meet the reinforcement detailing requirements for special RC structural walls contained in NSR-10 §C.21.9, which were previously discussed in **Chapter 1**. These requirements establish that RC walls must have special boundary elements (SBEs) if the compressive zone depth exceeds the limit of **Equation (1.1)** (displacement-based method) or if the compressive stresses at the extreme fiber exceed $0.20f'_c$ under the action of the different factored load combinations (forced-based method)

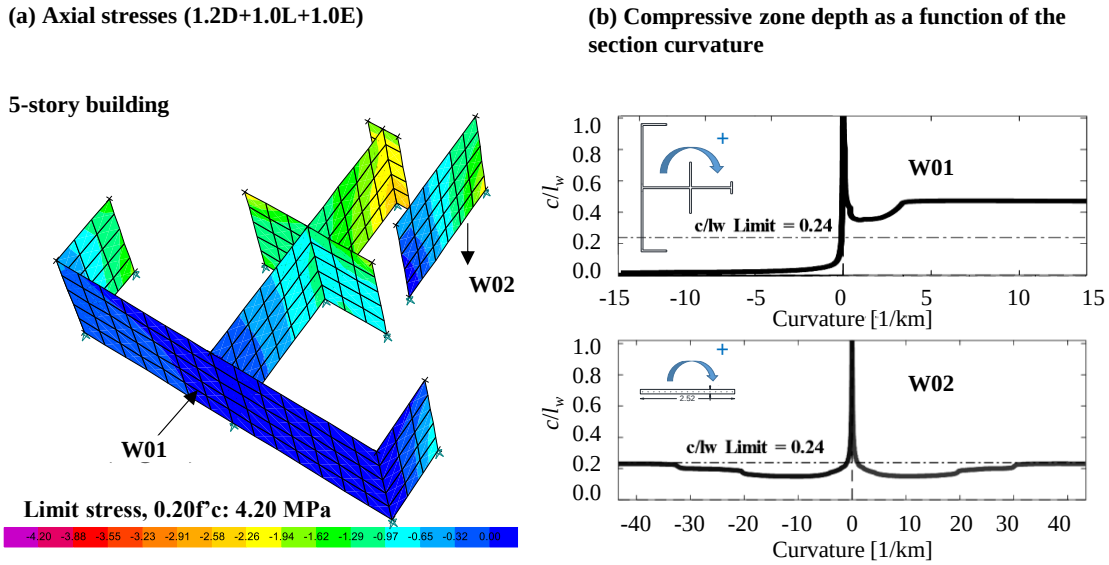

Figure 2.4 – Comparison between the results obtained using (a) the force-based method and (b) the displacement-based method for a flanged and a rectangular wall in the 5-story building archetype.

NSR-10 gives the structural engineer freedom to choose which method to use to determine if a wall must have SBEs. In engineering offices there is a preference for the force-based method, because the stresses can be easily estimated with any structural analysis program. There are, however, some inconsistencies in the application of these criteria in the design of thin RC walls. In some cases, the displacement-based and force-based methods do not draw the same conclusion about the need to use SBEs, since the stresses from an elastic structural analysis are not necessarily compatible with an inelastic section analysis. **Figure 2.4** provides an example of this problem. **Figure 2.4(a)** shows two walls located in the first story of the 5-story building, subjected to design seismic and gravitational loading stresses. The color scale is saturated in such a way that the minimum value corresponds to $0.2f'_c$. That is, if purple colors are observed in any portion of the wall, boundary elements are required according to the force-based method. **Figure 2.4(b)** shows the ratio of the compressive zone depth to the length of the wall (denoted $c/d = c/l_w$) as a function of the curvature at the critical section obtained from a nonlinear section analysis. The limiting ratio c/l_w, computed from **Equation (1.1)** and the roof drift ratio δ_u/h_w demands from **Table 2.2**, is highlighted with a dotted horizontal line. The value of δ_u/h_w obtained from the linear analysis is 0.12%. However, **Equation (1.1)** requires the value of δ_u/h_w to not be less than 0.7%. Enforcing this condition results in a limiting ratio c/l_w =

0.24. Note that neither of the two walls shown in the figure exhibits stresses larger than the limiting value of $0.2f'_c$ = 4.2MPa and would not require SBEs according to the force-based method. However, when the largest flange of the W01 wall pier in **Figure 2.4** is loaded in tension, the observed ratio c/l_w exceeds by a great margin the limiting value of **Equation (1.1)**, activating the requirement for SBEs according to the displacement-based method. In this case, the discrepancy between the two methods is mainly due to the lower limit of 0.7% in the value of δ_u/h_w. This limit seems conservative considering the low design displacements demands to which these buildings are subjected, especially in low-rise buildings. Despite the displacement-based method resulting in the need of SBEs, the design of the wall elements in this research follows the force-based method, as this is the preferred method by most structural engineers.

After analyzing the structural plans of the buildings in the inventory of Armenia, it was found that it is a common practice in structural companies to include closed stirrups in walls with thickness $t_w \geq 120$ mm even if no SBEs are required to comply with the requirements of ordinary boundary elements in NSR-10 §C.21.9.6.5. Accordingly, structural detailing of the walls in the 10 and 15-story buildings includes transverse boundary reinforcement whenever flexural demands require the addition of large amounts of longitudinal reinforcement concentrated at the wall boundary. On the other hand, experimental research has shown that the geometrical constraints imposed by a wall thickness $t_w < 150$ mm make it unfeasible to conceive an effectively confined boundary element (Arteta, 2015). For this reason, the 5- and 10-story structures are designed so that it is not necessary to include SBEs following the force-based method. For the 15-story building, it is assumed that the 150-mm thick walls provide enough room for the inclusion of SBEs, as NSR-10 does not impose a limit in the minimum thickness of SBEs. This consideration is consistent with Colombian engineering practice. Although such thin boundary elements can be constructed, their confinement effectiveness would not be considered in the nonlinear simulations used for risk assessment, as will be later explained in **Chapter 4**.

Figure 2.5 depicts typical reinforcement of key wall elements (those colored in black in **Figure 2.1)** for the 10-story building. Short-length walls such as the W02 piers have only distributed reinforcement in the form of cold-drawn WWM. On the other hand, wall piers of greater dimensions or with flanged-sections have ordinary boundary elements with ductile hot-rolled rebars due to their increased flexural demands. This reinforcement configuration varies significantly for each building archetype. As an example, **Figure 2.6** shows a comparison of the provided reinforcement for the W04 wall pier in each building. In the case of the 5-story wall, the design flexural demands are low enough for the wall to require only minimum WWM reinforcement. As a result, the outermost WWM fibers in the 5-story wall will exhibit larger strain demands than its 10-story counterpart when subjected to the same strain profile. This increases the potential risk of the early rupture of reinforcement, as will be explained in **Chapter 6**. In the case of the 15-story building, the provided boundary longitudinal and transverse reinforcement quantities increase with respect to the 10-story archetype to compensate the observed higher design flexural demands and meet the detailing requirements of SBEs.

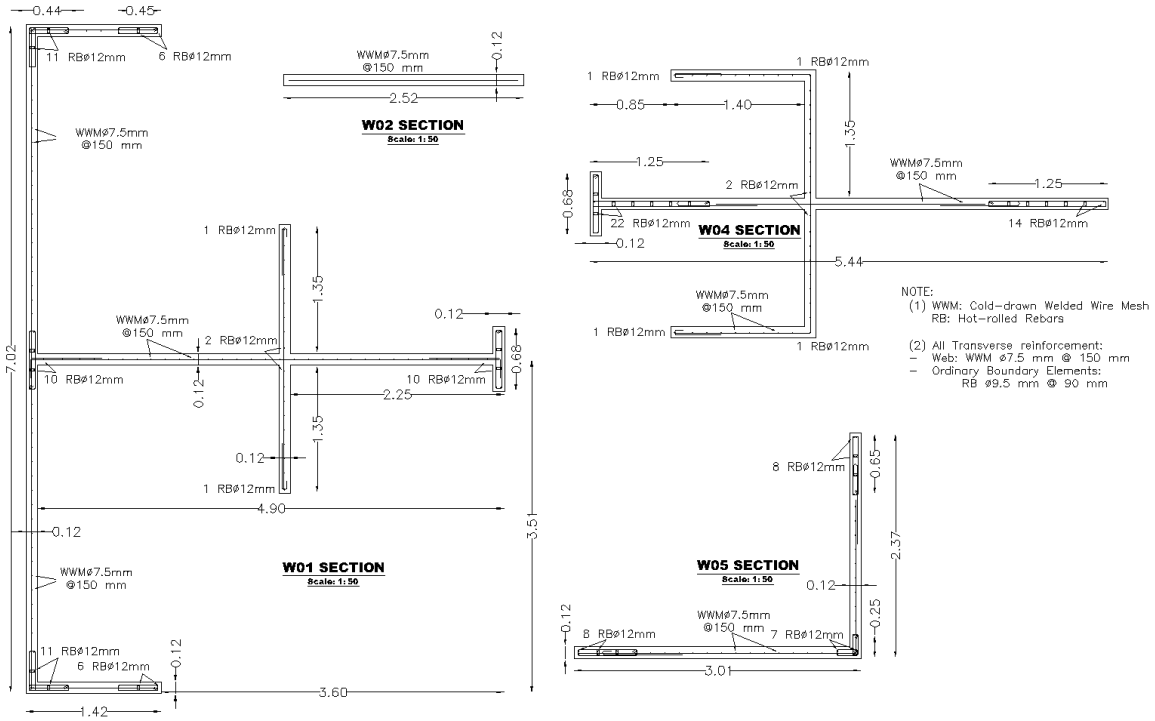

Figure 2.5 – Typical reinforcement layout of key wall specimens in the 10-story building. Units: meters

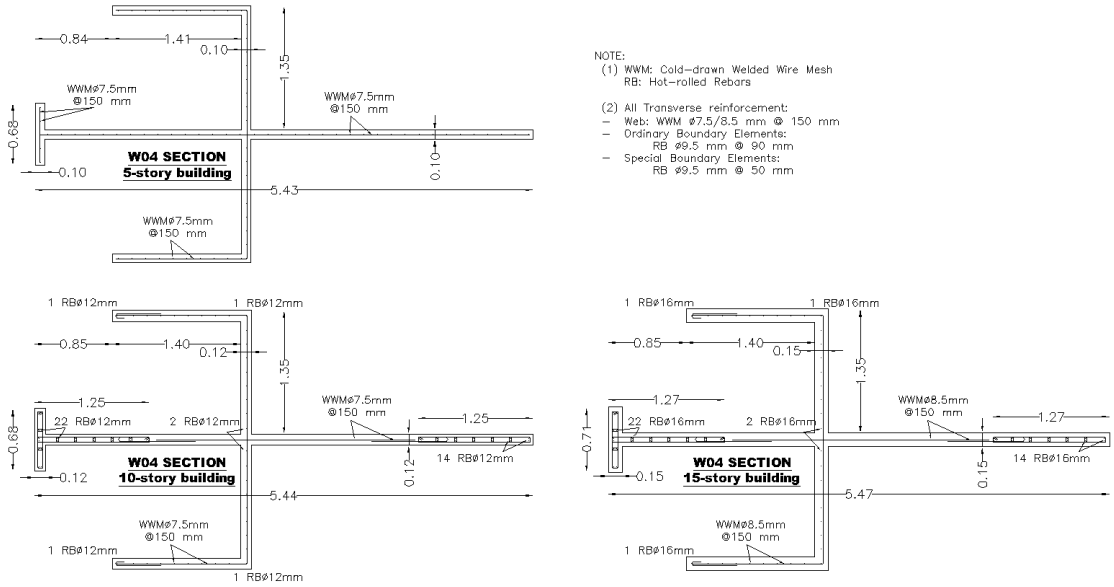

Figure 2.6 – Comparison of the reinforcement configuration provided for the W04 wall piers in the 5-, 10- and 15-story buildings. Units: meters

Chapter 3 –Hazard-Consistent Ground Motion Selection and Risk Assessment

This chapter describes the seismic hazard in the Andean region of Colombia and particularly in the city of Armenia. This city was chosen as a case study because there is a history of high seismicity in the area. The hazard in the city is dominated by different tectonic settings that result in the probability of occurrence of multiple causal earthquakes. Initially, a review of the historical seismicity of the region is made, highlighting the events that have caused the most widespread damage to the buildings in the city. Then, a seismicity model is proposed to quantify the contribution of the different tectonic settings to the seismic hazard in the city by means of a probabilistic seismic hazard analysis (PHSA). Lastly, the Conditional Scenario Spectra (CSS) (Arteta & Abrahamson, 2019) ground-motion selection methodology is extended to consider multiple causal earthquakes. The resulting set of ground motion records have spectral shape and assigned rates of occurrence that reproduce the hazard at the site and cover a wide range of intensities. This set can be used to estimate the expected structural response of a building subjected to different hazard levels by means of multiple nonlinear response history analyses. The obtained structural responses can be coupled with the assigned rates of occurrence of the ground motions to estimate the seismic risk to which the case-study structures are subjected.

3.1 Tectonic setting of the case-study site

Colombia is located in the most northwestern region of South America, where the South American, Caribbean and Nazca tectonic plates converge. The Nazca plate is subducted eastward beneath the South American plate on the Pacific coast at an approximate rate of 70 mm/year, while the Caribbean plate does the same in the southern direction at a rate of 10 mm/year (Kellogg & Vega, 1995). The interaction of these plates resulted in the formation of a complex system of crustal active zones in the South American plate and is responsible for the formation of the Andes Mountains and the Sierra Nevada de Santa Marta. In particular, the city of Armenia is located in one of the most active areas of Colombia, due to its proximity to the Romeral Fault System. A rupture in this fault system resulted in the 1999 M_w 6.1 Coffee Region ("Eje Cafetero" in Spanish) earthquake, which left 1,230 dead and an estimated economic loss of USD 1.9 billion (Restrepo & Cowan, 2000). **Figure 3.1** shows some of the major active zones in Colombia, including the Romeral and Cauca Fault Systems, and the Pacific subduction zones.

Earthquakes in the central-western Andean region of Colombia are produced by two main tectonic settings (Bonett, 2003; Restrepo & Cowan, 2000). The first and closest tectonic source is the Cauca-Romeral Fault System, whose crustal fault paths are a few kilometers away from the urban center of Armenia. This fault system is responsible for the notably destructive 1983 Popayán (M_w 5.5) and 1999 Armenia (M_w 6.1) earthquakes. The earthquakes generated by this system are not usually large in magnitude, but its proximity

to many urban centers in the Andean region is high enough to likely result in high-intensity ground motions. For these reasons, the Cauca-Romeral fault system is considered the major contributor to the seismic hazard in the Armenia and other major cities in the Coffee Region. The second main contributors to the seismic hazard in the region are the intermediate-depth earthquakes resulting from the slipping of a deep portion of the Nazca plate, at depths of 80 to 100 km beneath the Cordilleras. These intermediate-depth subduction earthquakes occur along inclined narrow zones of intraslab seismicity within the Wadatti-Benioff region. Subduction earthquakes are usually larger in magnitude and occur more frequently than crustal earthquakes. Large-magnitude earthquakes also occur at the convergent plate boundaries of the Nazca and South American plates near the Pacific Colombian coast. These earthquakes, called interface earthquakes, occur at shallow depths and have historically caused great damage to nearby cities (e.g. 1906 M_w 8.8 and 1979 M_w 8.1 Tumaco earthquakes). However, because Armenia is more than 200 km from the coast, few interface earthquakes have generated significant ground motion intensities in the city and are often considered to be minor contributors to the hazard.

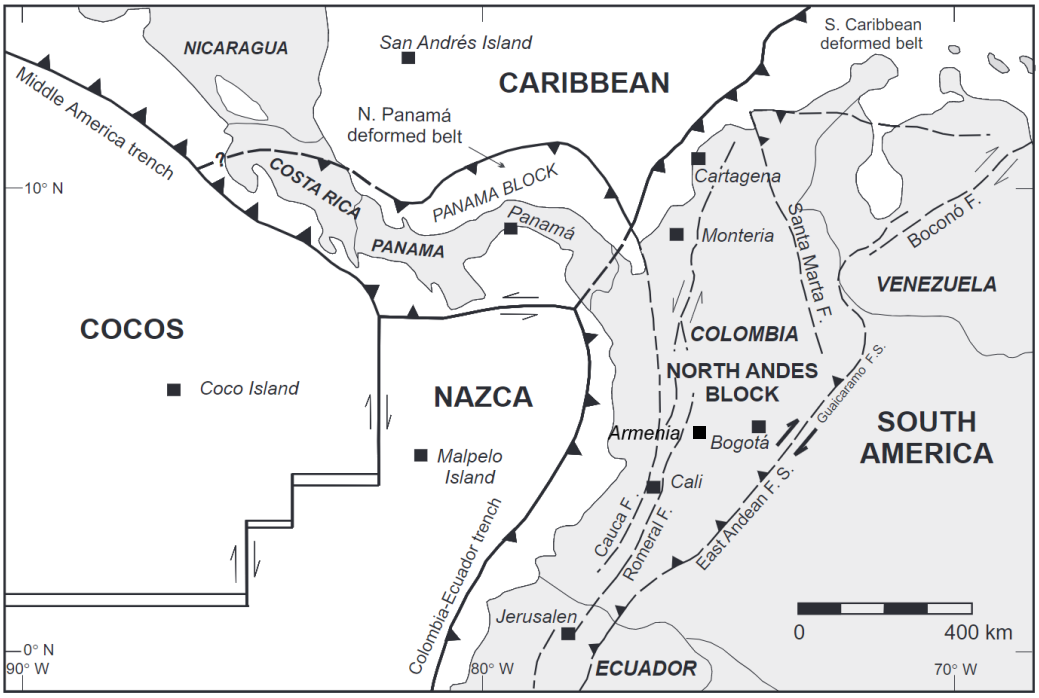

Figure 3.1 – Major tectonic characteristic and active zones in Colombia (Modified from Kellogg & Vega, 1995; Velandia et al., 2005).

3.2 Main earthquake events in the region

The Colombian Coffee Region is one of the most seismically active areas in the country. Some of the important cities in this area are Armenia, Manizales and Pereira. The region has an estimated population of 2,270,000 inhabitants (DANE, 2018). Diverse tectonic sources are responsible for the seismic events registered in the zone, with the most significant being the earthquakes coming from the Pacific subduction zone and the associated with the active crustal faults that run through the Colombian cordilleras. **Figure**

3.2 shows the epicenters of some of the major earthquakes recorded in the region (CIMOC & CEDERI, 2002; Servicio Geológico Colombiano, 2017). Only events with $M_w \geq 5.0$ or that caused moderate to severe damage in the Coffee Region are included. The corresponding metadata is presented in **Table 3.1**. Historical records indicate that intermediate depth subduction earthquakes are usually larger in magnitude and have repeatedly damaged towns along the Cordillera Central: 1961 M_s 6.8, 1962 M_w 6.5 and 1979 M_w 7.2 Eje Cafetero earthquakes, 1992 M_w 7.1 Murindó and 1995 M_w 6.4 Calima (Restrepo & Cowan, 2000).

Crustal earthquakes, though less frequent, also contribute significantly to the seismic hazard of the region. The January 25, 1999 M_w 6.1 Earthquake resulted from the rupture of a segment of the Romeral crustal fault system where no significant historical seismicity had been documented previously. The Colombian Geological Survey (SGC) (SGC, 2017) located the epicenter of the earthquake at 4.4° N, 75.7° W, about 15 km away from the urban center of Armenia (see **Figure 3.2**, top right). The event had an estimated depth of 15 km. The characteristics of the earthquake and its aftershocks indicated a steeply-dipping rupture restricted to the upper 20 km of the crust (Restrepo & Cowan, 2000).

Figure 3.3 shows the response spectra of the horizontal components of the 1999 Armenia earthquake recorded at the station Universidad del Quindío, Armenia. Recorded PGA was approximately 0.60 *g*. Spectral intensities $S_a \geq 1.0$ g are observed in the range $0.05 \leq T \leq 0.60$ s. The recorded ground motion spectra ($\zeta = 5\%$) are compared with the mean spectrum and variability predicted by the Sadigh et al. (1997) ground motion model for conditions similar to the event ($M_w = 6.1$, $R = 18$ km, deep soil). The elastic design NSR-10 spectrum is also included as a reference (Site Class D). For $T \leq 0.6$ s, the record spectra have intensity values around 3 times greater than the mean predicted by the Sadigh et al. (1997) model and about 2 times greater than those of the NSR-10 spectrum. For $T > 0.6$ s, the record spectra and the one predicted by Sadigh et al. (1997) have similar values of intensity, much lower in both cases than the values of the NSR-10 spectrum.

Table 3.1 – Notable historical earthquakes that affected the Colombian Coffee Region (CIMOC & CEDERI, 2002; Servicio Geológico Colombiano, 2017).

Date [yyyy-mm-dd]	Epicenter	Lat. [N]	Long. [W]	Depth [km]	MSK Intensity	Magnitude	Tectonic setting
1785-07-12	Southeastern Cundinamarca	3.0	74.3	10	IX	7.1	Crustal
1827-11-16	Altamira (Huila)	1.8	75.5	15	X	7.1	Crustal
1875-05-18	Cúcuta (Norte de Santander)	7.9	72.4	15	X	6.8	Crustal
1878-02-09	Los Nevados National Park	4.8	75.5	25	X	---	Crustal
1878-09-09	Los Nevados National Park	4.8	75.5	---	VII	---	---
1885-05-25	El Tambo (Cauca)	2.9	76.5	15	VIII	6.4	---
1906-01-31	Pacific Coast	1.0	79.4	20	X	8.8	Interface
1917-08-31	Villavicencio (Meta)	3.8	74.0	15	IX	6.7	
1923-12-22	Medina (Cundinamarca)	4.6	73.4	15	IX	5.9	Crustal
1924-01-10	Cartago (Valle del Cauca)	4.7	76.1	---	VI	---	---
1925-06-07	Tuluá (Valle del Cauca)	4.0	76.1	120	VII – VIII	6.1	Intraslab
1938-02-04	Eje Cafetero	4.7	75.7	150	VIII	7 (M_s)	Intraslab
1961-12-20	Eje Cafetero	4.5	75.5	163	VII	6.8 (M_s)	Intraslab
1962-07-30	Eje Cafetero	5.2	76.4	64	VIII	6.5	Intraslab
1967-07-29	Betulia (Santander)	6.7	73.0	161	IX	6.8	Intraslab
1973-04-03	Salento (Quindío)	4.6	75.6	150	VII	6.2	Intraslab
1973-04-24	Santa Rosa de Cabal (Risaralda)	4.9	73.6	19 – 118	VII	5.5	---
1979-11-23	Eje Cafetero	4.7	76.2	110	VIII	7.2	Intraslab
1986-11-29	San José del Palmar (Chocó)	5.1	76.7	90	V – VI	5.5	---
1990-11-23	Pijao (Quindío)	4.3	75.4	129	V	6.1	Intraslab
1991-11-19	Pacific Coast	4.5	77.3	18.5	IX	7.2	Interface
1992-10-18	Murindó (Antioquia)	7.1	76.8	10	X	7.1	Crustal
1995-02-08	Calima-Darién (Valle del Cauca)	4.1	76.6	71	VII	6.4	Intraslab
1995-08-19	Apia (Risaralda)	4.6	75.4	118	VI	4.7	Intraslab
1999-01-25	Armenia (Quindío)	4.4	75.7	15	VIII	6.1	Crustal
2008-09-13	Santa Rosa de Cabal (Risaralda)	4.8	75.5	133	---	5.7	Intraslab
2012-09-30	La Vega (Cauca)	1.9	76.4	170	---	7.3	Intraslab
2019-03-23	Versalles (Valle del Cauca)	4.5	76.2	122	---	6.1	Intraslab

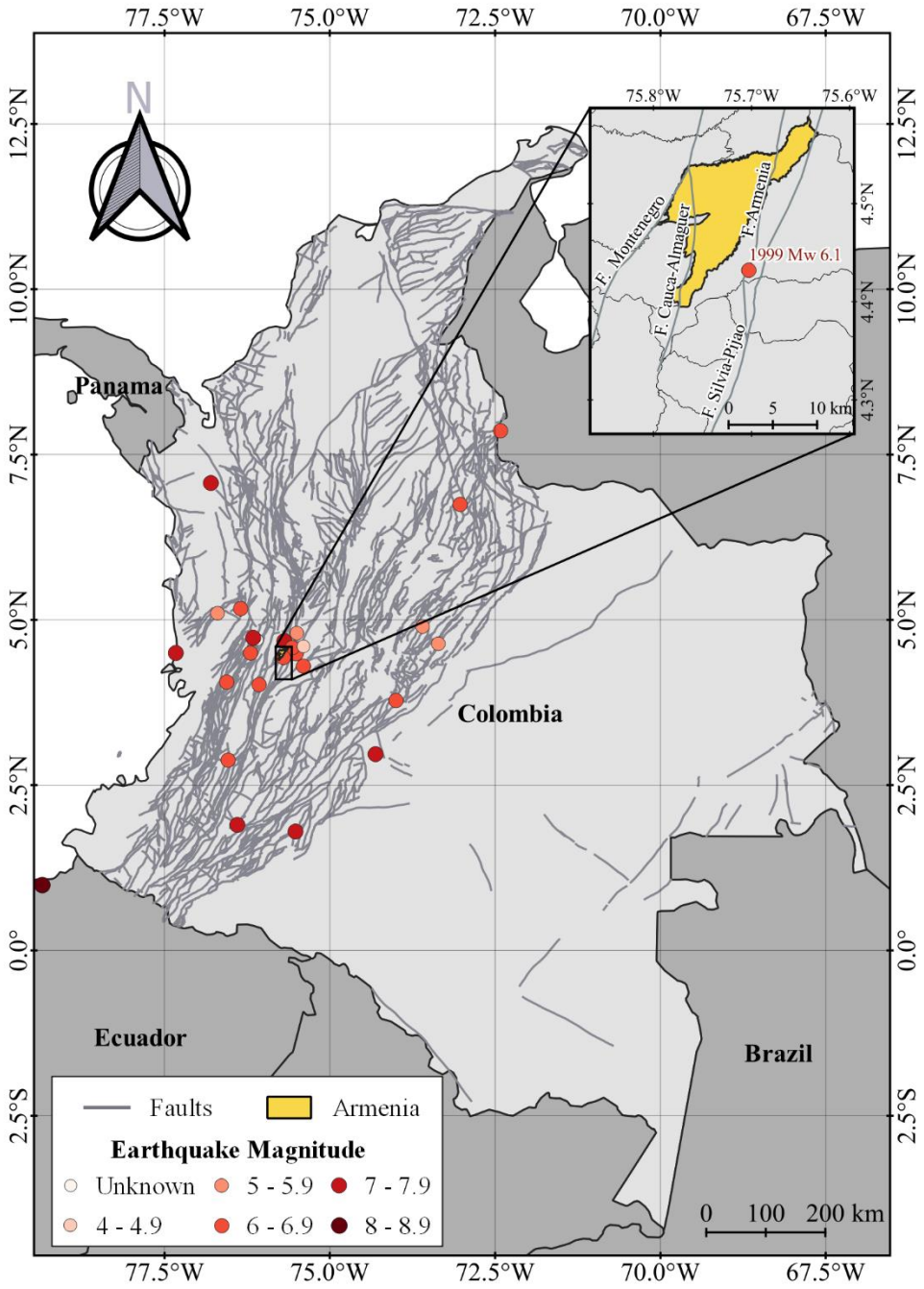

Figure 3.2 – Geological map of Colombia showing the epicenter of major historical earthquakes that have affected the city of Armenia, highlighting the January 25, 1999 M_w 6.1 earthquake (created with data from CIMOC & CEDERI, 2002; Servicio Geológico Colombiano, 2017, 2018).

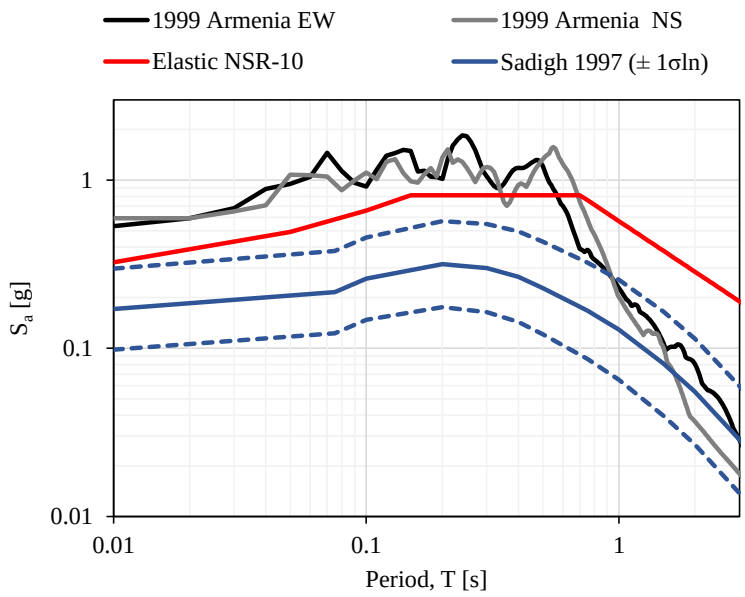

Figure 3.3 – Horizontal strong ground motion spectra (ζ = 5%) of the January 25, 1999 M_w 6.1 earthquake recorded at the station Universidad del Quindío, Armenia (Restrepo & Cowan, 2000). For comparison, the Elastic design NSR-10 spectrum (Site Class D) and the mean spectrum and variability predicted by the Sadigh et al. (1997) ground motion model (M_w = 6.1, R = 18 km, deep soil and ±1 σ_{lnSa}).

3.3 Seismic hazard assessment

The seismic hazard in Colombia has been studied by various researchers for more than 40 years. Most published studies have been associated with updates to earthquake-resistant construction regulations (Comité AIS 300, 1984, 1996, 2010; Salgado-Gálvez et al., 2016). The Salgado-Gálvez et al. (2016) served to establish the seismic design coefficients in the Colombian Seismic Resistant Design Code for Bridges (CCP-14). Salgado-Gálvez et al. (2016) used the same tectonic model developed for the estimation of the NSR-10 seismic hazard maps, but introduced changes in the seismicity parameters and ground motion models (GMMs) associated to the seismic sources, obtained through genetic algorithms calibrated with local records. This tectonic model is available in state-of-the-art seismic hazard platforms such as *Seismic Hazard* (Candia et al., 2019), making it easy to use for seismic hazard assessment of any site of interest.

The seismic hazard assessment in Salgado-Gálvez et al. (2016) was characterized by using a simple tectonic model and ground motion models that resulted in conservative seismic design coefficients. Considering these aspects, the Colombian Geological Survey (abbreviated SGC in Spanish) presented a new seismic hazard model for the country (Arcila et al., 2020). This model incorporated improvements in the definition of the geometry of the seismic sources, the seismicity parameters of the subduction sources and in the selection of GMMs that better represent the intensities observed in the different tectonic environments. The results of the seismic hazard assessment for rock sites using this model are available online (Servicio Geológico Colombiano, 2020).

Although the Arcila et al. (2020) model has significant improvements over the Salgado-Gálvez et al. (2016) model, its implementation by third parties for non-rock sites

is more complex because its tectonic model is not yet available in most seismic hazard platforms. For that reason, this research uses the Salgado-Gálvez et al. (2016) tectonic model modifying the seismicity parameters and GMMs associated to each seismic source to be aligned with the most recent SGC study. The resulting seismic model was implemented in *SeismicHazard* 1.0 (Candia et al., 2019), by modifying the input files available for Colombia by default. This platform features several modules that allow the user to perform probabilistic seismic hazard analysis (PSHA), estimate conditional mean spectra (CMS) and select ground motion records for the estimation of conditional scenario spectra (CSS). The input file used to generate the model can be found in **Appendix A**.

This research uses probabilistic methodologies (PSHA) to assess the seismic hazard to which the building archetypes presented in **Chapter 2** are exposed. These methodologies consider the uncertainties in aspects such as the location, magnitude and expected ground accelerations of future earthquakes. The PSHA is composed of four stages: (i) definition of the seismic source geometry and tectonic classification, (ii) selection of the seismicity model and estimation of its parameters, (iii) selection of the GMMs and assignment to the seismic sources and (iv) calculation of the seismic hazard. Each of these stages is presented next.

3.3.1 Seismic source geometry and tectonic classification

Based on existing information on seismicity in Colombia, Salgado-Gálvez et al. (2016) identified different faults that were grouped into 38 seismic sources represented as areal sources. Each one of them is described by a plane constructed from several vertices which not only accounts for its plan location, but also for its depth and dip angle. **Figure 3.4** presents the geometry of the seismic source model used in this research for the hazard assessment of the city of Armenia, highlighting the five major contributors to the seismic hazard at the case-study site. The sources are classified in three mechanisms according to their assigned scenarios: shallow crustal, and interface and intraslab subduction earthquakes.

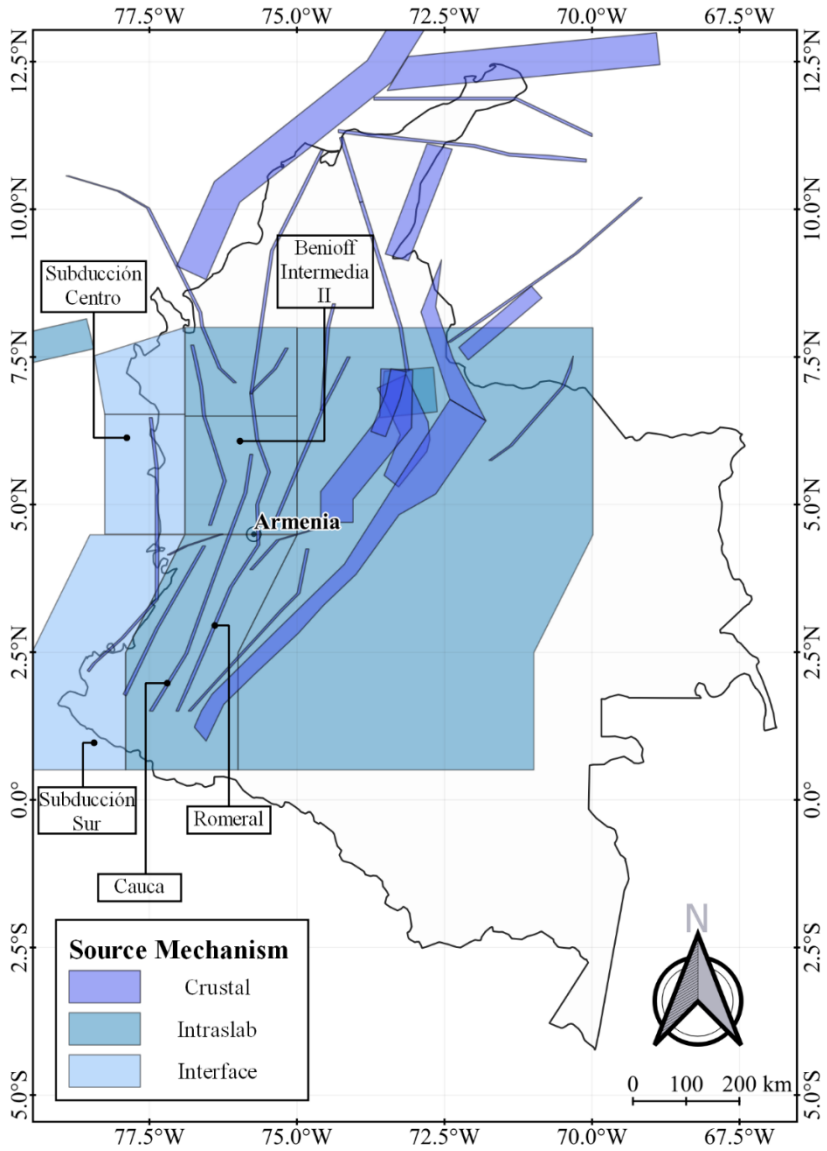

Figure 3.4 – Geometrical features of the 38 identified seismic sources as modeled in *SeismicHazard* along with localization of the site of interest.

3.3.2 Seismicity model

The occurrence of earthquakes in each seismic source is simulated following the Cornell and Vanmarcke (1969) relationship, which is a modified version of the Guttenberg and Richter (1944) relationship. This approach estimates the annual rate of exceedance $\lambda(M > m)$ of earthquakes with magnitude $M > m$ using **Equation (3.1)**, where m_{min} and m_{max} are the established magnitude limits for each source, and b is the slope of the logarithmic regression.

$$\lambda(M > m) = \lambda(M > m_{min}) \frac{10^{-b\,m} - 10^{-b\,m_{max}}}{10^{-b\,m_{min}} - 10^{-b\,m_{max}}} \tag{3.1}$$

The original geometric model from Salgado-Gálvez et al. (2016) has 38 seismic sources that simulate the hazard at the national level. Five of these sources contribute to 95% of the hazard in the city of Armenia, whether due to its shorter distance to the case-study site or historical associated seismicity. The identified major sources are labeled in **Figure 3.4**. It was found that any change in the seismicity parameters of these sources resulted in significant changes in the predicted hazard. To save computational resources in the computation of the hazard, the seismic source model was reduced to only include the previously mentioned sources. Then, the seismicity parameters ($\lambda(M > m)$, m_{min}, m_{max} and b) assigned to these sources were updated to better simulate the hazard predicted by the SGC model on rock sites. **Table 3.2** presents the resulting optimized values.

Table 3.2 – Simulated seismicity parameters and characteristics of the five most contributing sources to the seismic hazard in Armenia, Colombia.

Source	Mechanism	m_{min}	m_{max}	$\lambda(M_i > m_{min})$	b-value	GMM
Benioff Intermedia II	Intraslab	6.0	7.0	0.1224	0.768	Zhao et al. (2006)
Cauca	Crustal	5.0	7.0	0.1057	0.605	Sadigh et al. (1997)
Romeral	Crustal	5.0	7.0	0.1057	0.605	Sadigh et al. (1997)
Subducción Centro	Interface	6.0	9.0	0.0601	0.689	Montalva et al. (2017)
Subducción Sur	Interface	6.0	9.0	0.0601	0.636	Montalva et al. (2017)

3.3.3 Ground motion models (GMMs)

One of the necessary steps for the estimation of the seismic hazard of a site is the selection of a ground motion model that is consistent with the seismicity of the site. This requires the categorization of the seismic sources according to their fault mechanism. In this research, the seismic sources were classified as crustal, and interface and intraslab subduction sources. Arcila et al. (2020) defined unique logic trees for each source type and calibrated the weights assigned to various GMMs based on an extensive catalog of earthquakes recorded in the country. The author encourages readers to consult the original source for more details. In order to facilitate subsequent CMS and CSS calculations, only one GMM per source type was used in this research. The selected GMMs correspond to those that were best matched with the SGC hazard predictions on rock sites. As a result, crustal sources were modeled using the ground motion model (GMM) proposed by Sadigh et al. (1997). Similarly, the relations proposed by Montalva et al. (2017) and Zhao et al. (2006) were used to simulate the hazard in interface and intraslab subduction sources, respectively.

3.3.4 Probabilistic seismic hazard assessment (PSHA)

The seismic hazard at the site resulting from n sources is estimated using **Equation (3.2)**, where $\lambda(S_a(T) > z)$ is the annual rate of exceedance of the limiting value z of spectral acceleration S_a corresponding to a given structural period T, M_i and R_i are the earthquake magnitude and distance distributions for the source i, $\lambda(M_i > m_{min})$ is the annual rate of earthquakes with magnitudes greater or equal to m_{min}, $f_{Mi}(m)$ and $f_{Ri|Mi}(r|m)$ are the probability density functions of the plausible earthquakes scenarios (m, r), and $P(S_a(T) > z \mid m, r)$ is the conditional probability of exceeding a test value z of spectral acceleration $S_a(T)$ given an earthquake scenario (m, r). The first group of parameters, $\lambda(M_i > m_{min})$, $f_{Mi}(m)$ and $f_{Ri|Mi}(r|m)$, are defined along with the source geometry and magnitude recurrence relationships of the seismic source model. The probability

$P(S_a(T) > z \mid m, r)$ is estimated assuming that S_a is a random variable following a log-normal probability distribution with mean and standard deviation given by the GMMs assigned to each source.

$$\lambda(S_a(T) > z) = \sum_{i=1}^{n} \lambda(M_i > m_{min}) \int_{m_{min}}^{m_{max}} \int_{0}^{r_{max}} P(S_a(T) > z \,|m,r) f_{M_i}(m) f_{R_i|M_i}(r|m)\, \mathrm{d}r\, \mathrm{d}m \quad (3.2)$$

Figure 3.5a compares the seismic hazard predicted by the recent SGC (2020) model and that of the simplified model implemented herein for the city of Armenia, assuming firm rock site conditions. The rates in the hazard curves of both models are in the same order of magnitude, which is reflected in both models producing uniform hazard spectra (UHS) with similar intensity values S_a for structural periods $T \geq 0.2$ s (**Figure 3.5b**). This range includes the fundamental periods of the three case-study buildings. For short structural periods ($T < 0.2$ s) and high hazard levels (rate < 1×10^{-3} or return period $T_R > 975$ years), the spectral accelerations predicted by the SGC model are about 10% higher than those of the model proposed here.

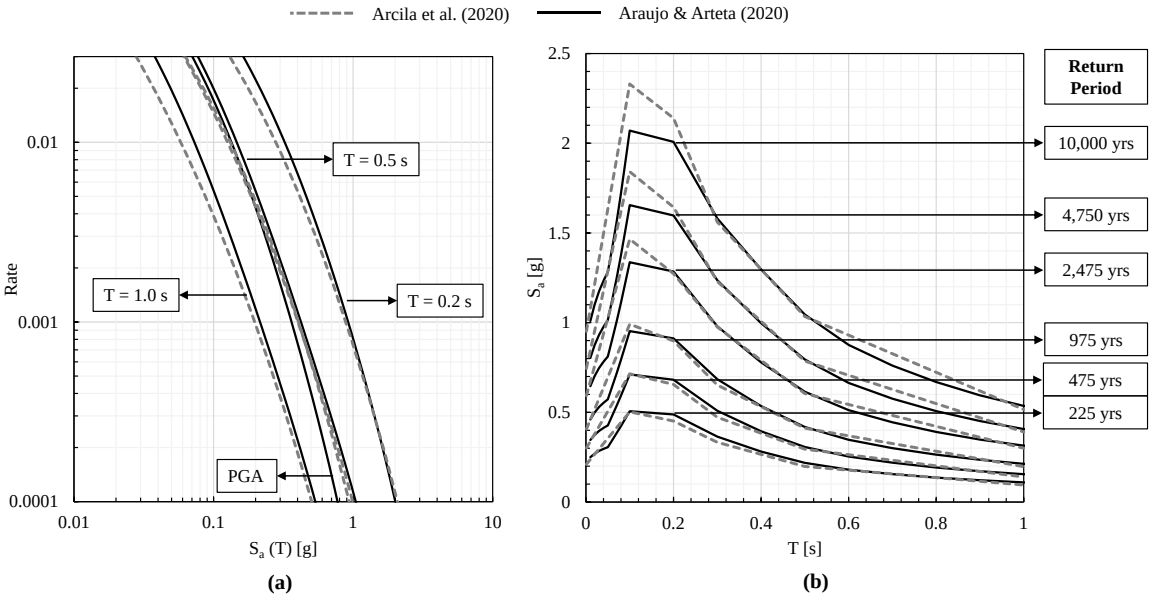

Figure 3.5 – Comparison between the (a) seismic hazard curves and (b) uniform hazard spectra predicted by the simplified model implemented in this research and the recent SGC (2020) model assuming firm rock site conditions in the city of Armenia.

Once it is verified that the proposed seismic hazard model yields consistent results when compared to the more sophisticated SGC model, the PSHA is repeated by changing the soil conditions. This is done by changing the average shear wave velocity of the upper 30 m of soil (V_{s30}) (see **Appendix A**). A V_{s30} = 300 m/s is assumed, which is consistent with Site Class D. **Figure 3.6** presents the resulting hazard curves for different structural periods and different source mechanisms. The total hazard curve is the result of adding the contribution from each source following **Equation (3.2)**. The curves show that the hazard is dominated by intraslab sources for structural periods $T \leq 0.5$ s. For more flexible

structures ($T > 0.5$ s), the three identified source mechanisms contribute to the seismic hazard in similar proportions. In general, for low hazard levels (rate > 4×10^{-3} or $T_R < 250$ years), the hazard is dominated by intraslab sources, followed by interface and crustal sources. For higher hazard levels, crustal sources contribute the most, followed closely by interface sources. As there is no single dominant source type for the range of structural periods of the study buildings, the methodology used for risk assessment must consider the contributions to the hazard of each source type in its respective proportions.

Figure 3.7 shows the UHS for different return periods resulting from the total hazard curves of the case-study site (V_{s30} = 300 m/s) presented in **Figure 3.6**. The range of structural periods of the building archetypes is shown in the shaded area of the plot. The elastic NSR-10 design spectrum (Site Class D) is also included for comparison. An approximation to the strength of a typical RC wall building can be obtained multiplying the elastic NSR-10 spectrum by the factor Ω/R. This capacity spectrum is also shown **Figure 3.7**, assuming $\Omega/R = 2/5$. Maximum spectral accelerations in the set of UHS are observed in the range $0.2 \text{ s} \leq T \leq 0.4$ s. For longer periods ($T \geq 0.4$ s), the spectral accelerations decrease at a rate proportional to a factor between $1/T$ to $1/T^2$. On the other hand, the NSR-10 spectrum has a spectral shape whose constant acceleration region covers a wider range of periods. This is the result of the use in NSR-10 of seismic coefficients that mimic the ASCE 7 design spectrum, with soil coefficients consistent with NEHRP provisions. In consequence, the spectral ordinates of the NSR-10 spectrum extend over different hazard levels. For structural periods $T \leq 0.4$ s, the NSR-10 spectral accelerations approximate the 475-year UHS. For longer structural periods, the NSR-10 spectral ordinates can be as greater as those of the 2,475-year UHS. This contrasts with the hazard assigned by the NSR-10 to the design spectrum, which is a uniform probability of exceedance of 10% in 50 years (475-year return period) at all structural periods. Similar observations with respect to the NSR-10 spectral shape have been documented in the past (Comité AIS 300, 2010). This implies that if all structures designed according to NSR-10 had an overstrength factor $\Omega = 2.5$, those with structural periods $T \geq 1.0$ s would be designed to resist seismic demands associated with much longer return periods than their more rigid counterparts (see the capacity spectrum shown in dotted lines in **Figure 3.7**).

Another main result from a PSHA is the hazard deaggregation. The hazard deaggregation gives the fractional contribution of different scenario pairs (M, R) to the total hazard. **Figure 3.8** shows the contribution of the (M, R) pairs to the seismic hazard at $T = 0.5$ s for two different return periods (i.e. different hazard levels). Major contributions to the hazard level of 2.1×10^{-3} (T_R = 475 years) are dictated by earthquakes scenarios with a distance to seismic source in the range $80 \leq R \leq 150$ km and earthquake magnitude $6.0 \leq M \leq 7.0$, though closer earthquake scenarios ($R \leq 30$ km and $5.5 \leq M \leq 7.0$) have also significant contributions. For the hazard level of 4.0×10^{-4} (T_R = 2,475 years), the contributions from the closer and distant earthquake scenarios are in the same order of magnitude. Some minor contributions from larger-magnitude events ($80 \leq R \leq 150$ km and $7.5 \leq M \leq 9.0$) are also present in the 2,475-year hazard level. These multiple causal earthquakes are the result of the different tectonic settings at the site, and are consistent with the observed historic seismicity in the region. The next section of this chapter presents a methodology for hazard-consistent ground motion selection that consider the contributions to the seismic hazard of multiple causal earthquakes over a wide range of

hazard levels and structural periods. The selected records are useful for structural fragility analysis and risk assessment.

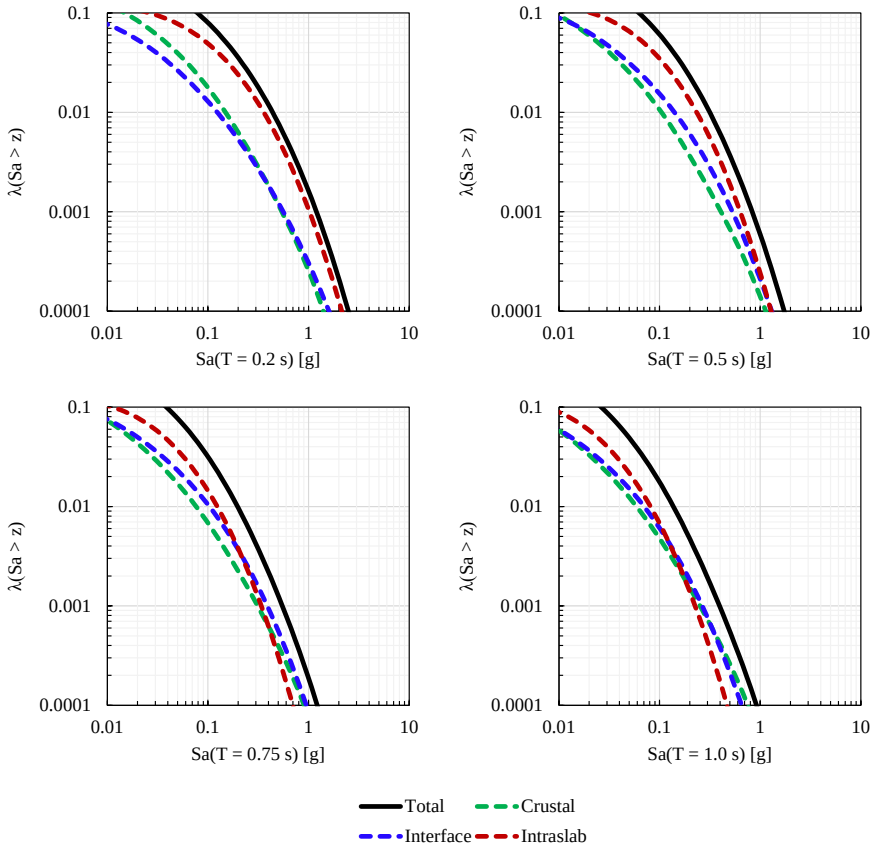

Figure 3.6 – Seismic hazard for the city of Armenia contributed from the different tectonic settings (V_{s30} = 300 m/s).

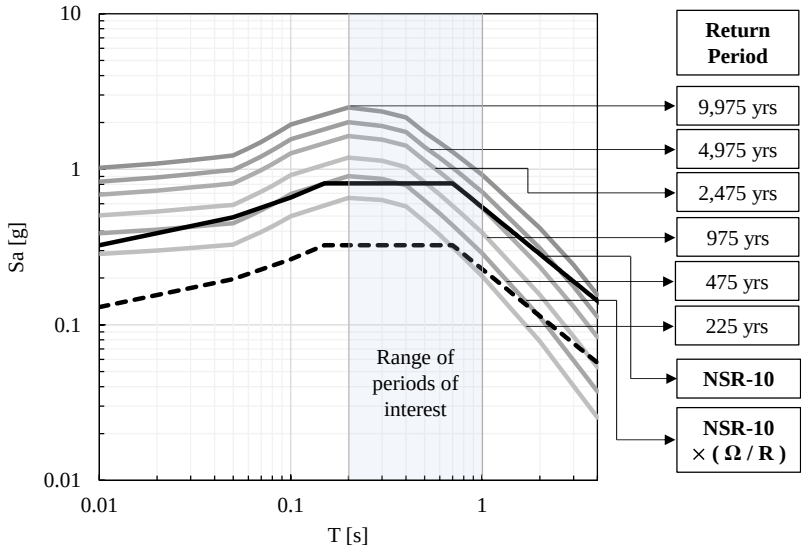

Figure 3.7 – Uniform hazard spectra for stiff soil sites (V_{s30} = 300 m/s) in the city of Armenia in comparison with the elastic NSR-10 design spectrum (Site Class D).

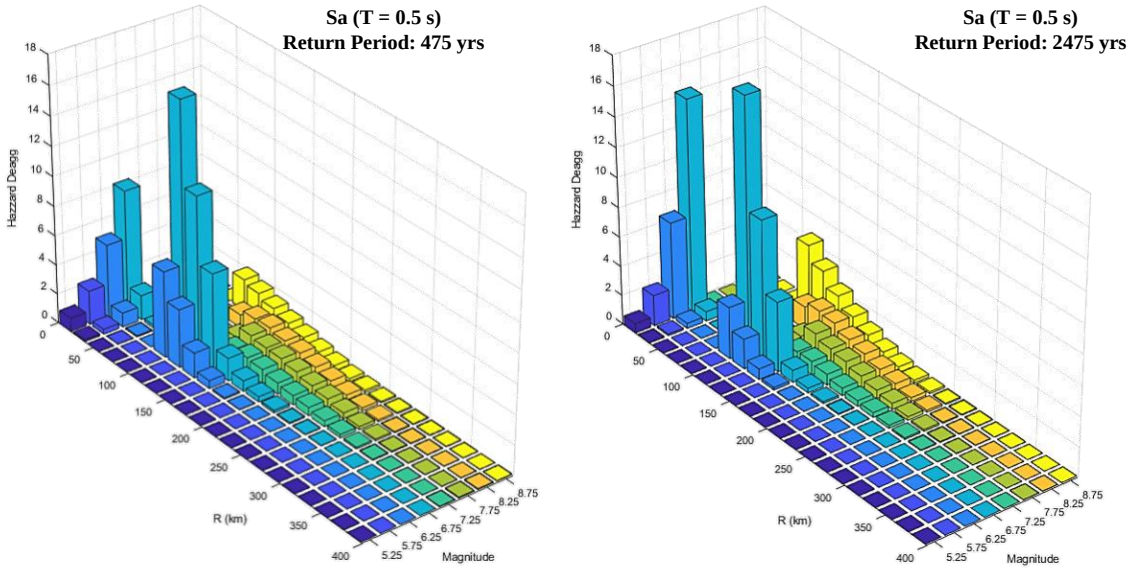

Figure 3.8 – Deaggregation of the seismic hazard (T = 0.5 s) at the site of interest for return periods of 475 and 2,475 years.

3.4 Conditional Scenario Spectra (CSS)

The seismic response of the building archetypes is evaluated in this study using non-linear dynamic analyses. In these analyses, the structure is subjected to different ground motions whose intensity and spectral shape are representative of those expected at the site, as estimated in the PSHA. For this case, the results of the PSHA showed that the seismic hazard in the city of Armenia is the result of the interaction of diverse seismic sources, grouped in three different mechanisms. To consider this variability in the hazard and the contribution of the different tectonic settings, this study extends the Conditional Scenario Spectra (CSS) methodology (Arteta & Abrahamson, 2019) for the selection of ground motion records to include multiple causal earthquakes.

The CSS methodology is a hazard-consistent procedure for ground motion selection and subsequent assessment of the seismic response of a given structure. With this methodology, the analyst is able to link the simulated seismic behavior with the expected occurrence rate of the ground motion intensity to obtain an estimate of the annual rate of exceedance of a given engineering demand parameter (EDP). This annual rate, coined herein as EDP-risk, is estimated using a large suite of ground motion records selected to cover a wide range of intensities. Each ground motion is assigned an occurrence rate based on its spectral shape and intensity. The set of selected ground motions is known as the CSS. Details of the procedure for selecting ground motions and assigning occurrence rates can be found elsewhere (Abrahamson & Al Atik, 2010; Abrahamson & Yunatci, 2010). Other methodologies, such as the incremental dynamic analysis (IDA; Vamvatsikos & Cornell, 2001), also allow the generation of a set of records for a given range of intensities, but do not take into account the variability in the hazard and the spectral shape as the hazard level increases. The estimation of the CSS in this study is performed using the homonymous module available in *SeismicHazard*. The CSS module in this platform links the results of

the PSHA to an implementation in Fortran of the ground motion selection procedure developed by Al Atik and Abrahamson (2017).

The main result of the CSS methodology is a set of ground motions with assigned occurrence rates that when added together reproduce the seismic hazard at the site. For a CSS with *m* records, the simulated hazard $\lambda(S_a(T) > z)$ is given by **Equation (3.3)**, where $H(x)$ is the Heaviside function and $S_{a,i}(T)$ is the scaled spectral acceleration of the *i*-th ground motion. In simpler terms, this equation estimates the annual rate of exceedance of a given spectral acceleration, $S_a(T) > z$, for a given structural period T as the sum of the occurrence rates of all the ground motions with $S_a(T) \geq z$.

$$\lambda(S_a(T) > z) = \sum_{i=1}^{m} (rate_i) H\big(S_{a,i}(T) - z\big) \tag{3.3}$$

In this study it is of particular interest to reproduce not only the total hazard but also the contribution of each tectonic setting. Accordingly, a CSS was generated for each tectonic setting (three in total) using the hazard contributed exclusively by the sources associated with it. This is an extension of the Conditional Scenario Spectra (CSS) methodology proposed by Arteta and Abrahamson (2019), initially conceived for active crustal tectonic settings. The estimation of three independent ground motion CSS sets rather than one global CSS from the total hazard allows the consideration of multiple causal earthquakes for a given hazard level in the risk estimation. Recall from **Figure 3.8** that the hazard deaggregation exhibited at least two different predominant scenarios. Similarly, this approach accounts for the difference in the frequency content of the ground motions generated by each tectonic setting. The resulting combined CSS is a set of records whose assigned rates of occurrence are consistent not only with the total hazard but with the tectonic setting they represent.

The CSS methodology requires the definition of a finite number of hazard levels. At each level a CMS (Baker, 2011) is estimated, which is then used as a target to select the ground motion records that will constitute the CSS. The case-study buildings have initial fundamental periods in the range of 0.2 s to 1.0 s, so a reference period approximately in the middle of the range, T_o = 0.5 s, is selected for the estimation of the CMS at all hazard levels. The choice of an arbitrary conditioning period is based on observations that show that the CSS is usually not sensitive to the value of T_o (Lin et al., 2013). In addition to estimating a CMS for each hazard level, it is also necessary to estimate the variability of the CMS. This variability is determined from a spectral acceleration correlation model using the method from Jayaram et al. (2011). For ground motions originated by crustal earthquakes, the correlation coefficients from Baker and Jayaram (2008) were used, while the coefficients from Abrahamson et al. (2016) were used for interface and intraslab earthquakes.

Eleven hazard levels were defined to generate the CSS for each source mechanism, with rates of exceedance ranging from 3.2×10^{-2} (T_R = 31 years) to 1.0×10^{-5} (T_R = 99,975 years). These hazard levels were chosen so that the hazard resulting from the combination of each CSS set would represent the total hazard at the site obtained with the PSHA between hazard levels 1.0×10^{-2} (T_R = 100 years) to 5.0×10^{-5} (T_R = 20,000 years). The resulting combined CSS set comprises 348 two-component ground motion records,

123 of which simulate the hazard contribution from crustal sources, 106 from interface and 119 from intraslab subduction sources. Crustal ground motion records were selected from the NGA-West2 database (Ancheta et al., 2014), while subduction ground motions were obtained from the NGA-Sub database preliminary suite (Kishida et al., 2020). The selected and scaled RotD50 CSS for the three types of seismic source considered in this study are presented in **Figure 3.9**, along with the elastic NSR-10 design spectrum. The metadata of each of these records is presented in **Appendix B**.

Each of the ground motion records shown in **Figure 3.9** is assigned a rate of occurrence that is optimized to reproduce the hazard from the PSHA. **Figure 3.10** presents the hazard recovered by means of **Equation (3.3)** for each of the three CSS sets and compares it with the target hazard curves of the case-study site obtained with the PSHA. The total hazard is also computed as the sum of the contribution of each source mechanism. The target and recovered hazard curves are shown for hazard levels from 1.0×10^{-2} to 1.0×10^{-4} (return periods of 100 to 10,000 years) at three different structural periods. The recovered hazard curves are in good agreement with the target seismic hazard, with closer agreement observed for structural periods close to the reference period T_o = 0.5 s. Thus, the combined CSS set is able to reproduce the total hazard and its deaggregation by source mechanism. The simulation of the hazard deaggregation by source mechanism based on the occurrence rates assigned to the CSS set can be extrapolated to the EDP risk. In this way, the analyst can determine which types of earthquakes contribute most to the exceedance rate of a given EDP.

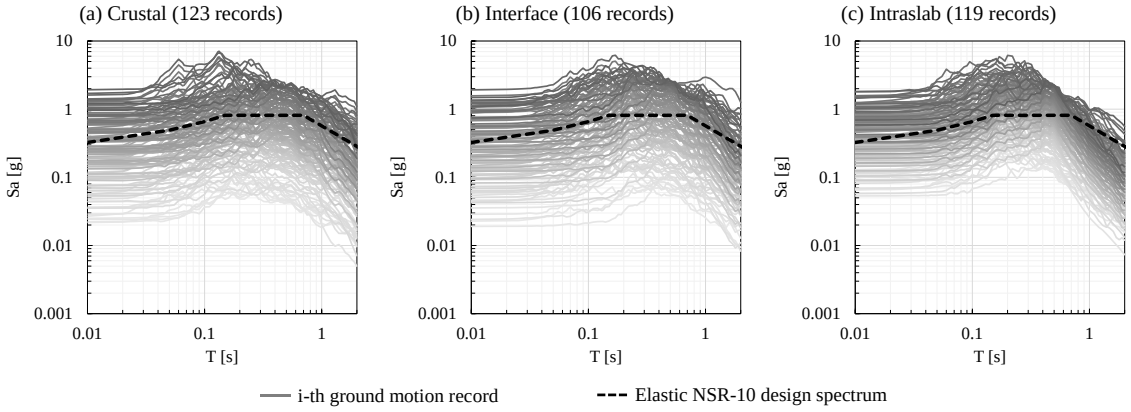

Figure 3.9 – Selected RotD50 CSS sets (ζ = 5%) for the three types of seismic sources considered in comparison with the elastic NSR-10 design spectrum.

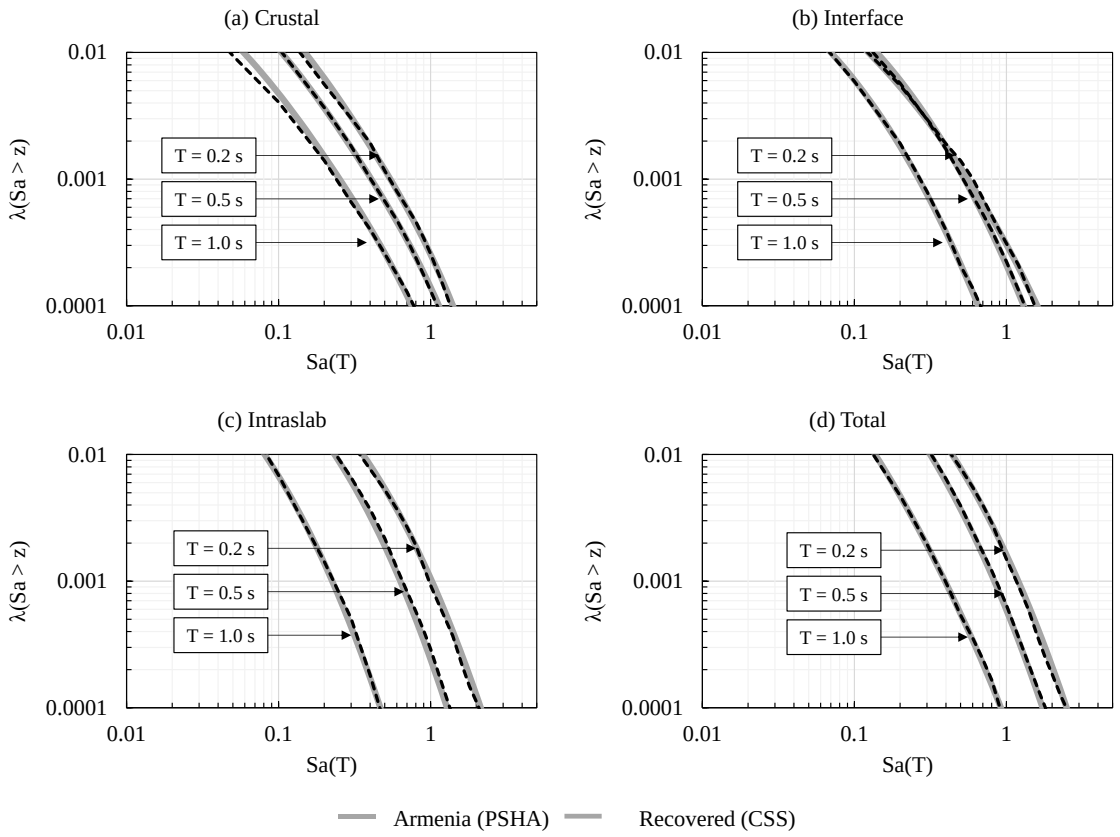

Figure 3.10 – Hazard curves at different structural periods and from different source mechanisms recovered with the CSS assigned rates.

3.5 Estimation of fragility curves and EDP-risk with the CSS

The CSS set can be used to find a correlation between the ground motion intensity (e.g. spectral acceleration S_a) and a given structural engineering response (EDP) by means of response history analyses (RHAs). Common EDPs at the global level of response are drift ratios and accelerations, while at the local level strains and curvature are more significant. The analyst can relate these responses to damage measures and establish performance limits (ASCE 41, 2017). In this research, the structural demands obtained with the CSS are used to determine the probability of exceedance of a certain EDP given different levels of spectral acceleration, $P(EDP > y \mid S_a(T_1) = x)$. Fragility curves are plots of $P(EDP > y \mid S_a(T_1) = x)$ versus $S_a(T_1)$, and are a description of the vulnerability. Intensity measures (IM) different from $S_a(T_1)$ may be chosen, as long as the engineering responses increase with increasing values of IM.

Figure 3.11 illustrates the estimation of fragility curves for three different levels of roof drift ratio (RDR_{max}) exhibited in an RC moment frame with a CSS set computed for the Yerba Buena Island in California. Details on the construction of the ground motion set and the numerical model are found in Arteta and Abrahamson (2019). The structural demands obtained from the RHAs are shown in **Figure 3.11a** in the form of a scattergram that relates RDR_{max} with the spectral acceleration $S_a(T_1)$. As expected, increasing values of $S_a(T_1)$ result in increasing RDR_{max} though great dispersion in the data is observed. Once the

responses from the CSS are gathered, the data is binned by intensity level $S_a(T_1)$. The probability of exceeding a specific value of $RDR_{max} = j$ at each intensity level is calculated by dividing the number of ground motions that result in values of $RDR_{max} > j$ by the total number of ground motions. The results are then fitted to a log-normal distribution as shown in **Figure 3.11b**. Buniya et al. (2020) found that the obtained fragility curves are usually insensitive to the bin size. Fragility curves shift to the right for larger values of RDR_{max}, indicating that large structural responses are associated with large ground motion intensities. On the other hand, the slope of the fragility curve depends on the dispersion of the data. Fragility curves computed with an IM that is a good response estimator exhibit consistent steep curve slopes for different values of EDP and less dispersion. More information of how to efficiently compute fragility curves is found in Baker (2015).

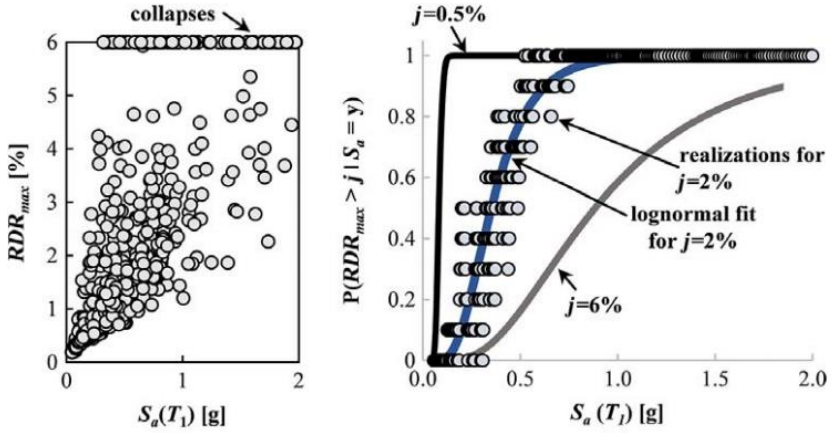

(a) (b)

Figure 3.11 – Estimation of fragility curves for the roof drift ratio (RDR_{max}) from CSS runs of an inelastic reinforced moment frame (Arteta & Abrahamson, 2019) .

The annual rate of exceedance of an EDP level y (EDP-risk) can be estimated from the PSHA hazard curves and the structural demands obtained from the nonlinear analyses using **Equation (3.4)**, where IM is any intensity measure specified by the analyst (e.g. $S_a(T_1)$), $P(EDP > y \mid IM = x)$ is the cumulative fragility function determined as in **Figure 3.11** and $\lambda(IM > x)$ is the annual rate of exceedance of the specified IM. This type of information is useful because it allows the expected behavior of the case-study structures to be evaluated from a hazard-consistent perspective (Arteta & Abrahamson, 2019). As each ground motion in the CSS has an assigned rate of occurrence, **Equation (3.4)** can be rewritten as the much simpler expression of **Equation (3.5)**. This latter expression is similar to the one in **Equation (3.3)** used to recover the seismic hazard with the CSS. As in the case of the seismic hazard, the EDP-risk may be computed using the combination of the three CSS sets or may be deaggregated by source mechanism to estimate the contribution of certain earthquake scenarios to the rate of exceedance of a given EDP.

$$\lambda(EDP > y) = \int_{IM_{min}}^{IM_{max}} \left(P(EDP > y|IM = x)\right)\left(-\frac{d\lambda(IM > x)}{dx}\right)dx \qquad (3.4)$$

$$\lambda(EDP > y) = \sum_{i=1}^{n.\ records} (rate_i) H(EDP - y) \tag{3.5}$$

The methodology described in this chapter offers an alternative for studying the response of a structure by consistently incorporating the seismic hazard contributed by different tectonic sources affecting the site of interest. This methodology becomes a powerful tool for decision-making by all the stakeholders. The procedures described here in conjunction with the selected ground motion sets will be used in Chapter 6 to estimate the vulnerability of thin RC wall buildings in Colombia and the risk to which these structures are exposed.

Chapter 4 – Nonlinear Model

This research uses nonlinear analyses to assess the expected behavior of the building archetypes defined in **Chapter 2** under static and dynamic lateral loading. A simplified two-dimensional (2D) model of the buildings is constructed in OpenSees (McKenna et al., 2010). The model allows to perform the large number of dynamic analyses required by the CSS methodology introduced in **Chapter 3** with significantly reduced running times.

4.1 Model configuration

Fragility assessment of the building archetypes is performed using a 2D model in OpenSees, with earthquake excitation applied only in the longitudinal direction. In this model, the behavior of RC walls is simulated using fiber-section force-based beam column (FBC) elements (Spacone et al., 1996) and uniaxial material relationships for concrete and steel reinforcement. Previous studies have demonstrated the capability of FBC models to reproduce global and local responses with reasonable accuracy for flexure-dominant specimens (Gogus & Wallace, 2015; Kolozvari et al., 2018; Pugh et al., 2015), while offering more moderate computational demands than finite element and other macroscopic models available. The formulation of FBC elements assumes coupled behavior between axial and flexural responses, while shear responses are uncoupled. Besides, it assumes that strains are linearly distributed along the wall section following the Euler-Bernoulli beam theory. While many approaches have tried to incorporate flexure-shear interaction in beam-column elements (Jiang & Kurama, 2010; Petrangeli et al., 1999), their associated computational demands and low numerical robustness make them unpractical for the present study. Linear distribution of strains is still a feature present in many macroscopic models, including those who incorporate flexure-shear interaction (Kolozvari et al., 2015a). An alternative modeling approach is the beam-truss model proposed by Yuan Lu and Panagiotou (2014), which accurately simulates the nonlinear distribution of strains based on a strut-and-tie approach. However, its computational demands are also high given the number of elements and degrees of freedom it requires (Arteta et al., 2019). Thus, the FBC modeling approach is selected in this study given its proven capabilities and the extensive computational work required to perform a comprehensive fragility assessment.

The simplified model is composed of 12 of the wall piers that constitute the structural layout of the system arranged in parallel. The selected elements are colored in black in the floor plan presented in **Figure 2.1**. A linear elastic model in ETABS® revealed that these walls resist 50% of the elastic design base shear in the EW direction and can therefore be considered as representative of the overall behavior of the case-study buildings. The inelastic response of wall elements is simulated using *forceBeamColumn* elements with distributed plasticity, following a scheme as in **Figure 4.1**. The Gauss-Radau and Gauss-Lobatto integration schemes with 3 and 4 IPs were found to be appropriate for the analysis. As later explained in **Section 4.3,** Coleman and Spacone (2001) demonstrated that inelastic deformations (i.e. deformations after the section response softens) in FBC elements localize in the first integration point (IP) and depend on the integration scheme used. Simulated inelastic deformations are only objective when the length of the first IP corresponds to the targeted and already calibrated plastic hinge length. Otherwise, local

deformations need to be postprocessed to obtain objective predictions. To avoid postprocessing, this study uses integration schemes with a length of the first IP that approximates the damage length l_p observed in thin RC walls: $2t_w \leq l_p \leq 3t_w$ (Blandón & Bonett, 2019; Segura & Wallace, 2018b; Takahashi et al., 2013; Wallace, 2011; Welt, 2015).

The flexural response of the elements is modeled using fiber-type sections and specified uniaxial constitutive relationships for concrete and steel. The shear response of the elements at the section level is assumed to be linear elastic. The slab-wall rigid joint is modeled using horizontal elastic rigid elements at each story level. Floor diaphragms are simulated using *equalDOF* constraints, not accounting for the bending stiffness of slabs. Consistent with linear analysis, mass is lumped at every story level and is equal to half the mass of the buildings (i.e. the 2D model accounts for 50% the mass and stiffness of the 3D model). The effects of expected gravity loads are modeled using the load combination 1.0*D*+0.25*L*. Geometrical nonlinearities are simulated using the *PDelta* geometric transformation, which reduces the tangent stiffness of the system by accounting for the action of the axial loading on the laterally deformed shape of the model. The selected modeling approach ignores the effects of soil-structure interaction and reinforcement slip, as well as coupling between axial-bending and shear actions.

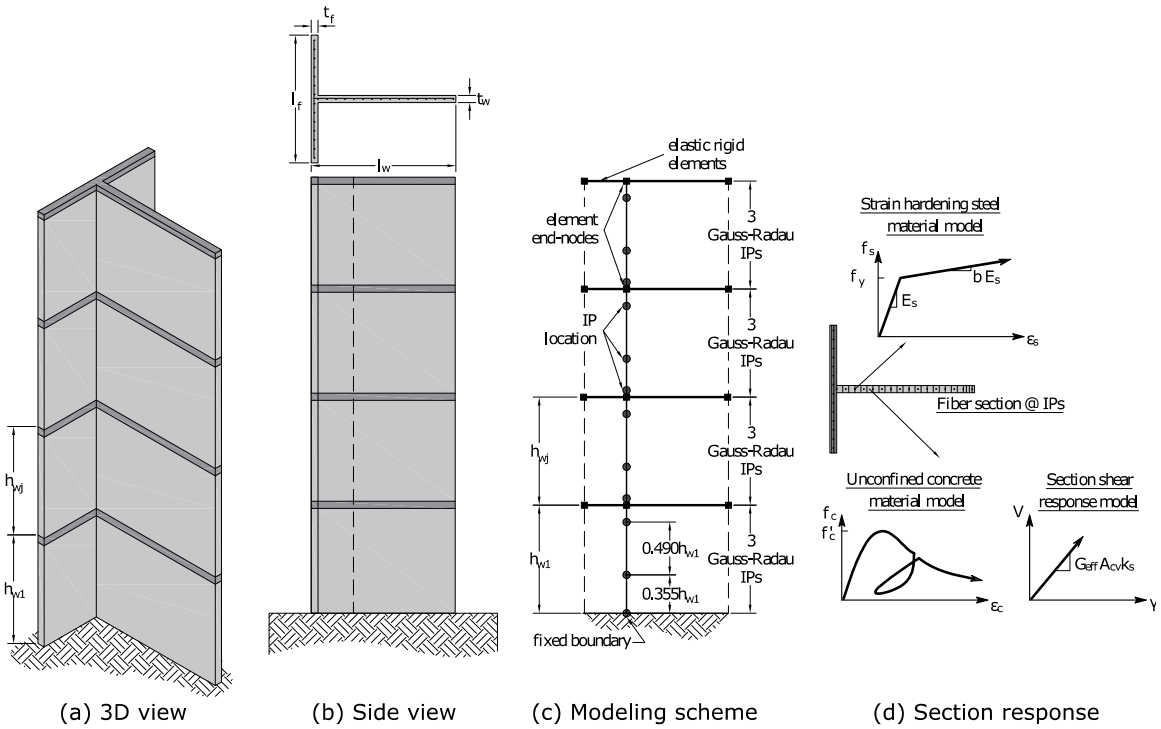

Figure 4.1 – Example of the simplified 2D modeling scheme of a multi-story RC wall in OpenSees.

4.2 Material constitutive relationships

The uniaxial behavior of concrete is simulated using the relationship proposed by Kent and Park (1971) and modified by Scott et al. (1982) to include the tensile behavior of concrete (available in OpenSees using *Concrete02*, see **Figure 4.3a**). The model follows the rules proposed by Mohd Yassin (1994), including gradual degradation of stiffness under

unloading and reloading in compression. The elastic modulus of concrete is assumed as $E_c = 3900\sqrt{f'_c}$ [MPa] per NSR-10, while the tensile strength is determined from the relationship $f_t = 0.33\sqrt{f'_c}$ [MPa] (Hsu, 1993; Vecchio & Collins, 1986).

The linear softening post-peak behavior of concrete, for both tensile and compressive responses, is regularized to limit mesh-sensitivity using the constant fracture energy approach (Bazant & Planas, 1998; Coleman & Spacone, 2001). Following this approach, the tension softening stiffness E_{ts} is determined using **Equation (4.1)**, where G_f is the fracture energy in tension and L_E is the length of the integration point for FBC elements in OpenSees. Reported values of G_f typically vary between 75 and 150 N/m (Lee & Lopez, 2014; Wittmann et al., 1988). This study uses $G_f = 100$ N/m, but the variability of this parameter does not significantly affect the simulated global response. Likewise, the ultimate compressive strain capacity ε_{c20} (at a residual stress $\sigma = 0.20f'_c$) is defined as in **Equation (4.2)** where G_f^c is the fracture energy in compression and ε_{c0} is the strain corresponding to the compressive strength f'_c. For unconfined concrete, results from experimental and analytical research (Mohammed & Barbosa, 2019; Nakamura & Higai, 2001; Pugh et al., 2015) suggest that G_f^c is a function of f'_c. Recommended values are typically around $G_f^c = 2f'_c$ mm. For the concrete in the SBEs of 15-story walls, the pre-peak response is simulated as in the case of unconfined concrete, while the post-peak response is regularized using $G_f^{cc} = 1.5G_f^c = 1.5(2f'_c$ mm) to account for the effects of the closely-spaced stirrups on compressive strain capacity. This results in $\varepsilon_{c20} = 0.015$, which is congruent with the lower bound of the experimentally-measured response of thin wall boundary elements under monotonic compression reported by Arteta (2015) shown in **Figure 4.2**.

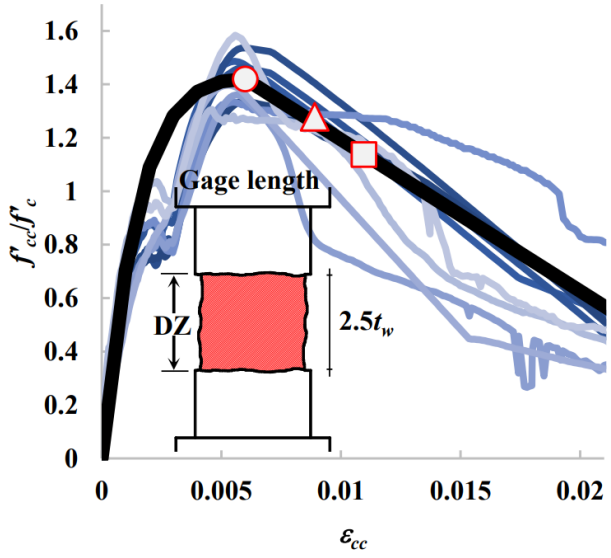

Figure 4.2 – Experimentally-measured compressive responses of thin boundary elements (in blue) and the fitted nonlinear model (in black) (Source: Arteta (2015)).

The monotonic envelope of the stress-strain model for reinforcing longitudinal steel is defined based on results from laboratory tests. Elastic modulus of steel is $E_s = 200$ GPa. Deformed bars are assumed to yield at $f_y = 490$ MPa (i.e. $f_{y,e} = 1.16f_{y,n}$), with ultimate tensile strength $f_{su} = 630$ MPa and an *experimentally measured* ultimate tensile strain

capacity $\varepsilon_{su,test}$ = 0.10. Electro-welded wire-meshes have proven to have greater yield strength and limited ductility. Based on results from Carrillo et al. (2019), wire-mesh bars are assumed to yield at f_y = 650 MPa, with f_{su} = 690 MPa and $\varepsilon_{su,test}$ = 0.015. The simple buckling model proposed by Pugh et al. (2015) is used to simulate the compressive response of steel reinforcement. This model assumes that reinforcing bars fail in compression when surrounding concrete reaches its ultimate compressive strain ε_{c20}. The cyclic response of steel is defined using the Menegotto and Pinto (1973) model modified by Kolozvari et al. (2015b), available in OpenSees as *SteelMPF*, and failure is modeled using the wrapper *MinMax*. As in the case of concrete in compression, the tensile post-yield behavior of ductile steel fibers is regularized to limit mesh-sensitivity using **Equation (4.3)**, where ε_{su} is the regularized ultimate strain capacity of steel, ε_y is the yield strain, L_{gage} is the gage length used in laboratory and G_{py} is the post-yield energy. When modeling thin RC walls, the tensile behavior of wire mesh fibers should not be regularized in any case, as they are expected to fail in tension before the section response of the wall softens, which implies that their simulated strains are not affected by localization issues (Vásquez et al., 2016). The resulting stress-strain relationship is depicted in **Figure 4.3b**.

The shear behavior of the walls is simulated using a linear-elastic constitutive relationship at the section level as expressed in **Equation (4.4)**, where G_{eff} is the effective shear modulus of the section, A_{cv} is the shear area of the section and k_s is the shear form factor, typically taken as 5/6 for rectangular sections. This simplistic approach has been implemented by other authors with accurate predictions of flexure responses of slender RC walls (Gogus, 2010; Kircher et al., 2010; Orakcal & Wallace, 2006; Pugh et al., 2015). Nonetheless, Kolozvari and Wallace (2016) showed that predicted interstory drift ratios and wall shear demands can be significantly affected by the implemented shear model (e.g. the value of G_{eff}). Recommended values of G_{eff} range from $0.1G_c$ to $0.5G_c$ (Gogus, 2010; Pacific Earthquake Engineering Research Center, 2017; Pacific Earthquake Engineering Research Center & Applied Technology Council, 2010; Tran, 2012), where $G_c = 0.4E_c$ is the uncracked shear modulus of concrete. However, this study uses $G_{eff} = 1.0G_c$ because an acceptable level of accuracy was obtained for this value after model calibration using results from tests on isolated thin RC wall specimens. Future research is required to evaluate the shear response of these elements.

$$E_{ts} = \frac{f_t^2}{2G_f} L_E \tag{4.1}$$

$$\varepsilon_{c20} = \frac{G_f^c}{0.6 f_c' L_E} - \frac{0.8 f_c'}{E_c} + \varepsilon_{c0} \tag{4.2}$$

$$\varepsilon_{su} = \varepsilon_y + \frac{2}{\left(f_u + f_y\right)}\left(\frac{G_{py}}{L_E}\right) = \varepsilon_y + \left(\frac{L_{gage}}{L_E}\right)\left(\varepsilon_{su,test} - \varepsilon_y\right) \tag{4.3}$$

$$V = G_{eff} A_{cv} k_s \gamma \tag{4.4}$$

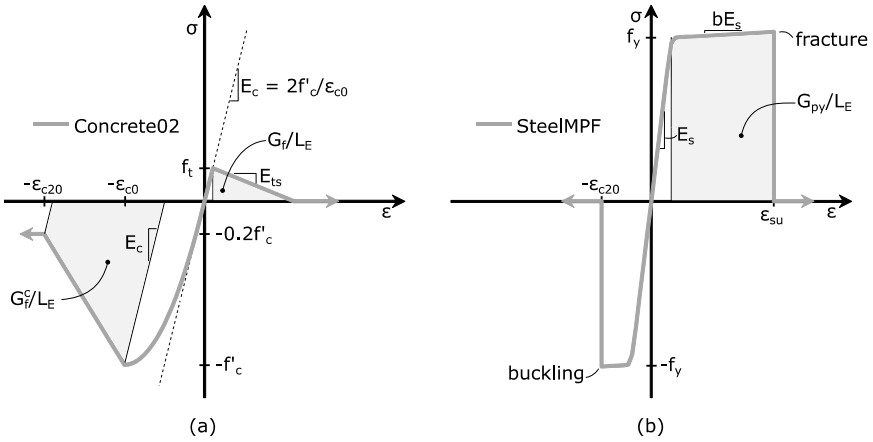

Figure 4.3 – Stress-strain relationships implemented in OpenSees for (a) concrete and (b) reinforcing steel.

4.3 Local deformation demands and simulated plastic hinge length

Coleman and Spacone (2001) showed that the simulated curvature and strain demands in FBC elements are sensitive to the integration scheme used due to localization of the inelastic response in the first integration point (IP). **Figure 4.4a** illustrates the response of an RC column in cantilever simulated using 3, 4 and 5 IPs. The pre-peak global response of the system is consistent among the three implemented integration schemes. Past this point, both the local base section moment-curvature response and the global base shear-displacement response lose objectivity. For the same level of displacement, the curvature demands in the first IP increase with increasing number of IPs. This is because as the number of IPs increases, the length of the first IP decreases and increasing curvatures are required to produce the same displacement. A review of the distribution of curvature demands over the height of the wall reveals that this increase is only significantly evident at the first IP (**Figure 4.4b**). To enforce objectivity in the global response, Coleman and Spacone (2001) proposed the regularization of the stress-strain relationship of the material based on the assumption of a constant fracture energy in compression G_f^c. In this approach, the strain demand ε_{20} at which concrete in compression loses 80% of its peak strength is calibrated to maintain a constant value of G_f^c, as shown in **Equation (4.2)**. While this method effectively results in predictions of the global force-displacement response that are independent of the integration scheme used, local curvature and strain demands in the plastic hinge region still need to be postprocessed to obtain objective section deformation predictions. The only exception is when the simulated plastic hinge length (i.e. length of the first IP) and the targeted plastic hinge length are the same. Thus, the modeling approach implemented herein requires the definition of a plastic hinge length that is consistent with the experimentally-observed behavior of thin RC walls so that the predicted local deformations have physical meaning.

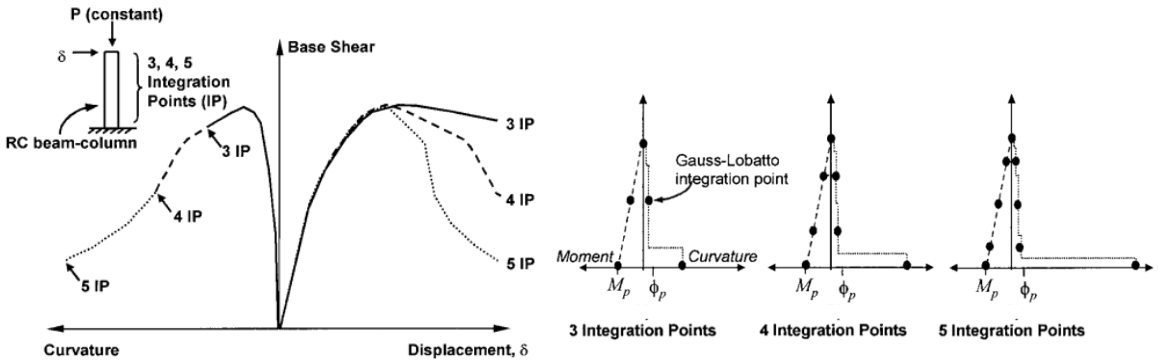

(a) Local and global response **(b) Moment and curvature distribution**

Figure 4.4 – Sensitivity of the nonlinear response of an RC beam column simulated using *forceBeamColum* elements to the number of integration points (Coleman & Spacone, 2001).

The definition of an appropriate plastic hinge length l_p for thin RC walls is a subject of continuous research in the engineering community. This parameter represents an equivalent length over which inelastic deformations are assumed to be concentrated for the prediction of flexural deflections and rotations along the element (Park & Paulay, 1975). It has been found that this parameter depends on many characteristics, such as the dimensions of the cross section of the element, its height, the geometric and mechanical characteristics of the reinforcement, and the level of axial-flexural demands (Mattock, 1965; Paulay & Priestley, 1992; Priestley et al., 1996). ASCE 41 (2017) states that the value of l_p shall be set equal to 0.5 times the flexural depth of the wall but less than one story height for structural walls and less than 50% of the element length for wall segments. However, as discussed in **Section 1.3**, post-earthquake reconnaissance and experimental results from tests on thin RC walls suggest that damage concentrates in a smaller portion of walls failing in flexural-compression, and that l_p may be more related to the wall thickness t_w, with typical values of $2t_w \leq l_p \leq 3t_w$ (Blandón & Bonett, 2019; Segura & Wallace, 2018b; Takahashi et al., 2013; Wallace, 2011; Welt, 2015). Yiqiu Lu et al. (2017) and Blandón et al. (2018) also found that walls with minimal amounts of distributed reinforcement tend to exhibit reduced plastic hinge lengths for large deformation cycles as a result of the concentration of plasticity in a limited number of cracks. All these phenomena make it a complex task to propose a non-linear model for thin walls that is capable of adequately replicating the local damage behavior observed in the laboratory while being both numerically stable and computationally efficient. For the purposes of this research, it will be assumed that the global force-displacement response of the walls can be adequately represented with a plastic hinge length in the range $2t_w \leq l_p \leq 3t_w$. This model feature is calibrated in **Section 4.4** for a set of four wall specimens resembling the Colombian building typology. For the geometry of the case-study walls, the Gauss-Radau and Gauss-Lobatto integration schemes with 3 and 4 IPs result in plastic hinge lengths in the targeted range. The section curvatures obtained with this approach should be interpreted as plausible average values of curvature demand. On the other hand, the simulated distribution of axial vertical strains along the wall may differ significantly from the experimentally-measured data, as explained next.

The model implemented in this research uses FBC elements whose flexural response is simulated assuming that the wall cross-section remains plane, therefore, the

strains along the wall follow a linear relationship. This is a typical assumption in other modeling approaches as well. However, experimentally-measured vertical strain profiles in slender walls are typically non-linear, especially at intermediate and large drift levels (Thomsen & Wallace, 2004). Recent research has shown that modeling approaches that assume plane sections underestimate or overestimate the vertical strains at the wall edge by a factor of 1.5 to 2 (Kolozvari et al., 2018; Parra et al., 2019; Ugalde et al., 2019). **Figure 4.5** depicts an example found in the literature (Parra et al., 2019) of the simulated response of the RW2 specimen from Thomsen and Wallace (2004) using FBC elements. The simulated global force-displacement relationship and lateral displacement profiles are in good agreement with the experimentally-measured results. However, tensile strains within the plastic hinge are overestimated for increasing drift levels, while compressive strains are underestimated. Similar results are reported by Kolozvari et al. (2018) for the same specimen using different modeling approaches to simulate the wall cyclic response.

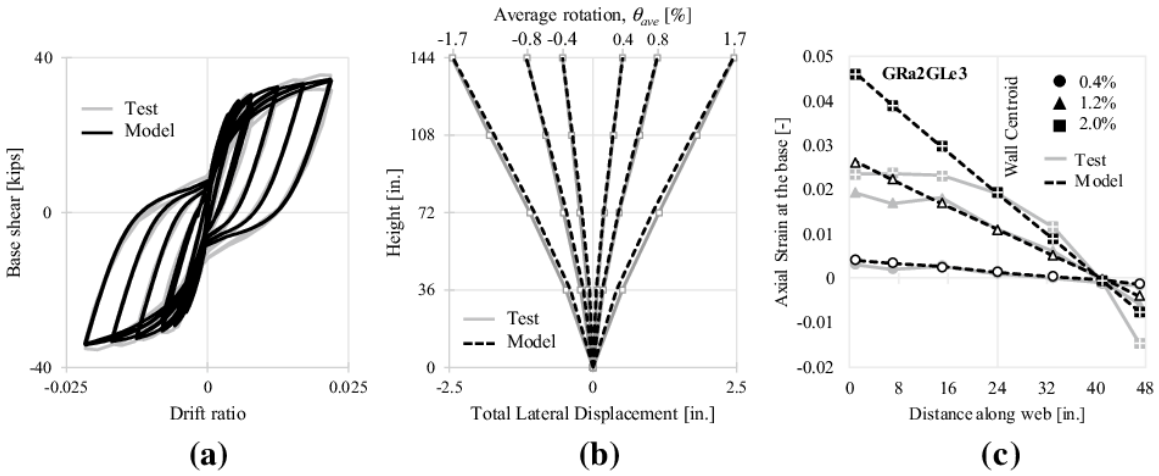

Figure 4.5 – Comparison of model and test data of specimen RW2 (Thomsen & Wallace, 2004) using FBC elements (from Parra et al., 2019): (a) global force-displacement relationship, (b) displacement profile for various levels of average rotation, and (c) axial-strain profile along the web for various levels of average rotation (1 kip = 4.4 kN, 1 in = 25.4 mm).

4.4 Validation of the proposed modeling approach for the Colombian building typology

The proposed model is validated using the experimental data from the four quasi-static cyclic tests in Blandón et al. (2018). All the specimens from this experimental program are T-shaped thin RC wall panels with shear-span ratio M/Vl_w of approximately 2.0, low axial load (P/f'_cA_g < 5%) and low web reinforcement ratios (ρ_w < 0.30%). These specimens were deemed as representative of Colombian construction practices in **Section 1.3**. The main characteristics of the studied walls are presented in **Table 4.1**, while general details on their geometry and reinforcement configuration are depicted in **Figure 4.6**. Further details of the experimental program may be found elsewhere (Blandón et al., 2018). The nonlinear model is evaluated in terms of its capability to simulate the lateral force-top displacement response of the specimens and to predict their ultimate displacement capacity and mode of failure.

Table 4.1 – Characteristics of test specimens used for model validation.

Spec.	f'_c [MPa]	t_w [mm]	Web reinf. ρ_w [%]	Web reinf. d_b [mm]	Type of web reinf.	Additional wall boundary reinf.	Axial load, P [kN] ($/f'_cA_g$ [%])	Shear-span ratio
W4	39.1	100	0.27	6.4	Distributed intermediate ductility bars	None	470 (4.4)	2.08
W5	40.1	100	0.26	7.0	Electro-welded cold-drawn mesh	None	470 (4.3)	2.08
W6	39.2	100	0.27	6.4	Distributed intermediate ductility bars	2 Φ 12.7 mm	470 (4.4)	2.08
W7	47.0	100	0.27	6.4	Distributed intermediate ductility bars	2 Φ 12.7 mm	490 (3.7)	2.08

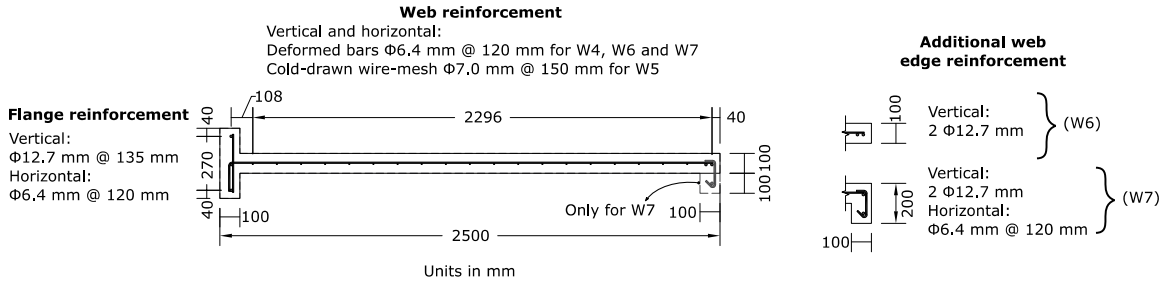

Figure 4.6 – Geometry and reinforcement layout of the specimens W4 to W7 (adapted from Blandón et al., 2018).

One of the failure modes found by Blandón et al. (2018) in their experimental campaign was the rupture of the lap splice reinforcement at the wall-foundation interface. It was found that the inclusion of this additional reinforcement generates an increase in the flexural strength of the base section of the walls and may shift up the critical section. To consider this effect, two types of fiber sections were created. The first section included additional steel fibers to represent the wall-foundation lap splice and was assigned to the first integration point of the *forceBeamColumn* element. This first integration point had a length equal to the lap splice length. The second section corresponds to the typical wall reinforcement from **Figure 4.6** and was assigned to the remaining integration points.

The simulated response using the previously described models is compared against the experimental data in **Figure 4.7**. The strength of the specimens is in general terms well predicted by the model (about ±6% error), except for the specimen W4 in the flange-in-compression loading direction (13% error). The initial stiffness is overestimated by the model in most cases, mainly because microcracking and strain penetration are not accounted for at the wall base (Parra et al., 2019). The same observation does not apply to the effective yield stiffness. **Table 4.2** compares the experimental and simulated response of the specimens in terms of their yield, peak strength and ultimate limits, as well as their mode of failures. The following are main observations on the simulated response of each of the specimens based on the previous measures:

- **Specimen W4:** The numerical model accurately predicts the response of wall in the flange-in-tension (positive) loading direction but does not represent well the

response in the opposite direction. In the positive direction, the strength of the specimen is underestimated by 13% at the peak and the observed mode of failure is not predicted. In the negative direction, the predicted strength is only 3% less than the measured in the laboratory. The yield displacement is underpredicted by 16% due to the overestimated initial stiffness. Ultimate displacement and modes of failure are accurately predicted in this loading direction.

- **Specimen W5:** The yield and peak strength of the wall in both loading directions is simulated with a maximum error of 8% and 6%, respectively. The yield displacement is well predicted in the positive direction but overpredicted in the negative direction by more than 50%. Except for lap splice failures, all the failure modes observed during the test are also reproduced by the numerical model. However, the model predicts the loss of lateral strength at an early level of lateral displacement. The simulated hysteretic loops have more pronounced pinching in every cycle.
- **Specimen W6:** The numerical model predicts the yield and peak strength of the wall in both loading directions with a maximum error of 7% and 2%, respectively. The yield displacement is underpredicted in the positive direction by 30% and overpredicted in the negative direction by 38%. Except for lap splice failures, all the failure modes observed during the test are also reproduced by the numerical model. The model also predicts accurately the lateral displacement associated to the sudden loss of lateral strength. The simulated hysteretic loops approximate well the tested response, with more pinching at zero-loading conditions.
- **Specimen W7:** The predicted yield and peak strength of the wall in both loading directions approximates well the response observed in the laboratory, with a maximum error of 5% and 2%, respectively. The yield displacement is slightly underpredicted in the positive direction (2% error) and overpredicted in the negative direction by 20%. As in the case of Specimen W6, except for lap splice failures, all the failure modes observed during the test are also reproduced by the numerical model. The model also predicts accurately the ultimate displacement and the simulated hysteretic loops are in good agreement with the test results.

The numerical model implemented in this chapter predicts with acceptable accuracy the lateral force–displacement response of thin RC walls. Most failure modes affecting the response are well simulated in two of the four specimens used during the calibration and conservatively simulated in a third one. Future research is necessary to improve the predicted hysteretic loop shapes and initial stiffness. However, for this research, the proposed model can reproduce the structural demands of interest and is suitable for EDP-risk estimation.

Table 4.2 – Comparison of the measured and simulated global response quantities as modeled in OpenSees.

Specimen	Loading direction	Yield Limit		Peak strength	Ultimate	Failure mode	
		$\Delta_{y,sim}/\Delta_{y,test}$	$V_{y,sim}/V_{y,test}$	$V_{max,sim}/V_{max,test}$	$\Delta_{u,sim}/\Delta_{u,test}$	Simulation	Test
W4	(+)	1.04	0.83	0.87	1.44	None	WLR
	(-)	0.84	0.96	0.97	1.04	CC, FRR	CC, FRR
W5	(+)	1.00	1.02	1.06	0.89	WRR	WLR, WRR
	(-)	1.58	1.08	0.97	0.78	WRR, CC, FRR	WLR, CC, FRR
W6	(+)	0.71	0.96	1.02	0.92	WBR	WLR, SWBR
	(-)	1.38	1.07	1.00	0.99	FRR	FRR
W7	(+)	1.04	1.00	1.00	1.09	WBR	WLR, WBR
	(-)	1.20	1.05	0.98	1.02	FRR	WLR, FRR

Symbols:

$\boldsymbol{\Delta_y}$: the yield displacement. $\mathbf{V_y}$: the yield strength. $\mathbf{V_{max}}$: the peak strength. Δ_u: the ultimate displacement.

Abbreviations:

WRR: rupture of the web distributed reinforcement above the wall-foundation interface.
WLR: rupture of web distributed reinforcement located at the wall-foundation interface (lap splice).
CC: concrete crushing.
FRR: rupture of the flange reinforcement above the wall-foundation interface.
WBR: rupture of the additional web boundary reinforcement above the wall-foundation interface.
SWBR: slippage of the additional web boundary reinforcement at the wall-foundation interface (lap splice).

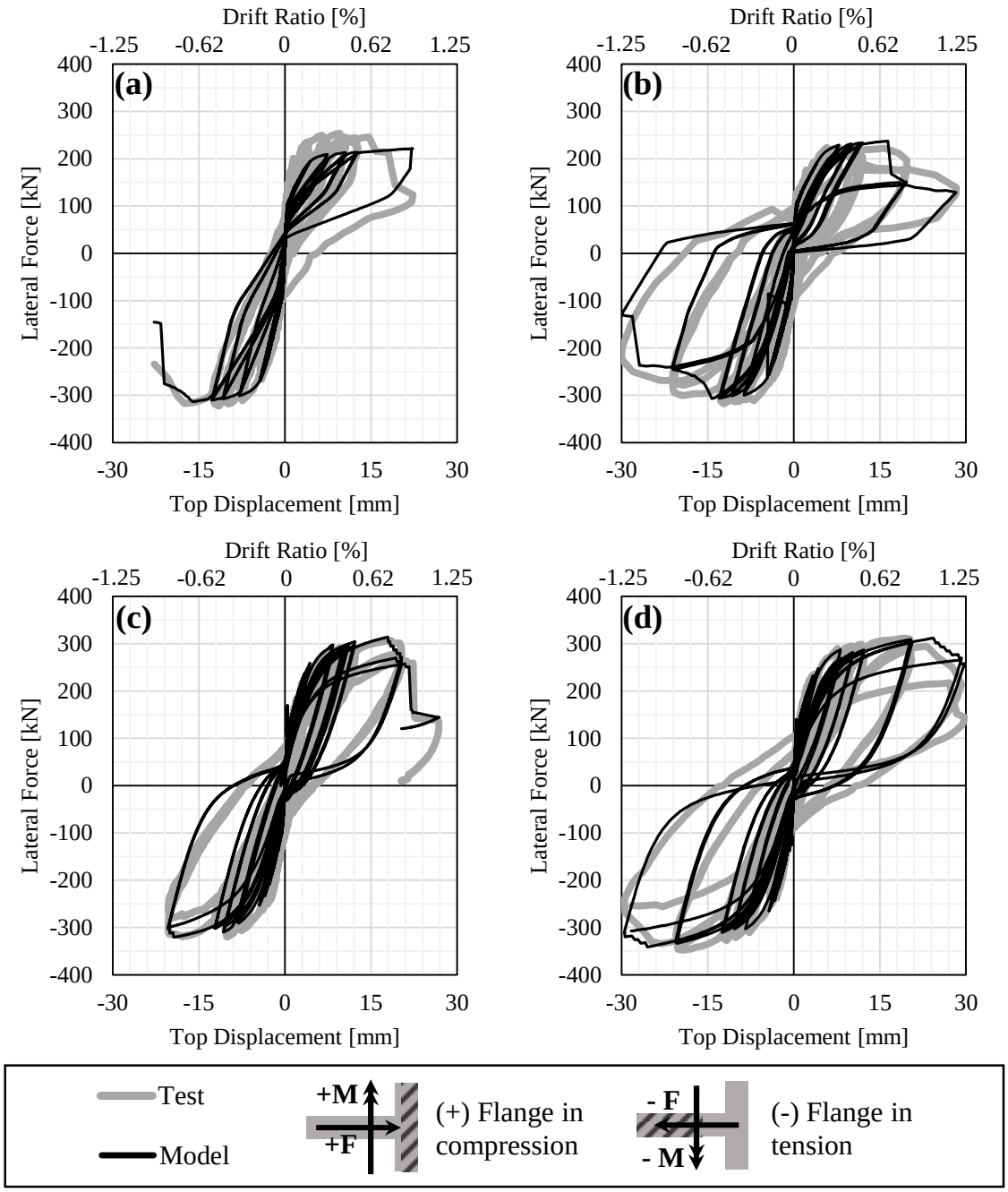

Figure 4.7 – Lateral load-top displacement histories for specimens (a) W4, (b) W5, (c) W6 and (d) W7 as reported in Blandón et al. (2018) and as simulated using the proposed simple approach.

Chapter 5 – Nonlinear Static Response

The nonlinear response of the building archetypes presented in **Chapter 2** is evaluated in this research by means of a nonlinear static (pushover) analysis. The procedure is performed along the longitudinal (EW) direction of the structures following a vertical distribution of the lateral force in proportion to the fundamental mode shape and the numerical strategy described in **Chapter 4**. This analysis is used to quantify the maximum base shear capacity and the ultimate displacement capacity of the building archetypes. The procedure is also useful to identify yielding patterns and establish performance limit states.

5.1 Global base shear – roof displacement response

The pushover response of the building archetypes is presented in **Figure 5.1** in terms of the weight-normalized base shear V_b/W and the roof drift ratio (RDR). Positive values of RDR correspond to displacement in the East direction (see **Figure 2.1** for reference). The onset of material limit states (i.e. the instant when any wall in the structure reaches such limits) is identified with colored markers. In the legend, RB is short for ductile boundary rebars and WM refers to the cold-drawn wires that constitute the web distributed reinforcement of the walls. The structural behavior of the three case-study buildings exhibits a well-defined elastic portion until the onset of concrete cracking, followed by an ascending branch of reduced stiffness until the maximum base shear capacity, $V_{b,max}$ is reached. The value of $V_{b,max}$ is limited by the deformation capacity of the web distributed reinforcement (WM rupture). After this point, there is a sudden loss of lateral strength. **Table 5.1** identifies the roof drift ratio (RDR), first-story drift ratio (1^{st}-SDR) and base shear (V_b/W) associated to the different simulated material limit states. The value of 1^{st}-SDR can easily be related to damage in the walls as explained in **Section 1.3**. A detailed description of the observed structural response of each building with respect to these limit states is given below.

- **5-story building:** the onset of cracking starts in the bottom first-story wall piers at an RDR of 0.02% and a 1^{st}-SDR of 0.01% and continues progressively until an RDR of 0.04% and a 1^{st}-SDR of 0.02%. The initial stiffness and cracking strength of the system are controlled by the wall piers with the largest assigned cross sections (the equivalent to W01 and W04 sections in **Figure 2.5**). These large concrete sections contribute to a cracking strength of similar magnitude to the design base shear (modified by R). After cracking, the building exhibits a reduced lateral stiffness and several progressive yielding mechanisms start activating. The first yielding in tension of the web longitudinal distributed reinforcement occurs in the smallest flange of the W01 pier located in the East face of the building (see **Figure 2.1**) at an RDR of 0.19% and a 1^{st}-SDR of 0.09%. Tensile yielding continues to spread to the rest of the wall piers as the lateral displacement increases. The most extreme fiber in the web edge of the West W04 pier reaches its peak concrete strength at an RDR of 0.38% and a 1^{st}-SDR of 0.16%. The structure exhibits its maximum base shear capacity, $V_{b,max}$ at an RDR of 0.54% and a 1^{st}-SDR of 0.11%, when the tensile strain in the web distributed reinforcement in the East W01 pier reaches the rupture limit. This is immediately followed by concrete

crushing in the West W01 pier. At this point, the lateral strength of the system drops to 40% of its peak value.

- **10-story building:** the onset of cracking starts at an RDR of 0.03% and a 1st-SDR of 0.01% % and continues progressively until an RDR of 0.08% and a 1st-SDR of 0.02%. As in the case of the 5-story building, the initial stiffness and cracking strength of the system are controlled by the East W01 and W04 wall piers. However, in this case the cracking base shear is only 38% of the design base shear. The first yielding in tension occurs in the web boundary reinforcement of the East W04 pier at an RDR of 0.31% and a 1st-SDR of 0.08%. The West W04 pier reaches its peak concrete strength in the web edge at an RDR of 0.81% and a 1st-SDR of 0.20%. The structure exhibits its maximum base shear capacity, $V_{b,max}$ at an RDR of 0.98% and a 1st-SDR of 0.29%, when the tensile strain in the web distributed reinforcement in the East W01 pier reaches the rupture limit. This is immediately followed by concrete crushing in the West W01 pier. At this point, the lateral strength of the system drops to 70% of its peak value.
- **15-story building:** the onset of cracking starts at an RDR of 0.03% and a 1st-SDR of 0.01% % and continues progressively until an RDR of 0.13% and a 1st-SDR of 0.02%. This limit state is reached at an early stage of the analysis, when the corresponding strength is only 30% of the design base shear. The first yielding in tension occurs in the web boundary reinforcement of the East W01 pier at an RDR of 0.46% and a 1st-SDR of 0.07%. At this point the lateral strength coincides with the design base shear. The West W01 pier reaches its peak concrete strength in the web edge at an RDR of 0.96% and a 1st-SDR of 0.15%. The structure exhibits its maximum base shear capacity, $V_{b,max}$ at an RDR of 1.27% and a 1st-SDR of 0.27%, when concrete crushing in the web edge of the West W01 pier occurs and the tensile strain in the web distributed reinforcement in the East W01 pier reaches the rupture limit. At this point, the lateral strength of the system drops to 62% of its peak value.

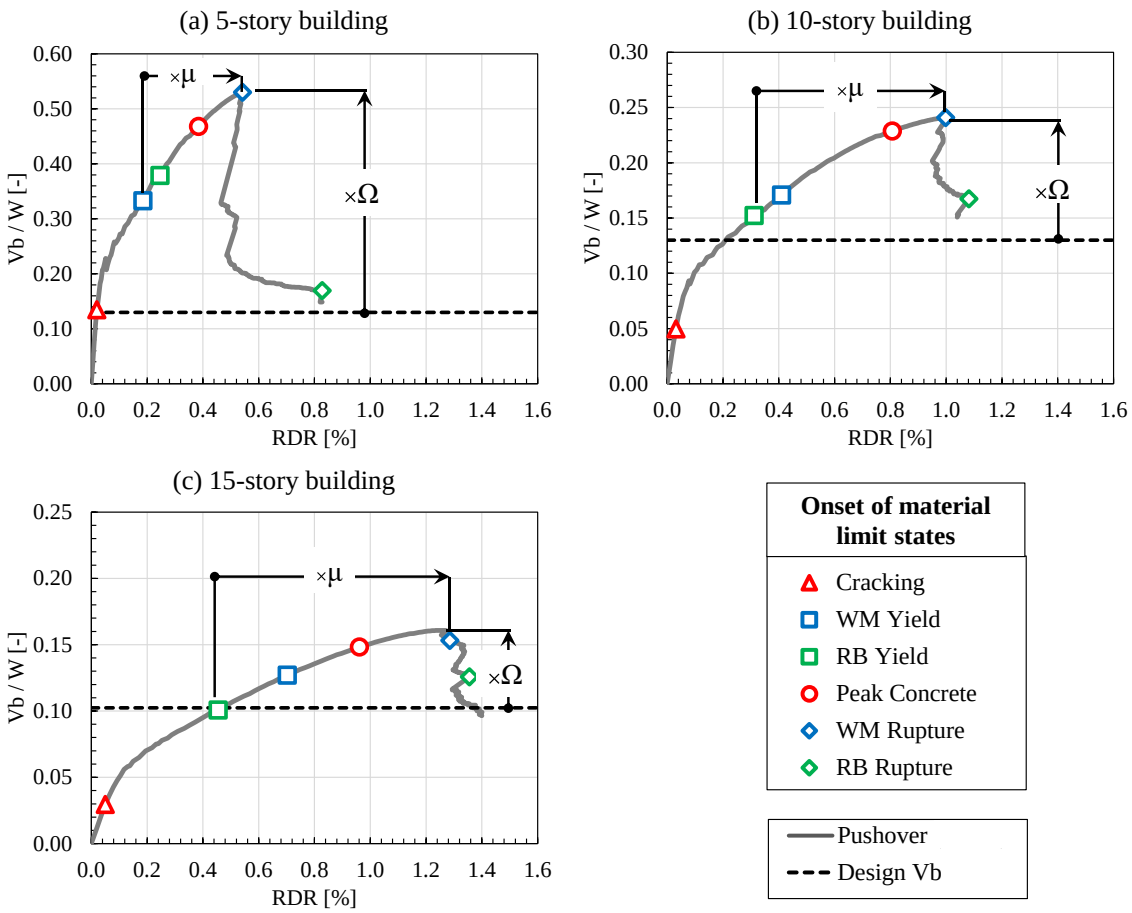

Figure 5.1 – Pushover response of the archetype buildings in terms of the weight-normalized base shear and roof drift ratio (RDR).

Table 5.1 – Onset of material limit states in the pushover response of the building archetypes.

Limit state	5-story building			10-story building			15-story building		
	RDR [%]	1st-SDR [%]	V_b / W [-]	RDR [%]	1st-SDR [%]	V_b / W [-]	RDR [%]	1st-SDR [%]	V_b / W [-]
Onset of cracking	0.02	0.01	0.13	0.03	0.01	0.05	0.05	0.01	0.03
Full cracking	0.04	0.02	0.21	0.08	0.02	0.09	0.13	0.02	0.10
RB yielding	0.25	0.11	0.38	0.31	0.08	0.15	0.46	0.07	0.10
WM yielding	0.19	0.09	0.33	0.41	0.09	0.17	0.70	0.11	0.13
Concrete peak stress	0.38	0.16	0.47	0.81	0.20	0.23	0.96	0.15	0.15
RB rupture	0.83	0.76	0.17	1.08	0.59	0.17	1.36	0.57	0.13
WM rupture	0.54	0.25	0.53	1.00	0.30	0.24	1.29	0.32	0.15
Concrete crushing	0.54	0.39	0.23	1.00	0.37	0.20	1.27	0.27	0.16

The global pushover response of the building archetypes can also be evaluated in terms of the overstrength factor Ω and the ductility capacity μ. This research defines Ω factor is as the ratio of $V_{b,max}$ to the design base shear, $V_{b,design}$ (FEMA P695, 2009). On the other hand, μ is defined as the ratio of the roof displacement at which the system reaches its peak strength, δ_{peak}, to the first yield roof displacement δ_y. A similar definition of μ has been used in past research for a 20-story wall building in Chile (Cando et al., 2020). **Figure 5.1** shows a graphic description of the estimation of Ω and μ from the pushover response.

These parameters describe quantitatively the expected performance of the structures, measuring their force and deformation capacity beyond that required by code specifications. **Table 5.2** shows the quantified values for Ω and μ. The 5-story building has the largest overstrength (Ω = 4.08), while the 15-story building has the smallest value (Ω = 1.57). This is because the flexural design demands on the 5-story building are very low compared to the large wall sections and the provided minimum web reinforcement is more than sufficient to meet the design requirements. Another contributor to the overstrength of the 5-story buildings is that expected yield strength of the cold-drawn wires is approximately 1.30 times the nominal strength. In the case of 10 and 15 story buildings, the flexural design demands are higher, as demonstrated by the need to include ductile reinforcing steel at the wall boundaries. Decreasing values of Ω with increasing number of stories were also observed by Ugalde and Lopez-Garcia (2017) and Ugalde et al. (2019) in three buildings with 5, 17 and 26 stories for wall buildings simulated using rigid-diaphragm constraints.

Concerning the displacement capacity beyond the elastic range, the results of the pushover analysis showed that the 5-story building is the most susceptible to experience damage at low levels of roof displacement, reaching its maximum capacity at an RDR = 0.54%. In contrast, the maximum allowable story drift ratio in Colombia is 1.43%. The results suggest that increasing the number of stories also increases the roof displacement capacity of the buildings, reaching RDR capacity limits equal to 0.98% and 1.27% for 10- and 15-story buildings. This apparent increased roof displacement capacity is due to a significant contribution of elastic displacements above the plastic hinge, as will be discussed in **Section 5.3**. This behavior disagrees with the plastic hinge model presented in **Figure 1.4**, which assumes that the roof displacement demand is the result of rigid body rotation from the wall base. The larger roof displacement capacity with increasing height does to necessarily implies improved performance, as taller buildings are also more flexible and more likely to experience large deformations when subjected to high intensity ground motions (compare the higher drift levels predicted for the design earthquake during the elastic analysis of the three buildings presented in **Figure 2.3**). An objective way to evaluate the displacement capacity with respect to the flexibility of the structure is based on the ductility capacity μ. **Table 5.2** shows that the value of μ for the three buildings is in the same order of magnitude. The 10-story building has the highest value of μ among the three case studies (μ = 3.15), while the 15-story building has the lowest value (μ = 2.78). Reported μ values for a 20-story wall building in Santiago (Chile) using a similar definition of ductility ranged between 4.3 and 5.8 (Cando et al., 2020). For the case of the Colombian building typology, values of μ between 2.1 and 6.0 when applying this definition of μ to the four walls tested by Blandón et al. (2018).

Table 5.2 – Seismic performance factors of the case-study buildings from pushover analysis.

Building	$V_{b,design}$ / W [-]	$V_{b,max}$ / W [-]	δ_y / h_w [%]	δ_{peak} / h_w [%]	Ω [-]	μ [-]
5-story	0.13	0.53	0.19	0.54	4.08	2.93
10-story	0.13	0.24	0.31	0.98	1.85	3.15
15-story	0.10	0.16	0.46	1.27	1.57	2.78

The pushover curves presented in this study were obtained from models that assumed that the lateral strength of the buildings is the result of only the action of the

structural walls and that the effect of the floor slabs can be modeled with a rigid diaphragm constraint. However, recent research on two wall buildings in Chile suggests that explicitly modeling the behavior of the slabs can significantly increase the resistance predicted in the pushover analysis and reduce the system displacement capacity to a lesser extent (Ugalde et al., 2019). Further research is required for the Colombian building typology.

5.2 Distribution of the global and local demands in the wall piers

Static equilibrium dictates that the total base shear exhibited by the case-study buildings must be the result of the addition of the individual base shears resisted by the wall piers that conform the lateral load-resisting system. The amount of force that each wall pier takes depends on its flexural strength and its stiffness. **Figure 5.2** shows the relative contribution of each wall pier to the total base shear in the pushover analysis for each of the building archetypes. Each series in the plots represents a wall pier (or two, if indicated by a "x2") in either the West or East side of the buildings. Increasing values of roof drift ratio (RDR) represent lateral displacement toward the East direction. When pushed in this direction, the West W01 pier exhibits tensile strains in its largest flange and compression in the smallest one, while its counterpart in the East side exhibits the opposite behavior. Similar observations can be made for the remaining wall piers. The results from **Figure 5.2** indicate that the major contributors to the strength of the system in all the buildings are the West W01 and W04 piers. This is expected due to the large dimensions these elements have and their concentrated amount of reinforcement in the flanges. At an early stage of the analysis, the relative contribution from the West W01 pier exhibits a drop due to the onset of cracking. At this point, the stiffness of the wall starts degrading and the base shear redistributes in the remaining stiffer walls. Eventually, these elements reach its cracking limit and the West W01 pier regains its role as the major contributor to the strength of the system. The West W01 pier starts exhibiting a drop in its relative contribution at levels of RDR close to peak strength of the buildings. This triggers an increase in the contribution of the remaining elements, especially the East W05 piers. This explains the sudden loss of lateral strength observed in the pushover of the building archetypes, as the contribution of the remaining other wall piers is limited by their much lower flexural capacity. The complicated interaction among wall piers makes it difficult to use simplified methods to estimate the capacity of the whole structure for different levels of displacement.

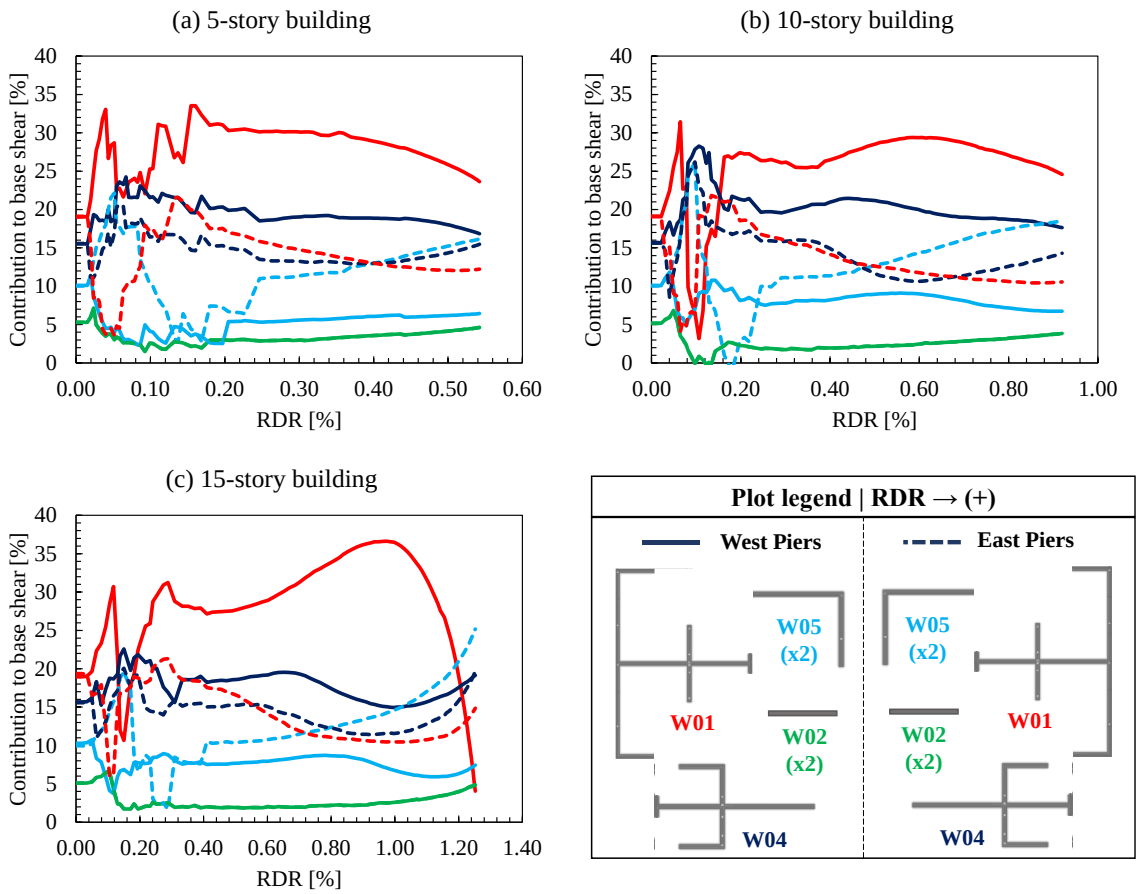

Figure 5.2 – Relative contribution of each wall pier base shear to the global base shear for increasing levels of roof drift ratio (RDR) until maximum strength is reached in the pushover analysis.

As in the case of the base shear, local section deformation demands are not distributed uniformly among the wall piers. **Figure 5.3** presents the strain demands recorded in the wall boundaries of the bottom first-story section of each wall pier with respect to the observed RDR for the three case-study buildings. As in the case of **Figure 5.2**, each series in the plots represents a wall pier (or two, if indicated by a "x2") in either the West or East side of the buildings. The recorded strain demands are consistent with a plastic hinge length in the range $2t_w \leq l_p \leq 3t_w$ and assume linear distribution of strains along the wall length. The implications of these assumptions were discussed in **Section 4.3**. Note that concrete compressive strain values $\varepsilon_{cu} > 0.6\%$ in unconfined boundary elements (as in the case of the 5- and 10-story buildings) are only to be interpreted as numerical results as concrete is expected to have already crushed at such deformation values. **Figure 5.3** indicates that there is a sudden increase in both the compressive and tensile strain demands as the buildings reach the RDR associated to their maximum lateral strength. As previously indicated in **Figure 5.1**, the onset of yielding and concrete crushing starts in the W01 and W04 piers, as their large wall lengths and flange widths ($l_w > 5.0$ m) along with the provided amount of flange reinforcement requires the wall web edge or the smallest flange to exhibit large deformations in order to ensure section equilibrium. In general, the strain demands are directly influenced by the area available in the section to work in compression and the unbalanced amount of boundary reinforcement. That is why

the East W01 pier exhibits lower strain demands, as this pier is being loaded in the flange-in-compression loading direction in the pushover analysis. Rectangular and shorter flanged-walls like the W02 and W05 piers have more moderate strain demands, experiencing a gradual increase in the observed strains as the system begins to lose lateral strength.

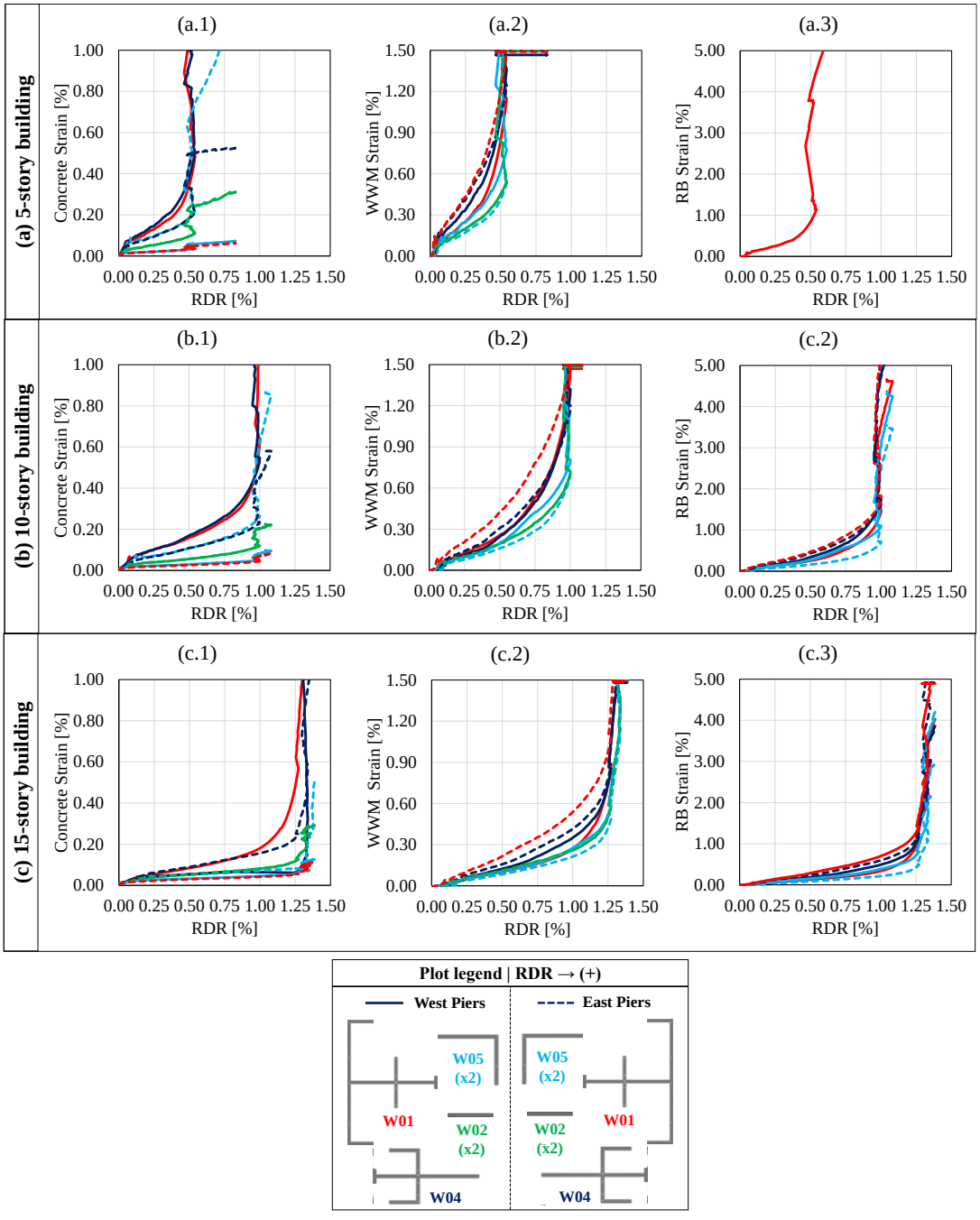

Figure 5.3 – Local strain demands in (1) the concrete wall boundary in compression, (2) the distributed web reinforcement in tension and (3) the additional ductile boundary reinforcement in tension (if any) of each wall pier for increasing levels of roof drift ratio (RDR) and number of stories.

5.3 Damage concentration in the first-story

This research has used the roof drift ratio (RDR) as the main response parameter to establish performance limits for the case-study buildings. This is in line with the traditional way in which the response of RC structures is analyzed (FEMA P695, 2009). However, recent research has suggested that the roof drift and the upper-story drifts are not the best indicators of damage in RC wall buildings. Ugalde et al. (2019) suggested the use of the tangential drift as an alternative indicator of the distribution of flexural demands and damage in RC wall buildings. In the presence of a rigid foundation (disregarding effects of soil-structure interaction), tangential drift coincides with story drift at the first story. In the upper stories, the tangential drift can be significantly less because a portion of the relative lateral story displacement is due to the rotation of the adjacent lower floor, as shown in **Figure 5.4**. The pushover analyses presented in this chapter showed that the deformation demands at the first story were high enough to limit the roof drift capacity of the system. The level of damage concentration in the first story with respect to the remaining upper ones is directly related to the contribution of the first-story displacement δ_1 and second-floor rotation θ_2 to the total roof displacement δ_{roof} (**Figure 5.4**). Assuming rigid body rotation of the upper stories, this contribution can be computed using **Equation (5.1)**, where δ_{rigid} is the rigid-body displacement resulting from the deformation of the first story, h_w is the total wall height and h_1 is the first-story height.

$$\delta_{rigid} = \delta_1 + \theta_2(h_w - h_1) \tag{5.1}$$

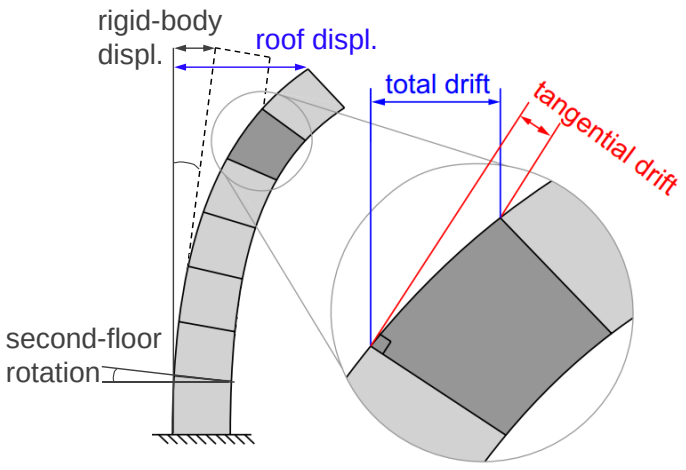

Figure 5.4 – Definition of total story drift, tangential story drift and rigid body displacement (adapted from Ugalde et al., 2019).

Figure 5.5 presents the obtained relative contribution of the first-story deformation to the total roof displacement, $\delta_{rigid}/\delta_{roof}$, for increasing levels of roof drift ratio (RDR) in the three building archetypes. Colored markers indicate the onset of material limit states and are included in the figure for reference. Increasing relative contributions are associated to damage concentration in the first story. The results indicate that the 5-story building exhibits the largest relative contributions from the first story, with 64% of the roof displacement being the result of rigid body rotation at the moment in which the peak strength of the system is reached (at the onset of web reinforcement rupture) and exhibits a sudden increase to 95% after the system loses its lateral strength capacity. As the number

of stories increases, the relative contribution of the first story to the roof displacement decreases. About 45% of the roof displacement in the 10-story building is the result of rigid body rotation from the first story when the peak strength of the system and increases to 70% after the system loses its lateral strength. In the 15-story building, these contributions are 35% and 65%. The contribution of the rigid-body rotation decreases with the number of stories due to the elastic displacement of the walls above the plastic hinge. In other words, the increased height of the building introduces extra flexibility in the system. In consequence, the relative contributions exhibited by buildings with different number of stories cannot be directly compared. However, these results allow the structural engineer to have a general overview of the evolution of damage concentration patterns in the buildings. For example, the relative contribution of the first-story rotation to the roof displacement exhibits a first significant increase after the onset of cracking in each of the case-study buildings due to the reduction of the first-story stiffness. As progressive yielding starts the contribution remains in the same order of magnitude until the concrete fibers in compression reach their peak strength. Past this point, the relative contributions start increasing again until the first steel web reinforcement fiber reaches the rupture limit. After this limit is reached, the system experiences a sudden increase in the relative contribution of the first-story deformation to the total roof displacement, indicating that most of the damage in the building is localized at the base of the structure.

Figure 5.5 shows that a large percentage of the roof displacement response obtained in the pushover analysis results from the concentration of damage at the first story. With this in mind, **Figure 5.6** presents again the global pushover response that was initially presented in **Figure 5.1**, but this time the first-story drift ratio (1^{st}-SDR) is used instead of the roof drift ratio (RDR) as the displacement response parameter. Again, the onsets of material limit states are included in the figure with colored markers, as well as the design base shear. The values of 1^{st}-SDR associated to these limit states are presented in **Table 5.1**. The first-story response of the systems before the peak strength is reached is consistent among the three archetype buildings, with little variations in the levels of 1^{st}-SDR associated to the cracking, yielding and peak-strength limit states. The onset of yielding occurs at levels of 1^{st}-SDR between 0.07% and 0.09%. The 1^{st}-SDR at which the system reaches its peak strength is in the range of 0.25% to 0.29%. The first-story pushover response of the 5-story building exhibits a sudden loss of strength for increasing values of 1^{st}-SDR after reaching its peak strength. This is expected because the wall piers in this building do not have ductile boundary reinforcement (except for the W01 piers at their largest flange). Once rupture of the cold-drawn WWM occurs, there is no other source of ductile response in the system and the building loses its lateral strength. On the other hand, the 10-story and 15-story buildings exhibit a moderately ductile first-story response after they reach their peak lateral strength. This is due to the wall piers in these buildings having ductile boundary reinforcement. The system is able to maintain is lateral strength until the onset of rupture of the ductile rebars.

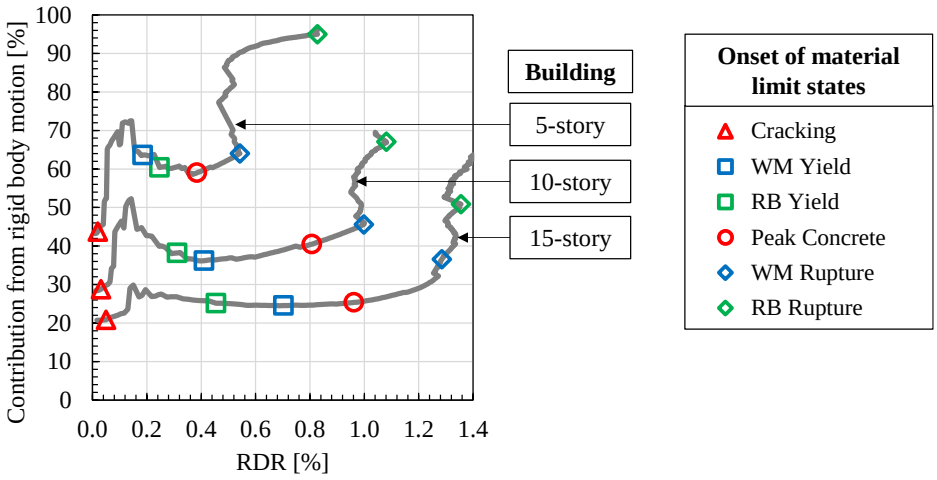

Figure 5.5 – Relative contribution of the first-story displacement (rigid body rotation of the upper stories) to the total roof displacement for different levels of roof drift ratio (RDR)

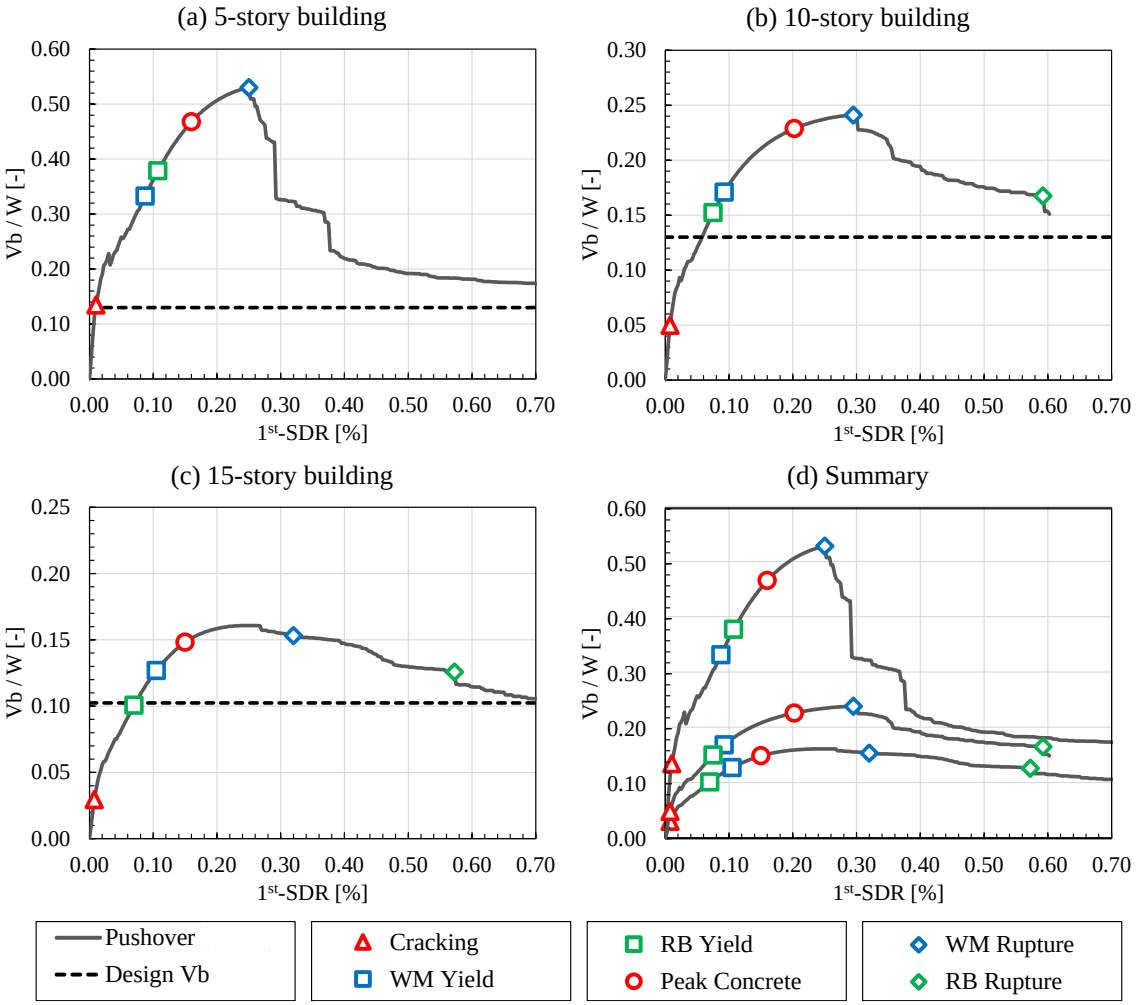

Figure 5.6 – Pushover response of the archetype buildings in terms of the weight-normalized base shear and first-story drift ratio (1st-SDR).

5.4 Main remarks

The results of the pushover analysis confirm that the lateral strength of thin RC wall building systems is commanded by the walls with the largest cross-sections and significant concentration of steel reinforcement in the boundaries. Large flanged wall sections can contribute up to 35% of the flexural capacity of the entire system when loaded in the flange-in-tension loading direction. The design of these elements requires special attention as their large dimensions could promote large tensile strain demands that could lead to rupture of the reinforcement in the case of limited-ductility cold-drawn wire meshes or compressive demands that result in concrete crushing. These modes of failure are brittle in nature and limit the displacement capacity of the system to RDR values in the range of 0.50% to 1.40%. The observed damage concentrates in the bottom first story while the upper portions of the building remain essentially elastic. It was found that the 1^{st}-SDR is better related to damage concentration patterns than the RDR, and that 1^{st}-SDR values at the instant of peak strength remains in the range of 0.25% to 0.30% in the three case studies analyzed.

Chapter 6 – Dynamic Response Assessment

This chapter presents the results of an analytical investigation of the seismic response of thin wall buildings. For each of the building archetypes presented in **Chapter 2**, a series of different nonlinear response history analyses (RHAs) is performed to estimate their expected structural demands under different hazard levels. The set of ground motions used to perform these analyses corresponds to the CSS from **Chapter 3**. The results of these analyses allow establishing probabilistic relations between the ground motion intensity and the structural demand, as well as quantifying their associated risk of exceedance.

6.1 Numerical strategy for the response history analyses

The nonlinear dynamic response of the building archetypes is simulated using the numerical modeling assumptions presented in **Chapter 4**. This model is a 2D simplification of the case-study lateral load-resisting systems in OpenSees in the longitudinal direction. The models are subjected independently to each of the horizontal components of ground motion records that constitute the CSS. This results in a total of 696 RHAs per building. As in the linear analysis from **Section 2.2b**, the building mass is assumed to be lumped at every story level in a central retained node to which each wall is constrained. As the numerical model accounts for only 50% of the stiffness of the buildings (i.e. only the 12 central wall piers are included), the assigned building mass is also 50% of the corresponding seismic weight. Mass- and stiffness-proportional Rayleigh damping is included to simulate the energy dissipation characteristics of the building not represented by the nonlinear behavior of the *forceBeamColumn* elements. The coefficients in the Rayleigh damping formulation were established to achieve damping ratio of $\zeta = 2.5\%$ at periods corresponding to the first and third vibrational modes. Finally, the average-constant-acceleration Newmark method is used to solve the nonlinear equations of motion.

6.2 Dynamic response of the building archetypes under UHS-targeted ground motions

Dynamic structural analyses are often used by structural engineers to predict the response of a structure subjected to ground motions selected to match a specified target response spectrum. Different target spectrums are proposed in the literature, being the UHS at a given hazard level the most commonly used. The structural responses obtained with this approach give an insight on the expected seismic performance of the structure subjected to ground motions associated to a specific hazard level. The current coded-based ground motion selection procedures specified in the NSR-10 are inspired in this approach. Given the extensive use of this methodology in the engineering community, this section initially evaluates the seismic response of the building subjected to ground motions selected to match the UHS for three different hazard levels.

Figure 6.1 shows three sets of ground motions whose mean spectrum approximates the UHS resulting from the hazard contributed by all the seismic sources at the site for three different return periods: 475, 975 and 2,475 years. The elastic NSR-10 design

spectrum is included for reference, as well as the first-mode period of the building archetypes. Note that the spectral shape of the target UHS and the design spectrum do not match for TR = 475 years. This is expected for two reasons: (i) the code-based design spectrum does not have a natural shape consistent with the UHS, (ii) the hazard analysis from which the code-based spectrum is developed is not consistent with the latest available PSHA studies in Colombia. Nevertheless, note that PGA values at TR = 475 years are consistent between both spectra. The ground motions are selected from the CSS set assembled in **Chapter 3**. The CSS set is hazard-consistent with the case-study site conditions in the city of Armenia, Colombia. It is organized in 10 hazard levels of increasing intensity and 3 different tectonic mechanisms, representing the expected seismic demand at the site from a range of return period of 100 to 20,000 years (see **Appendix B**). The sets in **Figure 6.1** are the result of the combination of different hazard levels from each tectonic mechanism as shown in **Table 6.1.** For instance, the 475-year set uses records from the Hazard Level #5 of each type of tectonic mechanism. Note that the selection of these subsets is purely based on spectral matching with the UHS and their assigned rates of occurrence are not necessarily consistent with the hazard; i.e. the structural responses resulting from these subsets do not have the same return period than the UHS they are targeting, but this is a feature of the practice for intensity-based seismic response structural assessment. The number of selected ground motions for each tectonic setting was tried to be approximately the same in each hazard level. This decision is made based on the results from the hazard curves in **Figure 3.6**, that show that, except for structural periods $T < 0.5$ s and return periods $T_R < 475$ years, the contributions from each tectonic setting to the hazard are similar. This selection criterion is not met only for the 475-year UHS, where more crustal ground motions were selected to better fit the target spectrum.

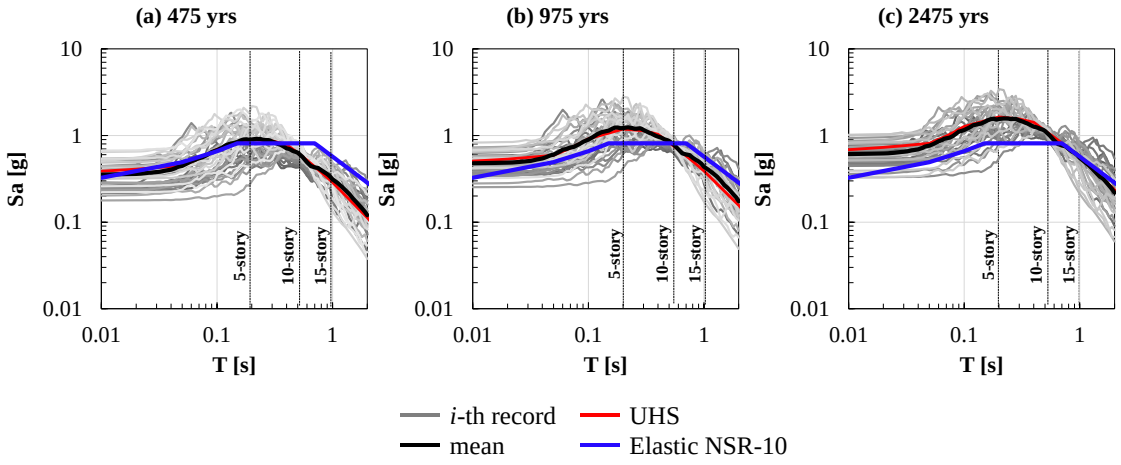

Figure 6.1 – Individual record spectra (ζ = 5%) of three different subsets from the CSS whose mean matches the UHS at specific hazard levels. The elastic NSR-10 design spectrum is included for reference.

Table 6.1 – Selected ground motion subsets matching the UHS corresponding to specific return periods.

Return Period [years]	Crustal			Interface			Intraslab			Total NGM
	Hazard Level ID	Hazard	NGM	Hazard Level ID	Hazard	NGM	Hazard Level ID	Hazard	NGM	
475	5	1.0×10^{-3}	16	5	1.0×10^{-3}	9	5	1.0×10^{-3}	13	38
975	6	4.0×10^{-4}	14	6	4.0×10^{-4}	11	6	4.0×10^{-4}	12	37
2,475	7	1.0×10^{-4}	9	7	1.0×10^{-4}	9	7	1.0×10^{-4}	13	31

NGM: number of two-component ground motion records.

6.2.1 Displacement demands

Figure 6.2 compares the maximum roof drift ratio (RDR) and first-story drift ratio (1^{st}-SDR) demands of the building archetypes subjected to the ground motions from **Figure 6.1**. Because the model is 2D, the number of analyses runs doubles the number of records presented in **Table 6.1**. In **Figure 6.2**, each dynamic analysis run is represented with a circle marker. The median and 84^{th}-percentile (p84) responses are summarized in **Table 6.2**. As expected, the lateral displacement demands increase with increasing ground motion intensity. The median and p84 values of RDR also increases with the number of stories, though large variability in the response is observed. On the other hand, the median and p84 values of 1^{st}-SDR are in the same order of magnitude for all the case-study buildings subjected to the 475-year and 975-year UHS, though there is a trend for larger demands in the 5-story building. Higher-intensity motions (2,475-year UHS) seem to impose larger 1^{st}-SDR demands with decreasing number of stories, being the 5-story building effectively the most demanded. Larger demands in low-rise buildings were expected as the NSR-10 design spectral ordinates for $T > 0.5$ s have return periods larger than 475 years (see **Figure 6.1**). A short-detailed description of the response in relation with the selected hazard levels is provided below.

- **475-year UHS**: Median RDR demands are in the range of 0.25% to 0.43%, being the 15-story building the one experiencing the largest RDR responses. However, 1^{st}-SDR demands are in the same order of magnitude for each building (about 0.10%). 68% of the analysis runs generate RDR and 1^{st}-SDR demands that exceed the onset of yielding identified in **Table 5.1** for the 5-story building. Similar results are observed in the 10-story (71%) and 15-story buildings (68%). None of the ground motions exceed the displacement limit associated to the peak pushover strength of the 5-story building, while 4% and 1% exceed this limit for the 10- and 15-story buildings, respectively.
- **975-year UHS**: Median RDR and 1^{st}-SDR demands are in the ranges of 0.40% to 0.60% and 0.13% to 0.17%, respectively. 92% of the analysis runs generate RDR and 1^{st}-SDR demands that exceed the onset of yielding for the 5-story building. Similar results are observed in the 10-story (96%) and 15-story buildings (92%). The values of RDR and 1^{st}-SDR associated to the peak pushover strength are exceeded in 10% of the analyses for each of the buildings.
- **2,475-year UHS**: Median RDR and 1^{st}-SDR demands are in the ranges of 0.54% to 0.76% and 0.16% to 0.26%, respectively. 95% of the analysis runs generate RDR and 1^{st}-SDR demands that exceed the onset of yielding for the 5-story building. Similar results are observed in the 10-story (97%) and 15-story buildings (95%). The values of RDR and 1^{st}-SDR associated to the peak pushover strength are

exceeded in 50% of the analyses for the 5-story building, and in 34% and 22% for the 10- and 15-story buildings.

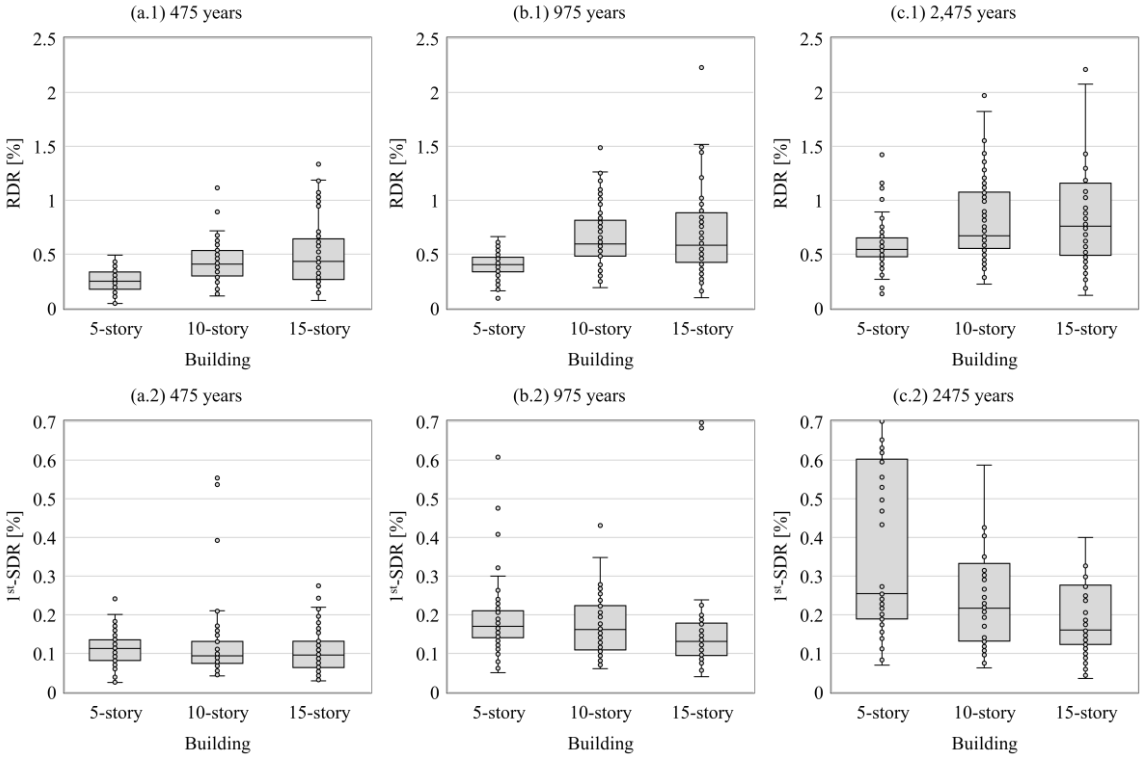

Figure 6.2 – (1) Roof drift ratio (RDR) and (2) first-story drift ratio (1st-SDR) demands exhibited by the building archetypes subjected to ground motions matching the (a) 475-, (b) 975- and (c) 2,475-year return period UHS.

Table 6.2 – Main statistics of the expected roof drift ratio (RDR) and first-story drift ratio (1st-SDR) demands in the building archetypes subjected to ground motions matching the UHS at different hazard levels.

Response		475-year UHS			975-year UHS			2,475-year UHS		
		5-story	10-story	15-story	5-story	10-story	15-story	5-story	10-story	15-story
RDR	Median	0.25	0.41	0.43	0.40	0.60	0.58	0.54	0.68	0.76
[%]	p84	0.38	0.59	0.71	0.52	0.90	0.98	0.75	1.18	1.43
1st-SDR	Median	0.11	0.09	0.09	0.17	0.16	0.13	0.26	0.22	0.16
[%]	p84	0.16	0.15	0.14	0.22	0.26	0.19	0.67	0.49	0.33

Figure 6.3 shows the distribution of the lateral displacement demands in the building archetypes subjected to the selected hazard levels in terms of the story drift ratio (SDR) and the tangent drift ratio (TDR). SDR demands from **Figure 2.3** computed using cracked properties and the NSR-10 design spectrum are also included for reference. Here, the value of TDR is calculated as illustrated in **Figure 5.4**. Median SDR demands imposed by the 475- to 2,475-year ground motions in each of the buildings remain below the 1.43% drift limit required by the NSR-10. The SDR demands above the first story predicted by the linear model are exceeded in more than 50% of the cases for the 475-year UHS in the 5-story building, even though the spectral ordinates from the NSR-10 and the 475-year UHS are in the same order of magnitude around the fundamental period of the structure. For the case of the 10-story building, the median SDR distribution over height is in good

agreement with the SDR demands from the linear model when subjected to the 975-year UHS. A similar behavior is observed in the 15-story buildings for demands consistent with the 975- and 2,475-year UHS. The largest SDR is located at the roof level in each of the structures. This is in contrast with the results from the linear model, which estimated maximum SDR demands in the middle-third stories. However, as previously noted in **Section 5.3**, the SDR is not a good indicator of damage in RC walls, as a portion of it is contributed by the lower stories. It must be accounted, although, when assessing potential damage in non-structural components. A better indicator of damage in the walls is the TDR, which is the direct result of the flexural demands at the specific story. Because soil-structure interaction is not modeled, the TDR and SDR coincide at the first story. The distribution of TDR shows that the first story exhibits the largest deformation demands. The concentration of damage is more evident as the intensity of the ground motion increases (e.g. compare the response for 475- and 2,475-year return periods).

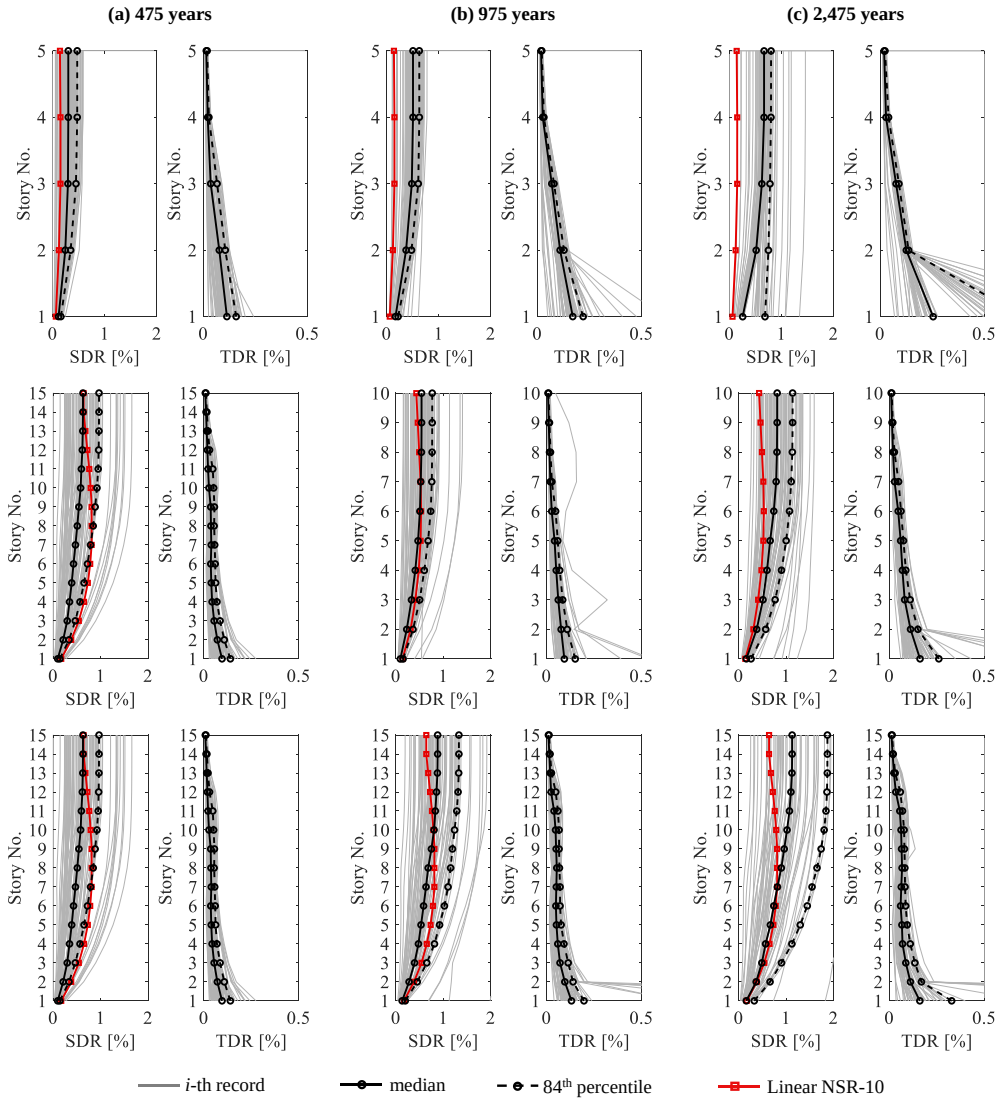

Figure 6.3 – Maximum story drift ratio (SDR) and tangent story drift ratio (TDR) demands exhibited by the building archetypes subjected to ground motions matching the (a) 475-, (b) 975- and (c) 2,475-year return

period UHS. Elastic demands from a linear analysis using the NSR-10 response spectrum are shown for comparison.

The results of the above analyses suggest that low-rise buildings may exhibit greater inelastic demands than high-rise and flexible buildings subject to UHS-compatible seismic demands. This initially appears to contrast with the pushover results, which suggested that the over-strength of the 5-story building was much greater than that of the 10- and 15-story buildings and that its ductility factor was not dramatically different. To get a better idea of the reasons for this behavior, the pushover curves in **Figure 5.1** were converted to an equivalent single-degree-of-freedom (SDOF) system with spectral coordinates (S_d, S_a) using **Equations (6.1)** and **(6.2)**, where V is the pushover strength, M_1 is the first-mode mass, u_{roof} is the roof displacement, Γ_1 is the first-mode participation factor and $\phi_{1,roof}$ is the first-mode ordinate at the roof level. The curves obtained are contrasted with the elastic spectra corresponding to the three hazard levels evaluated in this study, and the point of intersection is designated as the performance point. This performance point is not exactly the level of displacement demand that the structure will experience, as the demand damping is not modified, but it gives an idea of how likely it is that inelastic incursions are expected. The obtained SDOF pushover curves are compared with the elastic response spectra (ζ = 5%) at different hazard levels and the NSR-10 elastic design spectrum in **Figure 6.4**. The results show that the performance point of the 5-story building for any of the selected hazard levels is always associated to displacement demands that are closer or surpass the peak pushover strength of the system. On the other hand, the performance points of the 10- and 15-story buildings approach the peak strength of the system for seismic demands consistent with the 975- and 2,475-year UHS, respectively. The observed SDOF responses also suggest that significant inelastic demands are expected in the 10- and 15-story buildings when subjected to ground motion intensities consistent with the NSR-10 design spectrum, which are considered extremely rare, as the hazard-analysis results showed. These results agree with the performance observed in the nonlinear RHAs from **Figure 6.2**.

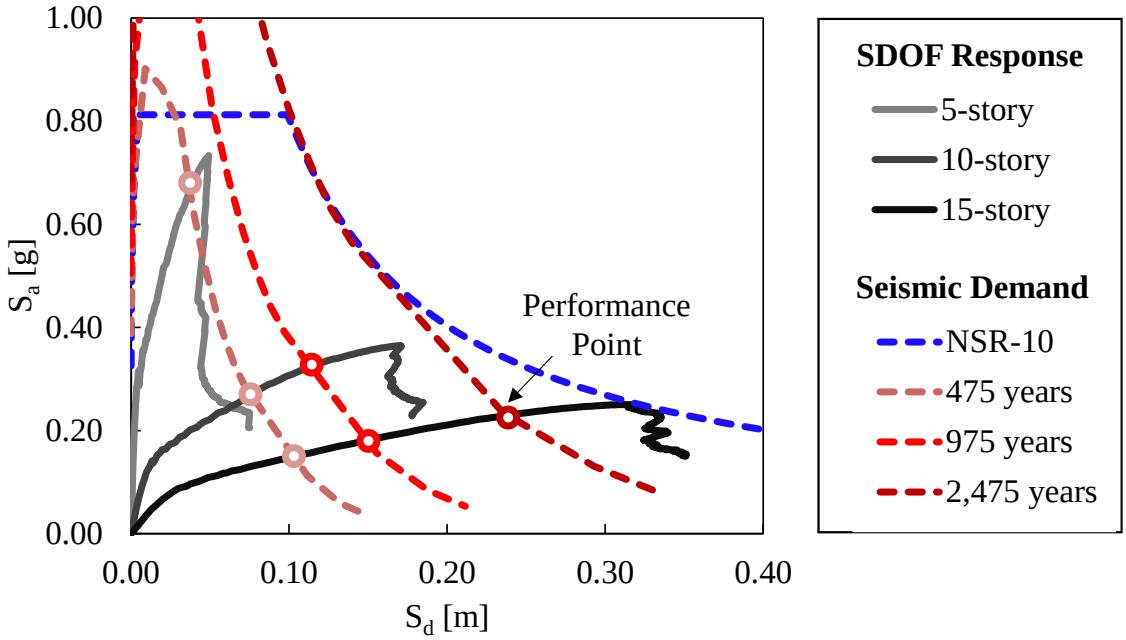

Figure 6.4 – Equivalent SDOF response of the building archetypes compared with the elastic response spectra (ζ = 5%) at different hazard levels and the NSR-10 spectrum.

$$S_a = \frac{V}{M_1} \tag{6.1}$$

$$S_d = \frac{u_{roof}}{\Gamma_1 \phi_{1,roof}} \tag{6.2}$$

6.2.2 Strain demands

Figure 6.5 compares the maximum concrete compressive strains and the maximum tensile strains in the wire-mesh distributed (WM) and ductile boundary reinforcement (RB) of the W01 piers of the building archetypes subjected to the ground motions from **Figure 6.1**. These wall piers are of special interest because their large flanged-section dimensions induce large strain demands in the smallest wall boundary and were identified as the most demanded along with the W04 piers in **Section 5.2**. As explained in **Section 4.3**, the simulated strains are consistent with a plastic hinge length in the range $2t_w \leq l_p \leq 3t_w$ and are assumed to be linearly distributed along the wall section. The latter assumption may result in underestimations of the compressive strain and overestimation of the tensile strain demands at the wall edges. In the numerical model, the values of the simulated compressive strain demand are not constrained by any upper limit. For this reason, the data presented in **Figure 6.5** is capped to a strain limit of 1.0% in all the buildings. Similar to **Figure 6.2**, each dynamic analysis run is represented with a circle marker. The median and 84th percentile (p84) responses are summarized in **Table 6.3**. In general terms, the expected WM tensile strain demands in the analyzed wall pier decrease with increasing number of stories. This is because the taller buildings have ductile boundary reinforcement in a large portion of the wall edge that results in alleviation of strain demands in the wire-mesh fibers. As an example, compare the reinforcement layout provided for the W04 pier in the different building archetypes shown in **Figure 2.6**. For this reason, strain demands in the RB fibers increase in the taller buildings, as shown in **Figure 6.2c1-3**. Median compressive strain demands are in the same order of magnitude for each of the building archetypes. A short-detailed description of the strain response in relation with the selected hazard levels is provided below.

- **475-year UHS**:
    - **WM:** Median tensile strain demands in the WM fibers are in the range of 0.28% to 0.42%, which is beyond the yield limit state of the material in the latter case (ε_{sy} = 0.33%). The numerical analyses indicate that this limit is exceeded in 68% of the RHAs in the W01 piers of the 5-story buildings. This percentage reduces in the 10-story (51%) and 15-story buildings (47%) because yielding in these structures occurs first in the ductile boundary rebars. Similarly, the rupture limit in the WM reinforcement (ε_{su} = 1.5%) is reached in 3% of the cases in the 10-story building. None of the ground motions from this set subject the W01 piers in the 5- and 15-story building to such large strain demands.

- **RB:** Median tensile RB strain demands are in the range of 0.15% to 0.37%, which is beyond the yield limit state of the material in the latter case (ε_{sy} = 0.24%). The numerical analyses indicate that this limit is exceeded in 20% of the RHAs in the W01 piers of the 5-story buildings. This percentage increases in the 10-story (82%) and 15-story buildings (66%). Though ductile rebars have a rupture limit close to ε_{su} = 1.5% for monotonic loading, low-cycle fatigue may trigger this limit state at lower strain demands. Recent analytical studies have suggested a limit of ε_{su} = 5% to account for these effects (Pugh et al., 2015). This limit is only reached in 1% of the cases in the 10-story building.
- **Concrete:** Median compressive strain demands in the analyzed wall piers are approximately 0.13%, which is effectively below the strain at concrete peak strength (ε_{co} = 0.2%). Only 8% of the analysis runs generate compressive strain demands that exceed this limit state in the 5- and 10-story buildings. In the case of the 15-story buildings, the number of cases increases to 20%. Compressive strain demands larger than ε_{cu} = 0.6% are observed in only 1% of the cases for the 5- and 10-story buildings. However, as compressive strains are known to be underestimated by the modeling approach implemented herein, actual compressive strains may be higher. For example, is a factor of 2 is considered, the peak strain limit ε_{co} = 0.2% would be exceeded in more than 60% of the analyses in each building. In this case, however, strain demands larger than ε_{cu} = 0.6% are still limited to 1% to 5% of the RHAs.

- **975-year UHS**:
  - **WM:** Median tensile strain demands in the web distributed reinforcement are in the range of 0.46% to 0.78%. Yielding in the web distributed reinforcement occurs in 93% of the cases in the W01 piers of the 5-story building. This percentage reduces to 77% and 75% in the 10- and 15-story buildings, respectively. Rupture in the wire-mesh occurs in 14% of the cases in the 5-story building, 11% for the 10-story building and only in 5% of the cases in the 15-story building.
  - **RB:** Median tensile strain demands in the ductile boundary reinforcement are in the range of 0.31% to 0.69%. Yielding occurs in 62% of the cases in the W01 piers of the 5-story building. This percentage increases to 96% and 92% in the 10- and 15-story buildings, respectively. Strain demands larger than ε_{su} = 5% occur only in 8% of the cases in the 10-story building.
  - **Concrete:** Median compressive strain demands in the analyzed wall piers are approximately 0.18%, which is around the strain at concrete peak strength (ε_{co} = 0.2%). This limit is exceeded in about 40% of the cases for each building. Strain demands larger than ε_{cu} = 0.6% are observed in only 3% of the cases for the 5-story building, 7% for the 10-story and 10% for the 15-story building. If a factor of 2.0 is applied to the strain demands to account for the nonlinear strain distribution, the peak strain limit ε_{co} is exceeded in more than 90% of the RHAs, while the number of runs in which ε_{cu} is exceeded increases to 10%, 20% and 14% in the 5-, 10-, and 15-story buildings, respectively.

- **2,475-year UHS**:
  - **WM:** Median tensile strains in the web distributed reinforcement are in the range of 0.61% to 1.24%, which is very close to the rupture limit. Yielding in the web distributed reinforcement occurs in 97% of the cases in the 5-story building, 90% in the 10-story and 80% in the 15-story building. The large strain demands trigger the rupture of the steel fibers in 47% of the cases in the 5-story building. In the 10- and 15-story buildings the frequency is much lower, with values of 38% and 18% respectively. This is attributed to the presence of ductile boundary rebars in a large area of the wall edges.
  - **RB:** Median tensile strains in the boundary rebars are in the range of 0.68% to 1.08%, which is well beyond the yield limit. The yield strain is exceeded in more than 90% of the RHAs in each building. Strain demands larger than ε_{su} = 5% are observed in 6% of the cases in the 5-story building and 15% of the cases in the 10-story building.
  - **Concrete:** Median compressive strain demands in the analyzed wall piers are in the range of 0.22% to 0.27%, which exceeds by little margin the peak strain ε_{co}. In 21% of the nonlinear analyses, the compressive strain demands exceed ε_{cu} = 0.6% in the 5-story building. Lower compression demands are observed in the 10- and 15-story buildings, exceeding this limit in 20% and 17% of the cases. If a factor of 2.0 is applied to account for nonlinear strain distribution, the peak strain would be exceeded in more than 95% of the cases, while ε_{cu} would be exceeded in 35% to 45% of the RHAs.

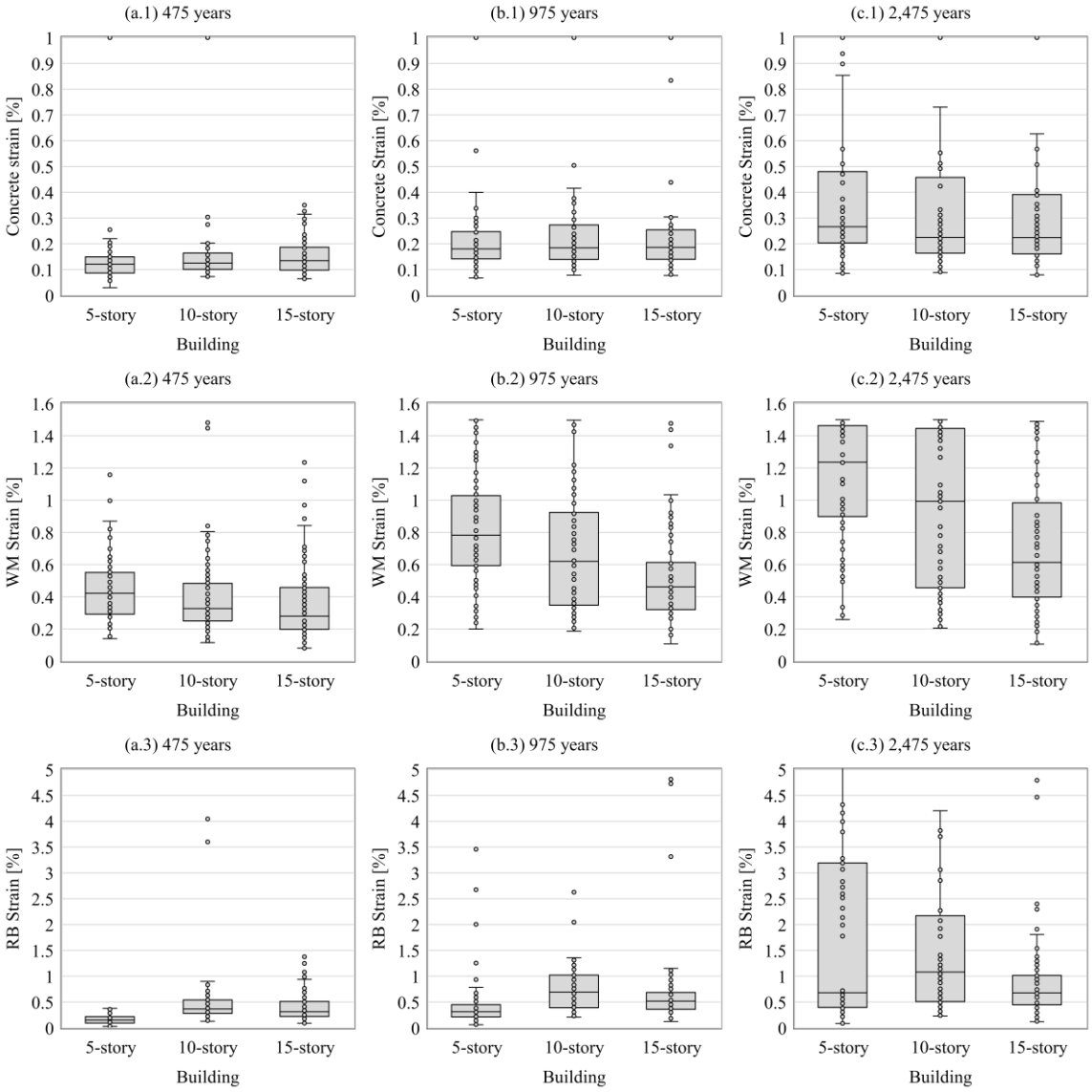

Figure 6.5 – (1) Concrete compressive strain demands, and tensile strains in the (2) wire-mesh distributed reinforcement (WM) and (3) the ductile boundary reinforcement (RB) of the W01 piers subjected to ground motions matching the (a) 475-, (b) 975- and (c) 2,475-year return period UHS.

Table 6.3 – Main statistics of the expected concrete compressive and wire-mesh (WM) strain demands in the W01 piers subjected to ground motions matching the UHS at different hazard levels.

Strain [%]		475-year UHS			975-year UHS			2,475-year UHS		
		5-story	10-story	15-story	5-story	10-story	15-story	5-story	10-story	15-story
Conc (1)	Median	0.12	0.13	0.13	0.18	0.18	0.19	0.27	0.23	0.22
	p84	0.17	0.18	0.21	0.27	0.32	0.27	0.95	1.00	0.60
WM	Median	0.42	0.33	0.28	0.78	0.62	0.46	1.24	0.99	0.61
	p84	0.64	0.57	0.51	1.15	1.13	0.81	1.47	1.48	1.34
RB	Median	0.15	0.37	0.31	0.31	0.69	0.52	0.68	1.08	0.68
	p84	0.28	0.63	0.57	0.56	1.21	0.91	4.00	3.97	1.42

(1) Concrete compressive strain demands capped to 1.0%. Compressive demands may be underestimated by a factor of 2.0, while tensile strains may be overestimated.

6.2.3 Main remarks

The results of the dynamic analyses suggest that the 5-story building is more likely to experience greater damage due to rupture of the WWM distributed reinforcement than its 10- and 15-story counterparts when subjected to earthquakes whose intensities match the UHS for different hazard levels. This is despite the fact that the demands of RDR and 1st-SDR may be greater in taller buildings. Two determinants of the apparent increased vulnerability observed in the 5-story building are (i) the absence of ductile reinforcement in its wall sections and, mainly, (ii) the mismatch between the NSR-10 design spectrum and the UHS computed for the site. The latter results in the taller buildings being designed for seismic demands with return periods in the range of 2,475 to 9,975 years, in contrast with the 475-year hazard level assigned by the NSR-10 to the design spectrum. Concrete spalling/crushing was also identified as a potential mode of failure in each of the building archetypes. While the analyses identified few cases in which the peak strain limit of concrete was exceeded for the 475-year and 975-year UHS, recent research has shown that the compressive strain demands may be underestimated using the modeling approach implemented in this study by a factor of 2.0. If this was the case, the peak strain limit is expected to occur in around 60% of the RHAs matching the 475-year UHS and 90% for the 975-year UHS. However, considering that strain demands decrease along the web, the exceedance of this limit might affect a small portion of the wall without resulting in noticeable damage. If a larger strain limit is accepted (e.g. ε_{cu} = 0.6%), the onset of concrete crushing occurs in maximum 5% of the cases for buildings subjected to the 475-year UHS.

This section evaluated the dynamic response of building archetypes when subjected to the demands of UHS-targeted ground motions at various hazard levels, following the most widespread practice for structural vulnerability assessment. However, recent research has shown that the structural responses obtained with this approach cannot be used for risk analysis because the use of UHS conservatively implies that large values of spectral acceleration will occur in all periods of a single ground motion. Instead, Baker (2011) proposes the use of CMS as the target spectrum because its spectral shape is consistent with the expected mean spectrum for the site provided a spectral acceleration is conditioned at a reference period. Following this philosophy, the methodology presented in **Chapter 3** extends the use of the CMS to form a set of ground motions (termed as the CSS) whose spectral shapes are compatible with the expected mean spectrum in wide range of intensities and with assigned occurrence rates that reproduce the seismic hazard at the site. The following sections of this chapter will make use of the CSS set to quantify the vulnerability and risk of the building archetypes.

6.3 Fragility analysis

The building archetypes were subjected to several RHAs using the complete CSS ground motion set. Since the seismic behavior of the buildings is simulated using 2D models, the response to each horizontal component of the records was evaluated independently. The result was a total of 696 RHAs for each archetype. The wide range of intensities covered by the CSS allows evaluating the response of the structure in the elastic range and well within the inelastic range of behavior. The results of the RHAs can be used to construct fragility curves of different structural responses. **Figure 6.6** shows the dataset obtained from the RHAs using the CSS set for each of the building archetypes. Selected engineering

demand parameters (EDPs) correspond to maximum roof and first-story drift ratios (RDR and 1st-SDR), maximum normalized base shear $V_{b,max}/W$, and strain demands in the outermost concrete and steel fibers of the W01 piers. The RDR, 1st-SDR and $V_{b,max}/W$ are plotted against the corresponding spectral acceleration of each ground motion record at the fundamental period, $S_a(T_1)$. The data is shown in log-log scale due to the inherent variability in the responses. Approximately constant dispersion in the log-log plots is observed for each of the EDPs, which indicates increasing dispersion of the response for increasing values of $S_a(T_1)$. This indicates that $S_a(T_1)$ by itself might not be the best predictor of the selected EDPs. This is in contrast with the traditional design philosophy that estimates equivalent static lateral forces from $S_a(T_1)$ that are later used to predict unique values of displacements. While other ground motion parameters could be used as intensity measures (IMs) for fragility analysis, such as the peak ground velocity (PGV) (Hoult et al., 2019), this study will continue using $S_a(T_1)$ because of its widespread use in the engineering community. The results from the RHAs using the CSS set in **Figure 6.6a-c** show that the displacement demands tend to increase with increasing number of stories for any given level of $S_a(T_1)$. These EDPs also increase with increasing $S_a(T_1)$, as expected. The normalized base shear also increases with increasing $S_a(T_1)$, but shows similar values for each building at fixed values of $S_a(T_1)$. Strain demands are plotted in **Figure 6.6d-f** against the observed 1st-SDR demands. As expected, increasing 1st-SDR results in increased axial strains in the walls. Data shows a strong correlation between displacements and strains for 1st-SDR < 0.3% for each building. This is consistent with the level of 1st-SDR associated to the peak strength. Values of 1st-SDR > 0.3% result in rapidly increasing strains until failure is achieved in many cases.

The response data set in **Figure 6.6** can be gathered and treated statistically to estimate fragility curves, as explained in **Section 3.5**. Fragility curves usually relate the probability of exceedance of a damage indicator to an intensity measure. This study uses the RDR and 1st-SDR as the damage indicators for the fragility curves, while the intensity measure is $S_a(T_1)$. The reason why RDR and 1st-SDR are chosen is because the structural response of the building archetypes was already detailly characterized with respect to these EDPs in **Chapter 5**, with the latter being strongly correlated to damage. In addition, these structural responses can be easily compared to the experimental limit states found in the literature for thin RC walls that were already discussed in **Chapter 2**. The obtained fragility curves for RDR and 1st-SDR at different response levels are shown in **Figure 6.7** and **Figure 6.8**. The elastic NSR-10 design spectral acceleration for the building archetypes is shown in dotted lines ($S_a(T_1)$ = 0.81 *g* for the 5- and 10-story buildings, and 0.64 *g* for the 15-story archetype). These results allow for the estimation of probability of exceedance of a given displacement demand (RDR or 1st-SDR) in the case-study buildings when subjected to ground motions matching the spectral ordinates of the NSR-10 design spectrum at the fundamental period. The estimated probabilities along with the statistical parameters of the fragility functions are summarized in **Table 6.4**.

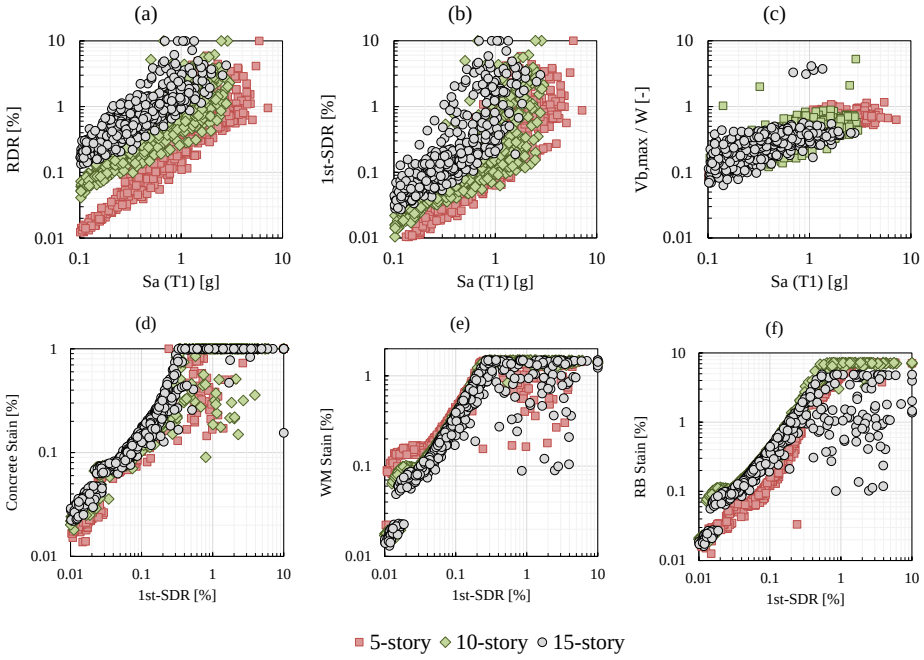

Figure 6.6 – Global EDPs from CSS runs of the nonlinear RC wall building models: (a) roof drift ratio (RDR), (b) first-story drift ratio (1st-SDR), (c) normalized base shear versus spectral acceleration $S_a(T_1)$; and (d) concrete compressive strains, (e) tensile strains in the wire-mesh (WM) distributed reinforcement and (f) tensile strains in the ductile boundary reinforcement (RB) in the W01 piers versus 1st-SDR.

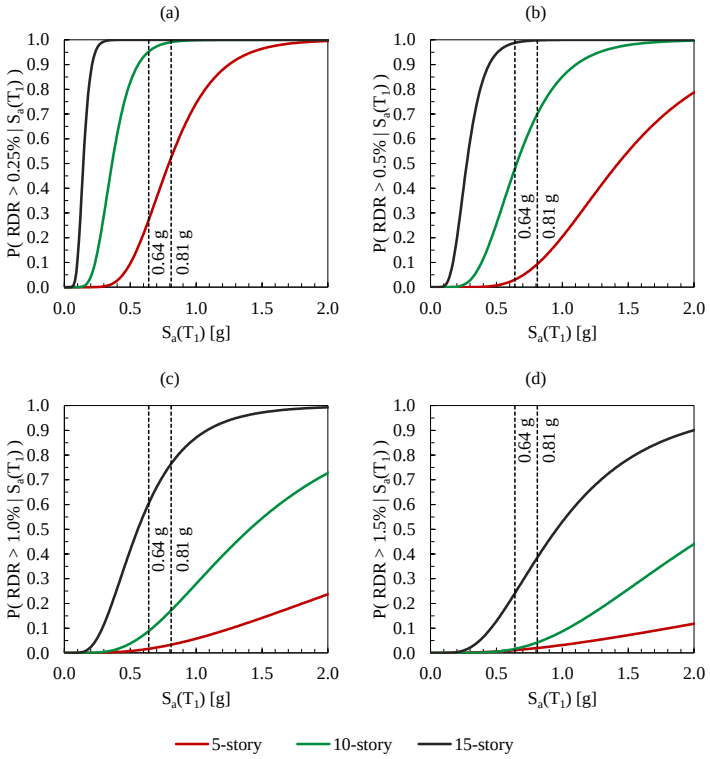

Figure 6.7 – Fragility curves for the maximum demands of roof drift ratio (RDR) in each of the building archetypes. Selected RDR levels are (a) 0.25%, (b) 0.5%, (c) 1.0% and (d) 1.5%.

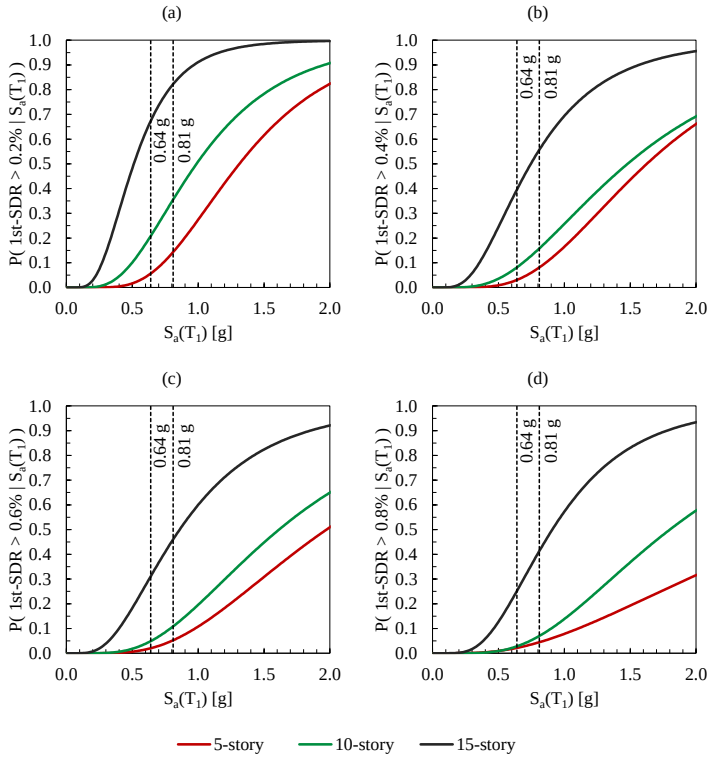

Figure 6.8 – Fragility curves for the maximum demands of first-story drift ratio (1st-SDR) in each of the building archetypes. Selected 1st-SDR levels are (a) 0.2%, (b) 0.4%, (c) 0.6% and (d) 0.8%.

Table 6.4 – Summary of displacement fragility of the case-study buildings subjected to ground motions with spectral ordinates consistent with the NSR-10 at the fundamental period.

EDP	Test value	P(EDP >Test value | S_a (T_1),NSR-10) [%]			Mean and standard deviation					
		5-story	10-story	15-story	5-story		10-story		15-story	
		S_a (T_1) = 0.81	S_a (T_1) = 0.81	S_a (T_1) = 0.64	μ_{Sa} [g]	σ_{lnSa}	μ_{Sa} [g]	σ_{lnSa}	μ_{Sa} [g]	σ_{lnSa}
RDR [%]	> 0.25 ?	52	99	100	0.79	0.35	0.36	0.34	0.14	0.30
	> 0.5 ?	9.3	70	99	1.42	0.43	0.65	0.41	0.27	0.37
	> 1.0 ?	3.3	17	61	3.56	0.80	1.40	0.58	0.56	0.52
	> 1.5 ?	2.0	4.2	24	6.82	1.03	2.18	0.57	0.96	0.57
1st-SDR [%]	> 0.2 ?	14	36	67	1.31	0.45	0.99	0.53	0.51	0.50
	> 0.4 ?	8.0	16	40	1.63	0.50	1.48	0.60	0.74	0.58
	> 0.6 ?	5.0	11	31	1.97	0.55	1.61	0.56	0.86	0.60
	> 0.8 ?	4.0	7.0	25	2.85	0.74	1.80	0.54	0.91	0.52

The results presented in **Figure 6.7** indicate that the probability of exceeding specific values of RDR increases with increasing number of stories. The RDR demands can be related to the limit states identified from the pushover analysis in **Section 5.1**. Particularly, the pushover curves reached the peak strength at RDR demands of approximately 0.5%, 1.0% and 1.3% for the 5-, 10- and 15-story buildings, respectively. The obtained fragility curves estimate that the probability of exceeding such RDR values is 0.09 for the 5-story building, 0.17 for the 10-story and 0.24 for the 15-story for ground motion intensities consistent with the NSR-10 design spectrum. Similar conclusions are

obtained when analyzing the fragility of 1st-SDR, a parameter that is more related to damage in this type of building. The pushover curves in terms of 1st-SDR in **Figure 5.6** indicate that the maximum strength of the building archetypes is reached at SDR levels between 0.2% and 0.4%. **Figure 6.8** shows that the probability of exceeding this limit under design earthquake demands is between 0.08 and 0.14 for the 5-story building, 0.16 to 0.36 for the 10-story building and between 0.40 and 0.67 for the 15-story building. These results indicate that taller buildings are more vulnerable to high seismic demands and may exhibit significant displacements subject to ground motions consistent with the design earthquake. The increase in vulnerability for taller buildings can be explained from their modal properties. As the number of stories increases, and consequently the elevation of the building, the structural period increases, and the structure enters in the displacement-controlled region of the response spectrum. The effect of the structural period on the vulnerability and seismic risk of thin RC wall buildings will be explored in Chapter 7.

The results of the fragility analysis revealed that taller thin wall buildings are more susceptible to high displacement demands when subjected to design earthquake excitation. However, this does not necessarily imply that the seismic risk to which these buildings are exposed is higher than its lower-rise counterparts. In fact, the preliminary analyses of the RHAs in **Section 6.2**, where the UHS was used as the target spectrum, revealed that the demands of the design earthquake exceed the expected at the site at hazard levels between 475 and 2475 years for structures with $T > 0.5$ s. The following section will use the results of the fragility analysis to estimate the risk based on assigned occurrence rates for each ground motion record.

6.4 Estimation of EDP-Risk

Fragility analysis results can be linked to the hazard at the site to produce risk estimates. In the CSS methodology, each of the EDPs obtained with the RHAs is assigned the same rate of occurrence as the ground motion that generates it. In this way, it is possible to directly estimate the annual frequency with which an EDP level is exceeded using **Equation (3.5)**. The ground motion records of the CSS generated in **Section 3.4** have assigned rates of occurrence that assume that the two horizontal components of the record occur simultaneously. As in this analysis the horizontal components are treated as individual records, the rates of occurrence of each component are assigned as half of the corresponding RotD50 spectrum in the CSS. **Figure 6.9** and **Figure 6.10** show scatter plots relating the maximum roof and first-story drift ratios (RDR and 1st-SDR) and the strain demands recorded at the outermost fibers in the W01 piers of the 10-story building to the corresponding rate of occurrence of the ground motion that generates them. The rate-versus-RDR data clouds are continuous for a wide range of RDR levels. On the other hand, the rate-versus-1st-SDR responses start deviating from the initial trend at 1st-SDR levels of 0.3% - 0.5%, which is the 1st-SDR associated to the peak pushover strength of the building archetypes. This instability behavior is also observed in the strain demands in **Figure 6.10** after significant incursions in the inelastic range**,** and confirms that 1st-SDR is well correlated with damage. Similar trends are observed for the 5- and 15-story buildings.

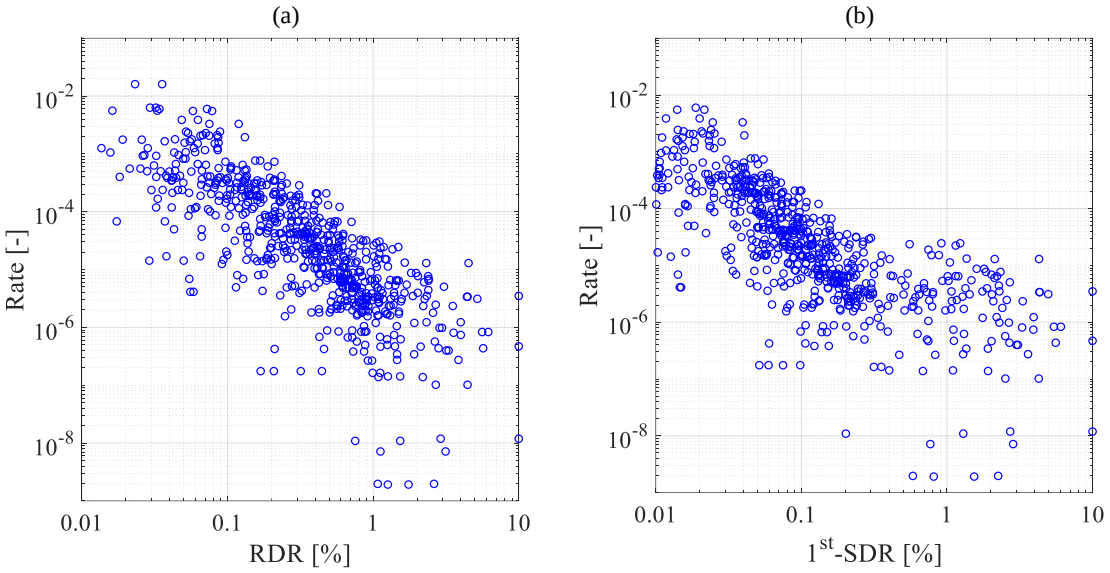

Figure 6.9 – Rates of occurrence versus displacement for the 10-story building: (a) maximum roof drift ratio (RDR) and (b) maximum first-story drift ratio (1st-SDR).

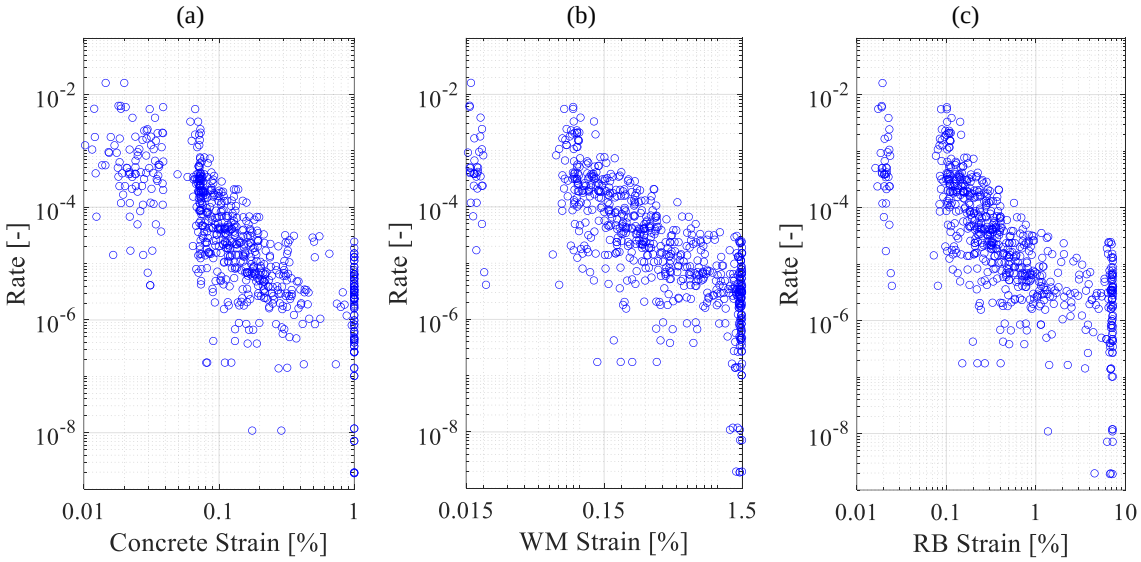

Figure 6.10 – Rates of occurrence versus axial strains for the 10-story building: (a) concrete in compression, (b) wire-mesh (WM) distributed reinforcement and (c) ductile boundary reinforcement (RB).

6.4.1 Displacement demands

Figure 6.11 shows EDP-risk curves estimated with **Equation (3.5)** for the RDR and 1st-SDR in the three building archetypes. The results in **Figure 6.11a** indicate that taller buildings have a greater risk of sustaining larger RDR demands than their low-rise counterpart. For instance, the return period of RDR > 0.5% is about 860 years for the 5-story building, 400 years for the 10-story building and 350 years for the 15-story building However, as previously explained in **Section 5.3,** the RDR is not an objective damage measure when comparing buildings of different heights because the RDR in taller buildings exhibits larger contributions from elastic displacements of the upper stories. As most of the

plasticity concentrates in the first-story, the 1st-SDR is a more objective damage measure. **Figure 6.11b** presents the calculated risk of exceedance of the 1st-SDR. The results suggest that low to moderate values of 1st-SDR (0.1% to 1.0%) have a greater risk to be exceeded in the 5-story building. This agrees with the results obtained using the UHS-targeted RHAs in **Section 6.2**. The return period of 1st-SDR > 0.3%, which is the displacement demand associated to the peak pushover strength, is approximately 1,000 years for the 5-story building, 1,700 years for the 10-story building, and 2,000 years for the 15-story building. On the other hand, the experimental-database analysis from **Section 1.3** suggested that thin RC walls are able to sustain a maximum 1st-SDR of 0.8-1.0%. This performance limit has a return period of 2,700 to 5,000 years according to the EDP-risk curves from **Figure 6.11b**. In general terms, the risk curves of 1st-SDR the 10- and 15-story buildings are similar at return periods lower than 975 years, while the RDR-risk is always higher in the 15-story building. For example, at the 475-year return period, the expected RDR is 0.54% for the 10-story building and 0.62% for the 15-story building. However, the expected 1st-SDR at this return period is 0.13% for both buildings.

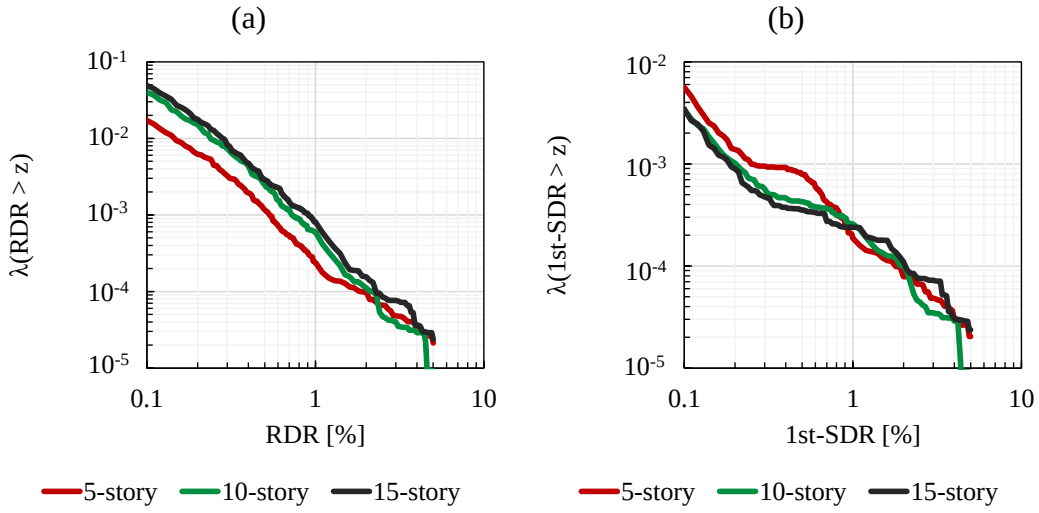

Figure 6.11 – Annual rate of exceedance of the maximum (a) roof drift ratio (RDR) and (b) first-story drift ratio (1st-SDR) in the building archetypes.

6.4.2 Strain demands

Figure 6.12a presents the estimated annual rates of exceedance of the axial strains recorded in the W01 piers of the three building archetypes. Concrete compressive strains exhibit similar rates for deformation demands lower than ε_{co} = 0.2%. For larger strains, the EDP-risk increases in the 5-story building. The peak strain ε_{co} has a return period of 600 years for the 5-story building, 900 years for the 10-story building and 574 years for the 15-story building. The ultimate strain limit considered in this study, ε_{cu} = 0.6%, has a return period of 1,600 years for the 5-story building, 2,800 for the 10-story building and 2,400 years for the 15-story building. Note that these compressive strain demands are calculated using a modeling approach that assumes a linear distribution of vertical strains along the wall section. This may result in the underestimation of the compressive strain in the outermost fibers. If a factor of 2.0 is used to account for these effects, the return period of the peak strain ε_{co} reduces to around 100-150 years for all the building archetypes, indicating that

this limit is likely to be surpassed; for example, there is a 30% chance of being exceeded in 50 years. Similarly, the return period of the ultimate strain ε_{cu} reduces to 1,200-1,400 years. The adjusted return periods of ε_{co} are below the target return period of 475 years assigned by the NSR-10 to the design spectrum. However, given that strains get reduced along the wall, it is unlikely that the exceedance of this limit translates into significant damage.

Figure 6.12b shows the EDP-risk curves estimated for the tensile strains in the wire-mesh distributed (WM) reinforcement in the W01 piers. The results indicate that expected annual rates of exceedance decrease with an increasing number of stories. This agrees with the results obtained in **Section 6.2** using UHS-targeted ground motions, where the 5-story buildings exhibited larger WM strain demands. The decrease in the risk of the WM strains in taller buildings is explained by the inclusion of larger amounts of ductile boundary reinforcement (RB) to compensate for the increased design flexural demands. This addition of RB constraints the placement of the WM reinforcement to a smaller region towards the wall centroid (for instance, compare the reinforcement layout of the W04 piers in **Figure 2.6**). The onset of yielding of the WM fibers (ε_{sy} = 0.33%) has a return period of 135 years for the 5-story building, and about 300 years in the 10- and 15-story buildings. Rupture of the WM, experimentally reported to occur at strain levels ε_{su} of 1.25 to 1.50%, has a return period of 1,000 years for the 5-story building, 1,500 years in the 10-story building, and 3,000 years for the 15-story building.

Figure 6.12c shows the estimated annual rates of exceedance for the tensile strains in the ductile boundary reinforcement (RB) in the W01 piers. The results indicate that taller buildings have a greater risk of exceeding RB strains lower than 1.0%. This is expected as the RB reinforcement allows the taller building to sustain larger lateral deformations at the cost of increasing the tensile strain demands in the wall edges. Beyond the 1.0% strain limit, the results invert and the risk of exceedance increases with a decreasing number of stories. A plausible explanation for this behavior may be that such large strains are sustained by the walls after the onset of rupture of the WM occurs. The onset of yielding of the RB reinforcement (ε_{sy} = 0.24%) has a return period of 415 years for the 5-story building, and about 100 years in the 10- and 15-story buildings. On the other hand, the low-cycle fatigue limit of ε_{su} = 5% used in this study has a return period of 4,000 years for the 5-story building, 2,500 years in the 10-story building, and 10,000 years for the 15-story building.

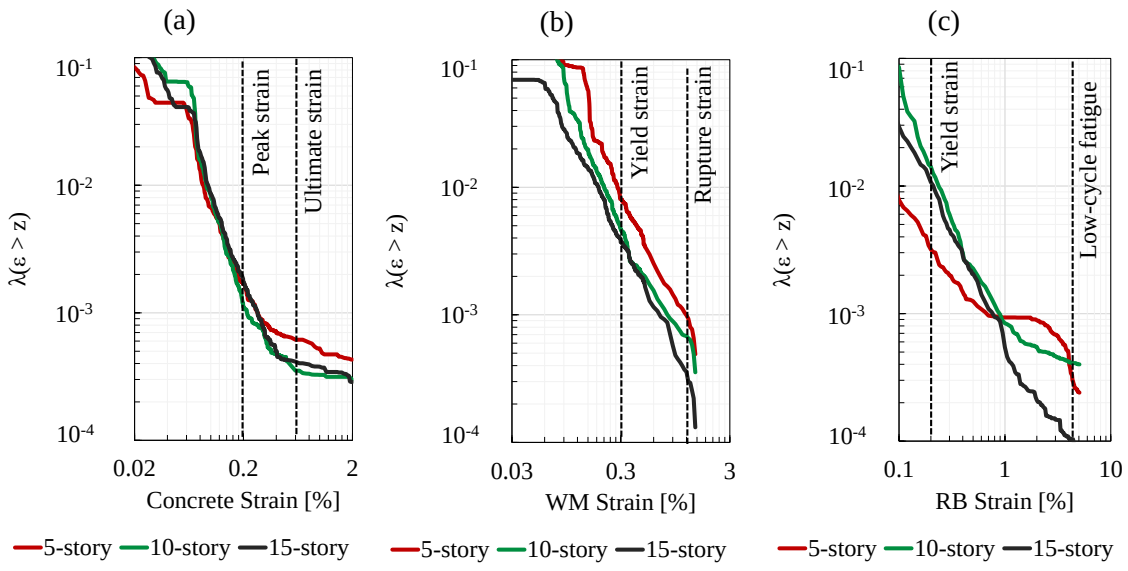

Figure 6.12 – Annual rate of exceedance of the maximum strains in the outermost (a) concrete, (b) wire-mesh (WM) and (c) ductile-boundary reinforcement (RB) fibers in the W01 piers of the building archetypes.

The return periods estimated in **Subsections 6.4.1** and **6.4.2** can also be expressed in terms of the probability of exceedance in a given time interval assuming that the phenomenon studied follows a Poisson distribution. Typically, this time interval is set as 50 years in engineering practice. An event with a return period of 475 years is then interpreted as one that has a 10% probability of exceedance in 50 years. The results of applying this concept to the return periods obtained for displacements and strains are presented in **Table 6.5**.

Table 6.5 – Return period and probability of exceedance in 50 years of specific values of EDP for the case-study buildings.

EDP	Test value	5-story		10-story		15-story	
		T_R [years]	P. in 50 years [%]	T_R [years]	P. in 50 years [%]	T_R [years]	P. in 50 years [%]
1st-SDR [%]	> 0.3 ?	1,050	4.7	1,770	2.8	2,100	2.4
	> 0.5 ?	1,270	3.9	2,400	2.1	2,830	1.8
	> 0.8 ?	2,730	1.8	3,190	1.6	3,900	1.3
	> 1.0 ?	5,300	0.9	3,870	1.3	4,174	1.2
Conc. Strain (1) [%]	Peak	150 - 600	8.0 - 28	120 - 900	5.4 - 34	115 – 575	8.3 - 35
	Crushing	1,160 - 1,630	3.0 - 4.2	1,360 - 2,850	1.7 - 3.6	1,270 - 2,420	2.0 - 3.9
WM Strain [%]	Yield	135	31	250	18	300	15.4
	Rupture	1,075	4.5	1,530	3.2	3,350	1.5
RB Strain [%]	Yield	415	11.4	100	39.3	130	31.9
	Fatigue	4,130	1.2	2,490	2.0	10,000	0.5

(1) A range of plausible values of return period as the result of applying factors of 1.0 and 2.0 to the obtained strain demands to account for nonlinear strain distributions.

6.4.3 Contribution from the different tectonic settings

The CSS ground motion set used in this study has assigned rates of occurrence that reproduce the seismic hazard in the city of Armenia for the site conditions of the archetype buildings. As shown in **Figure 3.10**, the CSS set replicates not only the total hazard but the contribution of each tectonic setting. This allows estimates to be made as to which types of earthquakes have the highest risk of generating specific EDP values. **Figure 6.13** presents the estimated annual rates of exceedance of the EDPs of interest in this study (1st-SDR and axial strains) and their deaggregation by tectonic setting for the 10-story building. The results indicate that crustal earthquakes contribute the most to the seismic risk of the 1st-SDR for return periods greater than 500 years, followed by interface subduction earthquakes. The structural demands generated by these types of earthquakes are likely to be beyond the elastic limits, and in less frequent scenarios, close to the onset of material brittle failures. In contrast, elastic displacement and strain demands are more likely to result from intraslab subduction earthquakes (return periods lower than 500 years). This is consistent with the hazard curves in **Figure 3.6**, which showed that the hazard at lower return periods is controlled by intraslab earthquakes and that interface and crustal earthquakes contributed the most to higher return-period hazard levels.

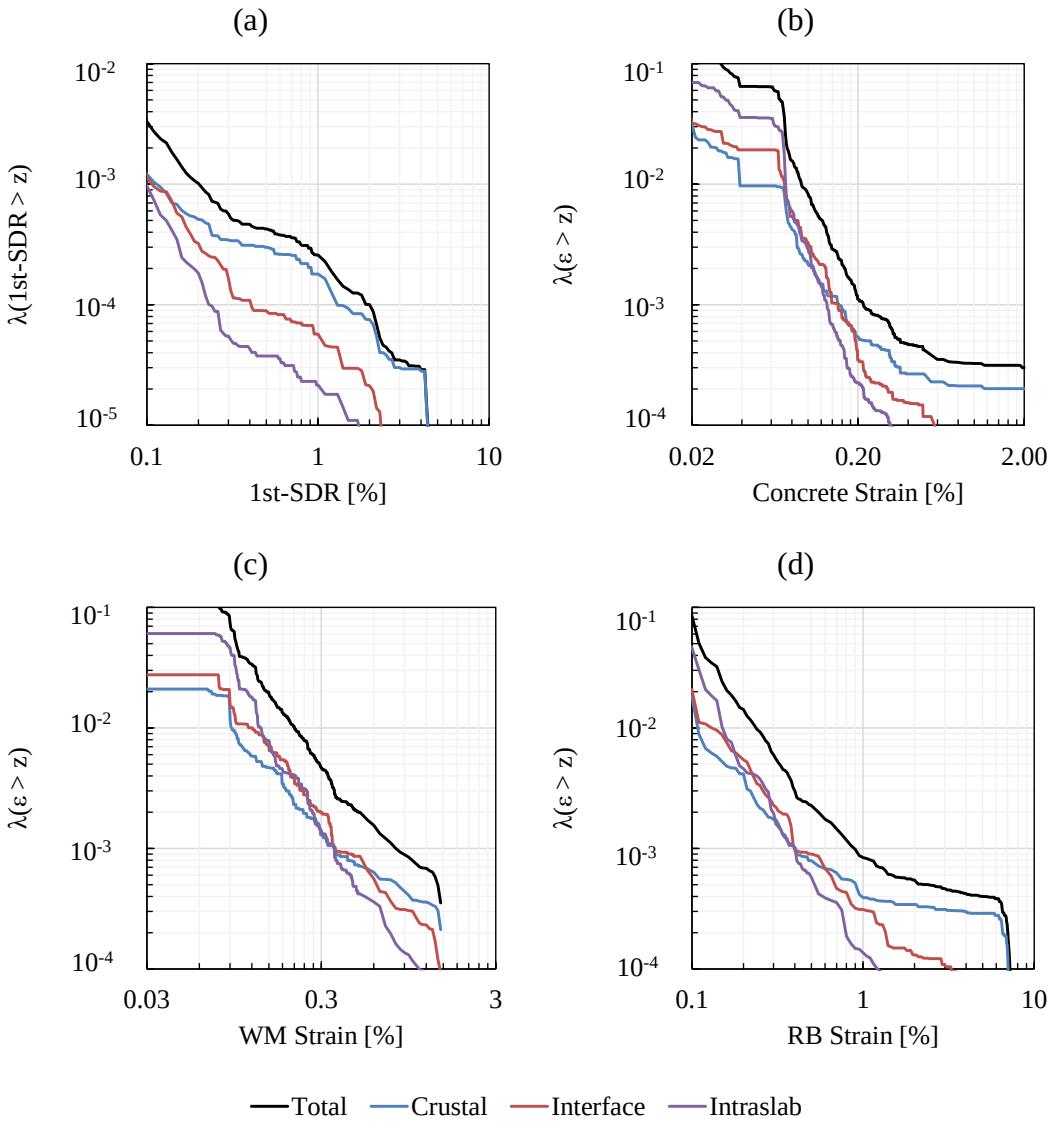

Figure 6.13 – Annual rate of exceedance of major EDPs deaggregated by tectonic setting for the 10-story building: (a) maximum first-story drift ratio (1st-SDR), and (b) concrete compressive strains, (c) wire-mesh (WM) tensile strains and (d) ductile-boundary-reinforcement (RB) tensile strains in the W01 piers.

6.4.4 Main remarks

The results of the fragility analysis confirmed that high-rise thin wall buildings are more vulnerable to ground motions with intensities similar to those of the NSR-10 design earthquake. However, when comparing the structural vulnerability with the seismic hazard of the site, it was found that the actual seismic risk in the taller structures is lower than in their lower-rise counterparts. This is so because the demands imposed by the design earthquake on flexible structures correspond to seismic hazard levels with return periods much longer than the one assigned by NSR-10, which is 475 years. It was found that the failure limit states with the highest annual rate of exceedance are concrete crushing and rupture of the wire-mesh reinforcement. Recognizing the limitations of the model implemented here to simulate the non-linear distribution of deformations along the wall,

adjustments were made to the compression demands using a factor of 2.0, in line with the level of underprediction of compressive strains observed in the literature. The risk-based analyses suggest that the probability of exceeding the limits of good structural behavior at the global and local level is less than 10% in 50 years. It was observed that the inclusion of ductile reinforcing steel at the edges of the walls helps to reduce the probability of rupture in the wire-mesh web distributed reinforcement. Further research is required to determine if the observed performance is a result of the particular configuration of the building archetypes being analyzed.

Chapter 7 – Effect of Stiffness and Structural Period on the Seismic Performance

The risk analyses in the previous chapter showed that buildings with higher number of stories are less likely to exceed the limits of good structural behavior despite being more vulnerable to high seismic demands. One possible explanation is that high-rise buildings have longer structural periods, for which the ordinates of the NSR-10 design spectrum are associated with higher hazard levels as opposed to those of the shorter periods. To further study this observation, the 10-story building archetype is modified to generate a new set of buildings with reduced a wall area index (WAI) and increased structural period. The modified buildings are again subjected to the demands imposed by the ground motions of the CSS set and the respective fragility and hazard curves are calculated.

7.1 Modified 10-story building archetypes

Figure 7.1a shows the structural plan of the 2D model of the 10-story building archetype. This structural model, referred to from now on as B0, was modified to generate three additional buildings with different wall area index (WAI) (and therefore different structural period). The structural floor plans of the modified versions are shown in **Figure 7.1b-c**. In the B1 model, the length of the W01 and W04 piers was reduced without changing their boundary reinforcement. The shorter rectangular walls were additionally eliminated and the L-shaped walls were converted to rectangular. In building B2, the W01 piers were eliminated and the length of the W04 piers was reduced as in building B1. The rest of the structural floor was kept the same as in B0. The B1-T building has the same structural plan as B1 but its seismic mass was artificially adjusted so that the structural period coincided with that of the B0 building. This is done to evaluate not only the impact of the stiffness and strength on the structural response, but also the natural period, which will make the structure sensitive to other portions of the frequency content of the ground motions. Minimal changes were done to the initial reinforcement layout to accommodate the new seismic demands. Because the default B0 exhibits design story drifts that are well below the 1.43% limit required by NSR-10, the introduced modifications still result in code-compliant buildings. The resulting WAI and other characteristics of the modified buildings are summarized in **Table 7.1**.

Table 7.1 – Return period and probability of exceedance in 50 years of specific values of EDP for the case-study buildings.

Building	T [s]	WAI [%]	Seismic weight[(1)] W [kN]	Design base shear [(2)] V_{EW} [kN]	Design base shear coefficient C_s [-]
B0	0.56	3.04	19859	2582	0.13
B1	0.65	2.30	18351	2386	0.13
B2	0.82	2.11	17378	1919	0.11
B1-T	0.56	2.30	13215	1718	0.13

(1) Half of the actual weight of the equivalent 3D structures.
(2) Consistent with the seismic weight. It includes reduction by *R* and scaling to 80% of the ELL base shear.

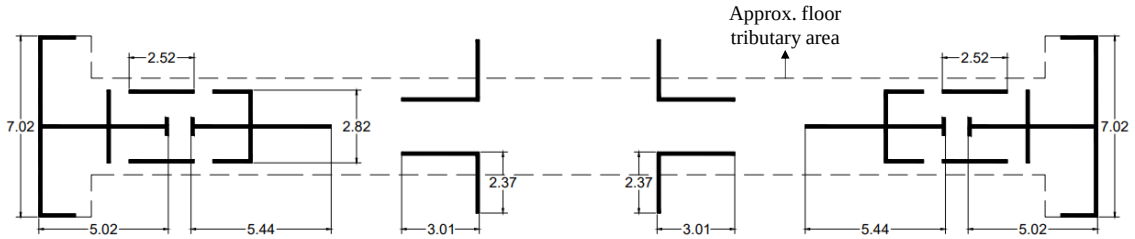

(a) Default 10-story building model (B0)

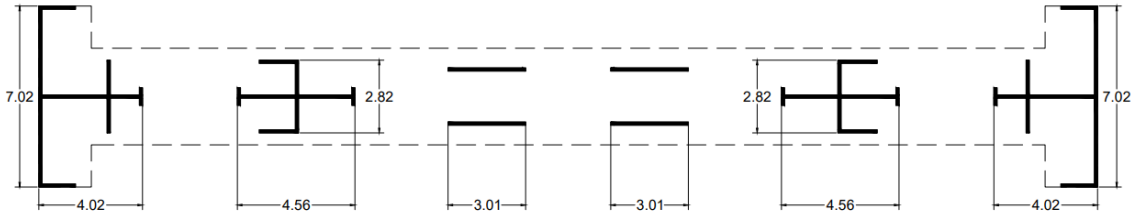

(b) Modified versions B1 and B1-T

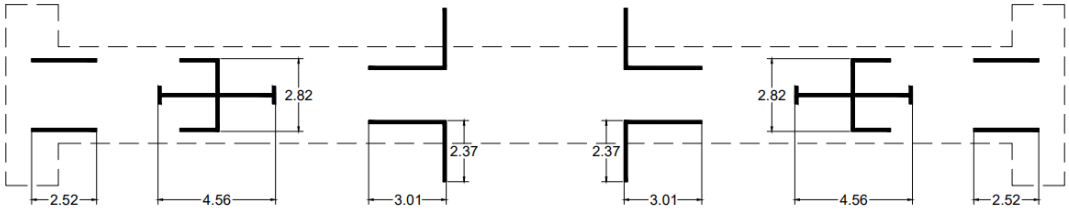

(c) Modified version B2

Figure 7.1 – Structural layout of the modified 10-story building archetypes.

Figure 7.2 depicts the pushover response of the modified archetypes in terms of both the first-story drift ratio (1st-SDR) and the roof drift ratio (RDR). The normalized base shear strength decreases with a decreasing WAI, except for the B1-T model that exhibits larger normalized strength due to its reduced seismic weight. The pushover stiffness of the buildings also decreases with decreasing WAI as expected, except for the B1-T model, which has the same initial stiffness as B0. Increased roof displacement capacity (RDR) is observed for decreasing WAI (**Figure 7.2b**). This does not translate necessarily to the 1st-SDR response (**Figure 7.2a**), where the B1 and B2 models have about the same 1st-SDR capacity. As in the analyses of the original building archetypes, the 1st-SDR at which the peak strength of the system is reached is consistent in the four buildings and is in the range of 0.25% to 0.35%. The observed relationship between the WAI and the pushover response agrees with the results obtained by Cando et al. (2020) for a series of 20-story buildings with different WAI in Chile.

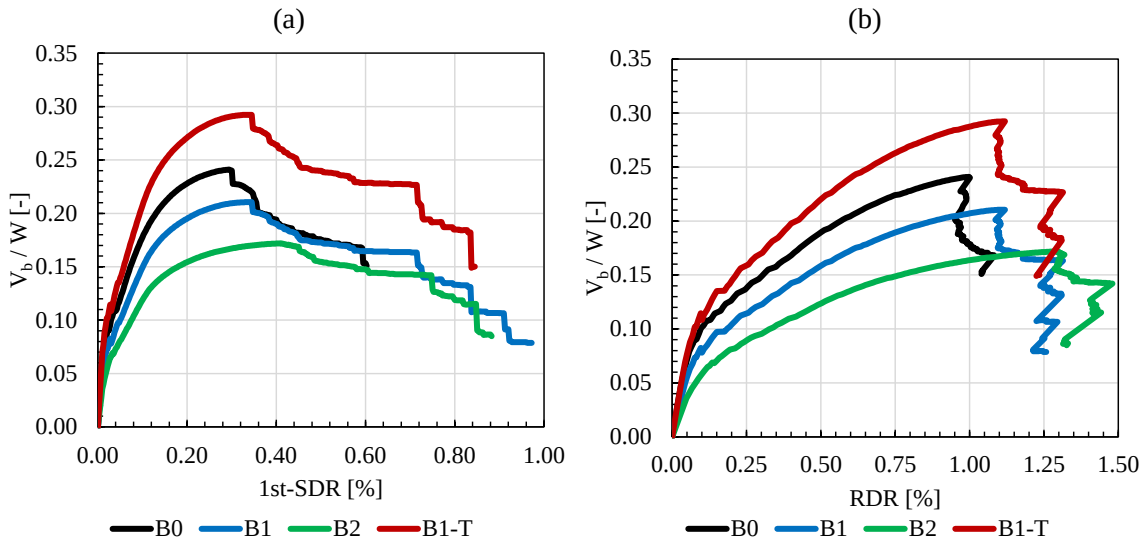

Figure 7.2 – Pushover response of the modified 10-story building archetypes in terms of (a) first-story drift ratio (1st-SDR) and (b) roof drift ratio (RDR).

7.2 Effect on the dynamic response under UHS-targeted ground motions

The modified 10-story buildings were subjected to the UHS-targeted ground motion sets from **Figure 6.1** to get an insight on the influence of the WAI (i.e. the stiffness) and the structural period in the performance at different hazard levels. **Figure 7.3** presents the maximum 1st-SDR demands sustained by the modified 10-story buildings when subjected to the 475-, 975- and 2,475-year UHS-targeted ground motion sets. Increasing displacements are observed with a decreasing WAI at each of the hazard levels analyzed. The exception to this trend is the B1-T, which exhibits 1st-SDR demands that are in the same order of magnitude as the sustained by the B0 building, and are even sometimes less. Even though the buildings with reduced stiffness exhibit larger 1st-SDR demands, the median response does not exceed the limit of 0.3% at which the pushover strength is reached for any of the hazard levels. The obtained results indicate that the expected displacement demands are directly related to the structural period of the system and not only its stiffness. In this case, the responses consistently exhibit an increasing trend with the structural period. This is in contrast with the results obtained in **Figure 6.2** for the original 5-, 10- and 15-story building archetypes, where the shorter-period low-rise buildings exhibited larger demands in the first story. These differences suggest that other factors, such as the height of the building or the inclusion of ductile longitudinal reinforcement, also impact the performance of thin RC wall buildings.

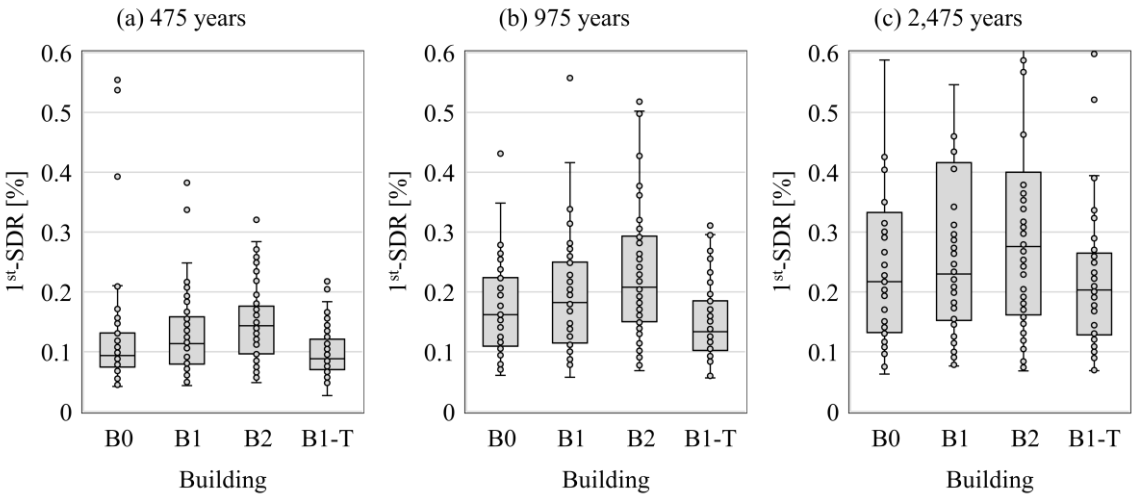

Figure 7.3 – First-story drift ratio (1st-SDR) demands exhibited by the modified 10-story building archetypes subjected to ground motions matching the (a) 475-, (b) 975- and (c) 2,475-year return period UHS.

7.3 Effect on the estimated fragility curves

Figure 7.4 presents the fragility curves of the modified 10-story buildings for different levels of 1st-SDR. The ordinates of the NSR-10 design elastic spectrum at the fundamental period of the structures are additionally marked. The curves indicate that by decreasing the WAI, the structure is more vulnerable to high seismic demands, which is expected. The exception is the B1-T model, which despite having a lower WAI, is less vulnerable than all other buildings. This indicates that buildings with low WAI can perform well if the structural period is sufficiently low. For structures with fundamental periods close to the displacement-controlled region of the response spectrum, reductions in WAI translate into increased 1st-SDR demands for a given seismic intensity. It is worth noting that although increasing the WAI makes the structure more vulnerable as compared to the default model, it may eventually result in a lower probability of exceedance when contrasted with the elastic design demand because of the increased structural period. Consider for example building B2, which has a WAI of 2.11% and a period of 0.82 s. For this period, the design spectral acceleration is $S_a(T_1)$ = 0.68 g, while that of the other models is in the design spectrum plateau, with $S_a(T_1)$ = 0.81 g. When comparing the exceedance probabilities of 1st-SDR for demands consistent with the NSR-10 spectrum, building B2 ends up being as vulnerable as building B1 for 1st-SDR ≥ 0.4%. The estimated probabilities along with the statistical parameters of the fragility functions are summarized in **Table 7.2**.

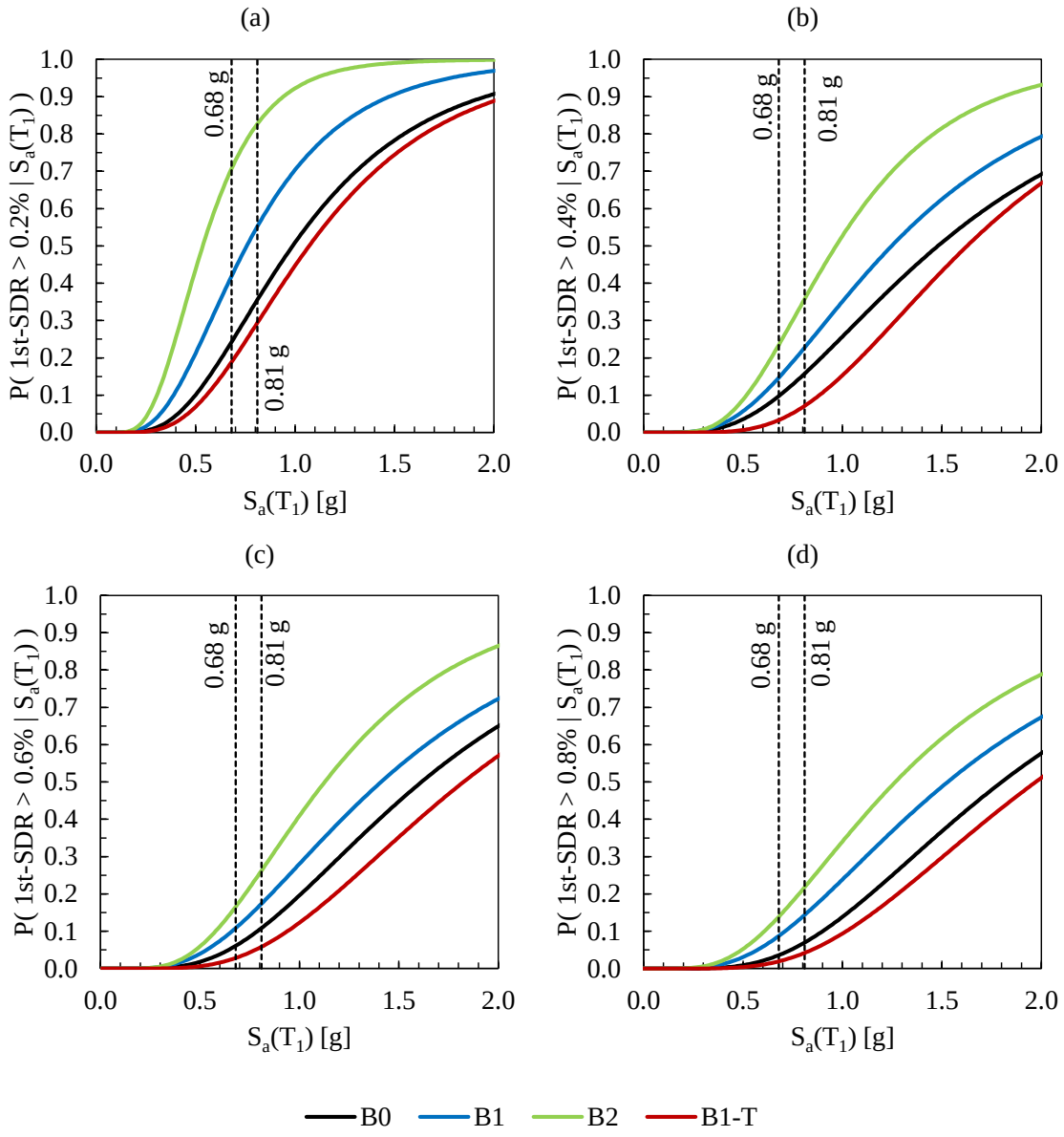

Figure 7.4 – Fragility curves for the maximum demands of first-story drift ratio (1st-SDR) in each of modified 10-story buildings. Selected 1st-SDR levels are (a) 0.2%, (b) 0.4%, (c) 0.6% and (d) 0.8%.

Table 7.2 – Summary of displacement fragility of the case-study buildings subjected to ground motions with spectral ordinates consistent with the NSR-10 at the fundamental period.

1st-SDR [%]	P(EDP >Test value | S_a (T_1),NSR-10) [%]				Mean and standard deviation							
	B0	B1	B2	B1-T	B0		B1		B2		B1-T	
	S_a (T_1) = 0.81	S_a (T_1) = 0.81	S_a (T_1) = 0.68	S_a (T_1) = 0.81	μ_{Sa} [g]	σ_{lnSa}	μ_{Sa} [g]	σ_{lnSa}	μ_{Sa} [g]	σ_{lnSa}	μ_{Sa} [g]	σ_{lnSa}
> 0.2 ?	36	55	71	29	0.99	0.53	0.76	0.52	0.54	0.44	1.07	0.51
> 0.4 ?	16	23	23	7	1.48	0.60	1.25	0.58	0.97	0.49	1.63	0.47
> 0.6 ?	11	17	17	6	1.61	0.56	1.41	0.59	1.13	0.52	1.82	0.52
> 0.8 ?	7.0	14	14	4	1.80	0.54	1.52	0.60	1.27	0.57	1.97	0.52

7.4 Effect on the EDP-risk

Fragility analyses revealed that the WAI and the structural period greatly influence the vulnerability of thin wall buildings subjected to seismic demands consistent with the NSR-10 design earthquake. However, the vulnerability must be contrasted with the hazard to obtain estimates of the annual rate of exceedance of specified EDPs. This section will explore the impact of the WAI and the structural period on the annual rate of RDR and 1^{st}-SDR. **Figure 7.5** presents the RDR and 1^{st}-SDR risk curves for the modified 10-story buildings. To facilitate the interpretation of results, the risk curves of the B0, B1, and B2 models (increasing WAI) are plotted independently from the B1-T model. The risk curves of the latter are contrasted with those obtained for B0 (equal-period structures), and B1 (equal-stiffness structures). The results suggest that decreasing the WAI increases the annual rate of a given RDR. The exception is the B1-T building, which despite having a lower stiffness, has a risk curve of RDR practically identical to that of B0, which matches its fundamental period. At the first-story level, it is observed that decreasing the WAI increases the annual rates for 1^{st}-SDR lower than 0.3% and greater than 1.0%. For the range of 0.3% to 1%, the risk curve is nearly the same for all buildings. When comparing B0 and B1-T, the results show that the risk curve for RDR is the nearly the same for the two buildings. For 1^{st}-SDR, the rates are lower for the B1-T building in the range of 0.2% to 1.0%, while for other 1st-SDR values it closely resembles the B0 curve. The difference between the annual rates of 1^{st}-SDR for B0 and B1-T may be associated to numerical instability in the B0 simulations for displacement demands around the peak pushover strength (see **Figure 7.2**).

Figure 7.6 compares the return periods of different levels of 1^{st}-SDR for the B0, B1, and B2 buildings, organized by increasing WAI. The results show that for 1^{st}-SDR demands in the range of 0.5% to 1.0%, the WAI does not influence significantly the return period of the studied response. For 1^{st}-SDR > 1.0%, the return period of the first-story response consistently increases with an increasing WAI. However, such large levels of 1^{st}-SDR are beyond the experimentally-measured displacement capacity of thin RC walls. An increasing WAI also increases the return period for 1^{st}-SDR demands lower than 0.3%. This is expected as in this range of displacements the analyzed structures are expected to be in the elastic-cracked range of performance, where the displacement response is directly related to the structural period.

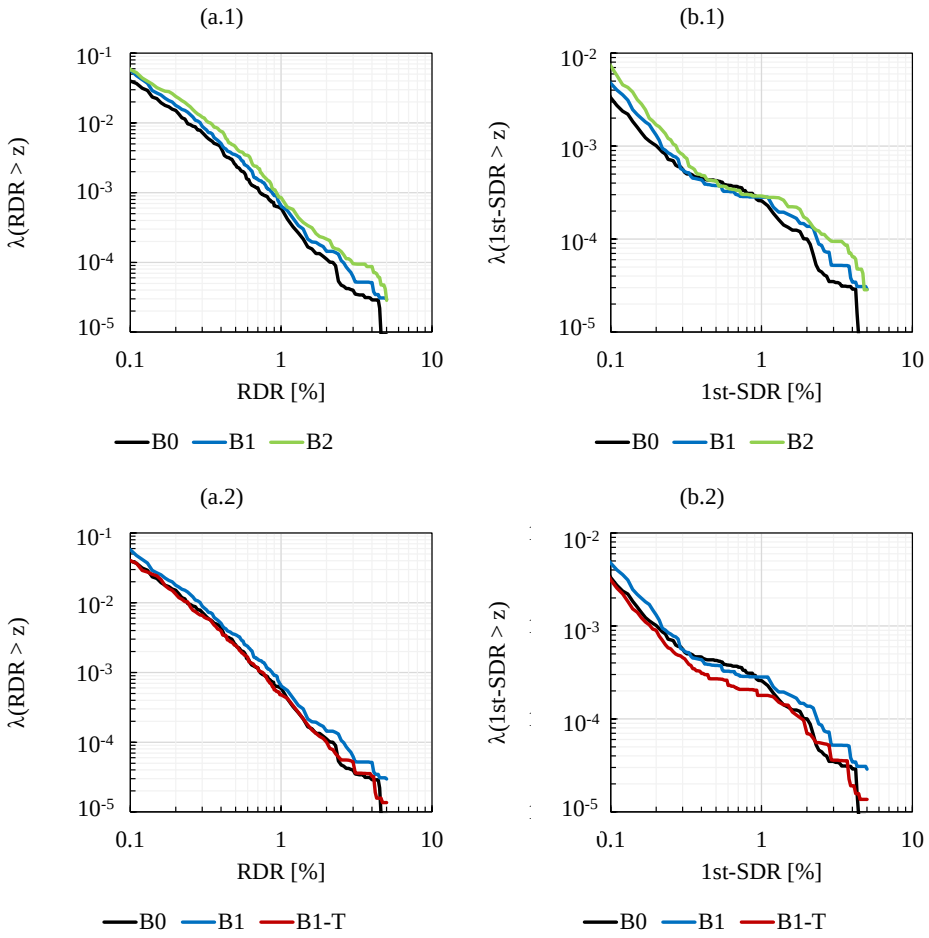

Figure 7.5 – Annual rate of exceedance of the (a) roof drift ratio (RDR) and (b) first-story drift ratio (1st-SDR) in the modified 10-story buildings. Results are grouped by (1) increasing WAI and (2) equal period or structural layout.

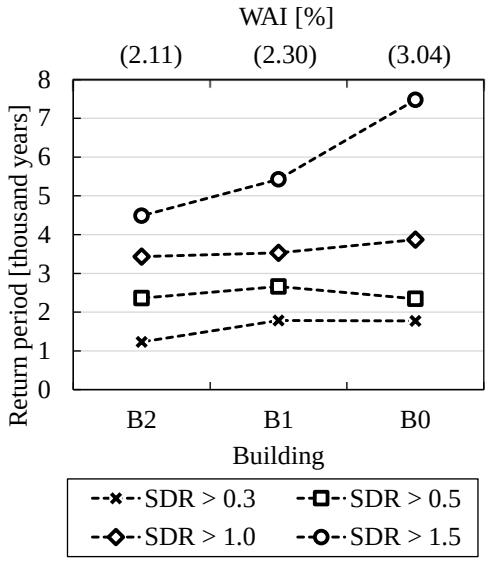

Figure 7.6 – Return period of specific values of first-story drift ratio (1st-SDR) as a function of the WAI.

7.5 Main remarks

In this chapter, the effects of an increasing WAI on the vulnerability and risk of thin wall buildings were studied. It was found that an increasing WAI increases the probability of sustaining large displacements (high 1^{st}-SDR) for fixed values of spectral acceleration $S_a(T_1)$. However, when calculating the annual rate of exceedance of 1^{st}-SDR, the effects of reducing WAI were only evident for very low (1^{st}-SDR < 0.3%) or very large (1^{st}-SDR < 1.0%) displacement demands. For 1^{st}-SDR in the range of 0.3% to 1.0%, the resulting probability of exceedance remained nearly constant for all buildings, with return periods that exceed the 475-year hazard level assigned by the NSR-10 to the design spectrum. A similar study for a group of four 20-story buildings in Chile (Cando et al., 2020) observed that the risk of exceeding displacement demands below the peak pushover strength of the structures increased with a decreasing WAI, but decreased for larger displacements. A plausible explanation for the nearly equal annual rates of exceedance of moderate displacements for buildings of different WAI and structural periods in Colombia is that the NSR-10 design spectrum does not have a natural shape, providing low-WAI, long-period structures with an increased overstrength as compared to shorter-period buildings.

Summary and Conclusion

Industrialized thin RC wall buildings are being built more and more frequently in Colombia and other Northern South American countries. This system allows the constructor engineer to reduce costs in finishes and hasten construction processes compared to traditional systems. The gravity- and lateral force-resisting system of these buildings consists of lightly-reinforced walls with reduced thicknesses. Traditional ductile reinforcement is also typically replaced with cold-drawn wires of limited ductility. The popularity of this construction system has extended to regions of moderate and high seismicity in Colombia. One of the main concerns regarding this construction system is that it has been found experimentally that thin RC walls may have lower-than-expected displacement capacities. Additionally, wall buildings with better structural detailing in Chile and New Zealand exhibited significant damage after the 2010 and 2011 earthquakes. Since the last significantly damaging earthquake in Colombia occurred more than 20 years ago, in 1999, when the building system in question was not popular, it has not been possible to contrast the performance of these buildings with the seismic hazard in the field. This research proposes a hazard-consistent methodology based on nonlinear dynamic analysis to evaluate the vulnerability of thin wall buildings and the risk of exceeding specific engineering demand parameters (EDPs). A case study is presented with geometric features and reinforcement configuration of buildings compatible with the Colombian building typology in high-risk seismic zones. The seismic response of the structures is evaluated in terms of local (at the section level of the elements) and global (general behavior of the structure) deformation capacity and demand in the inelastic range using the proposed methodology. The chapters of this document revolve around the proposed method and the results obtained for the case study.

Chapter 1 described the main characteristics of the thin wall building system as implemented in Colombia based on a recent building inventory carried out in four major cities in Colombia located in moderate- and high-seismicity zones. Among these, the ciy of Armenia is selected as a case study because of its historical seismicity zone, being located only 15 km away from the epicenter of the devastating January 25, 1999 M_w 6.1 Colombia earthquake. Main statistics such as the number of stories, wall dimensions, reinforcement ratios, gravity load demands, and wall area index (WAI) were analyzed to identify a potential building archetype. It was found that the typical wall thickness t_w ranges between 80 and 150 mm, and that the number of stories extends up to 15. Regarding reinforcement, the common practice is to use a single cold-drawn electro-welded wire-mesh layer as longitudinal and transverse reinforcement instead of traditional ductile rebars. With the aim of having a better understanding of the expected behavior of these structures under lateral loads, an experimental database was compiled from three testing campaigns on walls with similar characteristics to the Colombian building typology. It was found that the displacement capacity of the walls is strongly correlated with the aspect ratio of the cross section l_w/t_w and the compression zone c/t_w. An increased in these aspect ratios resulted in a decreasing displacement capacity. In all cases, the characteristics of the Colombian wall archetype typically exceed the geometric limits available in the database, but the trend suggests story drift capacities between 0.5 and 1.0%. This capacity is lower than the 1.43% limit imposed by the local NSR-10 regulation; therefore, these walls do not

meet the performance criteria required by the current Colombian building code. This chapter additionally introduced the current NSR-10 provisions for the design of structural walls, which are based on ACI 318-08, and the implications of applying them to the industrialized wall building system.

In **Chapter 2**, three case-study buildings are selected to investigate the seismic performance of thin RC wall building systems. All the buildings share the same structural plan. The buildings are assumed to be located in the city of Armenia, one of the most seismically active areas in Colombia, as their structural plan is a simplified version of an actual 10-story building in this city. The buildings have fundamental periods in the range 0.2 s $\leq$T $\leq$1.2 s, and WAI between 2.5% and 4.0%. Seismic design forces were estimated using a response spectrum analysis and were scaled to 80% of the base shear obtained using the equivalent lateral force method. The structural walls have thicknesses of 100, 120 and 150 mm for the 5-, 10- and 15-story buildings, respectively. The walls were designed as special structural walls following NSR-10 §C.21, that allows the use of ordinary boundary elements in high-seismicity zones provided that the flexural-compressive demands are low. Two methods are available in NSR-10 to check the need of special boundary elements (SBEs): (i) a force-based method and (ii) a displacement-based method. It was found that for low-rise buildings, where design flexural demands are low, the two methods lead to different conclusions regarding the need of SBEs. This is so because the NSR-10 imposes a limit in the minimum design tip displacement that exceeds the flexural demands imposed by the design seismic forces. Given the reduced thickness of the wall archetypes, the force-based method was used to verify the need of SBEs, following typical engineering practice. The structural walls were provided with minimum reinforcement ratios in the form of a single cold-drawn electro-welded wire-mesh layer and additional boundary reinforcement was added to meet the design flexural demands. These design flexural demands increased with an increasing number of stories, resulting in the 10- and 15-story buildings being provided with increased amounts of boundary reinforcement as compared to the 5-story building.

Chapter 3 reviews the tectonic setting and historical seismicity of the city of Armenia. The earthquakes recorded in the region are the result of the subduction of the oceanic Nazca plate beneath the continental South American plate. Depending on the region where they occur, these earthquakes are classified into three tectonic settings: namely crustal-faulting, intraslab and interface earthquakes. The first two types were found to be the major contributors to the seismic hazard in the region. Next, a seismic model was proposed and calibrated to simulate the seismic hazard at the case-study site. Using this model, a probabilistic seismic hazard analysis (PSHA) was carried out to estimate the expected ground motion intensities at different hazard levels. Lastly, the Conditional Scenario Spectra (CSS) ground-motion selection methodology is extended to consider multiple causal earthquakes. The resulting set of ground motion records have spectral shape and assigned rates of occurrence that reproduce the contributions of the different tectonic settings to the hazard at the site in a wide range of hazard levels. This set is later used to perform intensity-based response history analyses and generate fragility curves of different EDPs. The obtained structural responses are coupled with the assigned rates of occurrence of the ground motions to estimate the seismic annual rate of exceedance of the EDPs of interest. Because these rates also account for the contribution of each of tectonic setting to

the seismic hazard, the annual rates can be deaggregated to determine which types of earthquakes are most likely to generate certain levels of EDP.

In **Chapter 4**, a simple 2D nonlinear model is implemented to evaluate the seismic response of thin wall buildings. The modeling approach uses force-based beam-column (FBC) elements to simulate the flexural response. This element formulation was selected because of its numerical robustness and associated low computational cost. Material constitutive relationships are proposed based on experimental testing. The model is validated using experimental data from four wall specimens with geometric and reinforcement characteristics that resemble the Colombian building typology. The implemented model simulated the lateral force-displacement response of the specimens with an acceptable margin of error and was able to reproduce most of the experimentally-observed modes of failure. The simulated local responses were found to be dependent on the selected integration scheme of the FBC elements. Based on different experimental findings and model calibration, a plastic hinge length in the range $2.0t_w \leq l_p \leq 3.0t_w$ was proposed as the weight of the first integration point. It was found that strain demands in the wall boundaries may be overestimated in tension or underestimated in compression by a factor of 1.5 to 2.0 for high levels of lateral displacement. This is because the formulation of FBC elements assumes plane sections and thus is incapable of reproducing the actual nonlinear strain distribution along the wall section. Future research is also necessary to improve the predicted hysteretic loop shapes and initial stiffness of the walls. However, for this research, the proposed model was able to reproduce the structural demands of interest and was considered suitable for EDP-risk estimation.

The structural response of the building archetypes was evaluated using nonlinear static (pushover) analyses in **Chapter 5**. Seismic performance was evaluated using global- and local-response indicators. The displacement capacity of the system was found to be limited by the tensile strain capacity of the wire-mesh reinforcement. Flanged- and wide-cross-section walls contributed the most to the strength of the system. These walls also exhibited the largest strain demands for any given level of displacement. Two displacement response parameters were initially selected for damage assessment, namely the roof drift ratio (RDR) and the first-story drift ratio (1^{st}-SDR). The 1^{st}-SDR was found to be a better structural damage measure as compared to the RDR because the walls have a single critical section at the base where most of the plasticity is localized. The 1^{st}-SDR associated to different limit states, including the peak pushover strength of the system, was nearly the same for each building archetype. On the other hand, the RDR has an elastic-displacement contribution from the upper stories that results in increased RDR demands for the same 1^{st}-SDR in taller buildings. A similar conclusion applies to the story drift ratios in the upper stories. Instead, the tangent story drift (TDR) as a measure of structural damage. TDR and 1^{st}-SDR are the same in the first story because soil-structure interaction is not simulated. Story drift ratios are an important parameter for non-structural damage assessment, which is out of the scope of this research.

Chapter 6 evaluates the response of the system when subjected to the hazard-consistent CSS ground motion set. The seismic design demands are found to be particularly conservative when compared to a realistic estimation of the hazard for long structural periods. This provides the taller building archetypes with an increased overstrength for a given hazard level. Fragility analysis indicated that an increasing number of stories results

in an increased vulnerability to high ground motion intensities. However, when the structural responses are coupled with the assigned rates of occurrence of the ground motions, it was found that taller buildings do not necessarily have a higher EDP-risk. The estimated annual rates of exceedance were found to be a function of the improved structural detailing in taller buildings and the inherent conservatism of the NSR-10 design demands for long-period structures.

Chapter 7 further explores the impact of the structural period and stiffness of thin wall buildings in the fragility curves and risk estimates. The structural plan of the 10-story building archetype is modified to result in three different versions of the building with different WAI. A decreasing WAI was found to increase the vulnerability of the structures, but this did not translate into increased risk except for very small or very large displacement demands. It was also found that the vulnerability of the structures also depends on the structural period, as two buildings with the same WAI but different structural periods exhibited different fragility curves. Further research is necessary to establish is these findings are specific to the building archetypes studies or if they are indeed a general characteristic of this structural system and the hazard at the site.

References

Abdullah, S. A., & Wallace, J. W. (2019). Drift Capacity of Reinforced Concrete Structural Walls with Special Boundary Elements. *ACI Structural Journal, 116*(1). doi:10.14359/51710864

Abrahamson, N. A., & Al Atik, L. (2010). *Scenario spectra for design ground motions and risk calculation.* Paper presented at the 9th U.S. National and 10th Canadian Conference on Earthquake Engineering, Oakland, CA.

Abrahamson, N. A., Gregor, N., & Addo, K. (2016). BC Hydro Ground Motion Prediction Equations for Subduction Earthquakes. *Earthquake Spectra, 32*(1), 23-44. doi:https://doi.org/10.1193/051712eqs188mr

Abrahamson, N. A., & Yunatci, A. A. (2010). *Ground motion occurrence rates for scenario spectra.* Paper presented at the Fifth International Conferences on Recent Advances in Geotechnical Earthquake Engineering and Soil Dynamics, Rolla, MO.

ACI Committee 318. (2008). Building Code Requirements for Structural Concrete (ACI 318-08) and Commentary. In. Farmington Hills, MI: American Concrete Institute.

ACI Committee 318. (2019). Building code requirements for structural concrete (ACI 318-19) : an ACI standard : commentary on building code requirements for structural concrete (ACI 318R-19), an ACI report. In. Farmington Hills, MI: American Concrete Institute.

Al Atik, L., & Abrahamson, N. A. (2017). Scenario Spectra Program (Version May 2017). Retrieved from https://github.com/abrahamson/css

Alarcon, C., Hube, M. A., & de la Llera, J. C. (2014). Effect of axial loads in the seismic behavior of reinforced concrete walls with unconfined wall boundaries. *Engineering Structures, 73*, 13-23. doi:https://doi.org/10.1016/j.engstruct.2014.04.047

Almeida, J., Prodan, O., Rosso, A., & Beyer, K. (2017). Tests on Thin Reinforced Concrete Walls Subjected to In-Plane and Out-of-Plane Cyclic Loading. *Earthquake Spectra, 33*(1), 323-345. doi:10.1193/101915eqs154dp

Ancheta, T. D., Darragh, R. B., Stewart, J. P., Seyhan, E., Silva, W. J., Chiou, B. S. J., . . . Donahue, J. L. (2014). NGA-West2 Database. *Earthquake Spectra, 30*(3), 989–1005. doi:http://doi.org/10.1193/070913eqs197m

Arcila, M., García, J., Montejo, J., Eraso, J., Valcarcel, J., Mora, M., . . . Díaz, F. (2020). *Modelo nacional de amenaza sísmica para Colombia*. Retrieved from Bogotá:

Arteta, C. A. (2015). *Seismic Response Assessment of Thin Boundary Elements of Special Concrete Shear Walls.* (Ph.D. Dissertation). University of California, Berkeley, Retrieved from https://search.proquest.com/docview/2031098506?accountid=41515 Available from ProQuest Dissertations & Theses A&I database. database.

Arteta, C. A., & Abrahamson, N. A. (2019). Conditional Scenario Spectra (CSS) for Hazard-Consistent Analysis of Engineering Systems. *Earthquake Spectra, 35*(2), 737-757. doi:https://doi.org/10.1193/102116EQS176M

Arteta, C. A., Araújo, G. A., Torregroza, A. M., Martínez, A. F., & Lu, Y. (2019). Hybrid approach for simulating shear–flexure interaction in RC walls with nonlinear truss and fiber models. *Bulletin of Earthquake Engineering*(S.I. : Nonlinear Modelling of Reinforced Concrete Structural Walls). doi:http://doi.org/10.1007/s10518-019-00681-6

Arteta, C. A., Blandón, C. A., Bonett, R., & Carrillo, J. (2018). *Estudio del Comportamiento Sísmico de Edificios de Muros Delgados de Concreto Reforzado*. Retrieved from http://ceer.co/ceer-estudio-de-edificios-de-muros-delgados-con-recomendaciones-enviado/?lang=en

Arteta, C. A., Sánchez, J., Daza, R., Blandón, C. A., Bonett, R. L., Carrillo, J., & Velez, J. C. (2017). *Global and Local Demand Limits of Thin Reinforced Concrete Structural Wall Building Systems.* Paper presented at the 16th World Conference on Earthquake Engineering, 16WCEE 2017, Santiago, Chile.

ASCE 41. (2017). Seismic Evaluation and Retrofit of Existing Buildings (ASCE/SEI 41-17). In. Reston, VA: American Society of Civil Engineers.

Baker, J. W. (2011). Conditional Mean Spectrum: Tool for Ground-Motion Selection. *Journal of Structural Engineering, 137*(3), 322-331. doi:https://doi.org/10.1061/(ASCE)ST.1943-541X.0000215

References

Baker, J. W. (2015). Efficient Analytical Fragility Function Fitting Using Dynamic Structural Analysis. *Earthquake Spectra, 31*(1), 579-599. doi:10.1193/021113eqs025m

Baker, J. W., & Jayaram, N. (2008). Correlation of Spectral Acceleration Values from NGA Ground Motion Models. *Earthquake Spectra, 24*(1), 299–317. doi:https://doi.org/10.1193/1.2857544

Balkaya, C., & Kalkan, E. (2004). Seismic vulnerability, behavior and design of tunnel form building structures. *Engineering Structures, 26*(14), 2081-2099. doi:https://doi.org/10.1016/j.engstruct.2004.07.005

Bazant, Z. P., & Planas, J. (1998). *Fracture and size effect in concrete and other quasibrittle materials*. Boca Raton, FL: CRC Press.

Blandón, C. A., Arteta, C. A., Bonett, R., & Carrillo, J. (2020). *Experiments on non-planar thin and lightly-reinforced concrete walls*. Colombian Earthquake Engineering Research Network.

Blandón, C. A., Arteta, C. A., Bonett, R. L., Carrillo, J., Beyer, K., & Almeida, J. P. (2018). Response of thin lightly-reinforced concrete walls under cyclic loading. *Engineering Structures, 176*, 175-187. doi:http://doi.org/10.1016/j.engstruct.2018.08.089

Blandón, C. A., & Bonett, R. (2019). Thin slender concrete rectangular walls in moderate seismic regions with a single reinforcement layer. *Journal of Building Engineering, In Press*. doi:https://doi.org/10.1016/j.jobe.2019.101035

Bonett, R. (2003). *Vulnerabilidad y riesgo sísmico de edificios. Aplicación a entornos urbanos en zonas de amenaza alta y moderada*. (Ph.D. Doctoral thesis). Universitat Politècnica de Catalunya, Barcelona. Retrieved from https://upcommons.upc.edu/handle/2117/93542

Buniya, M., Simpson, B., Macedo, J., Vergaray, L., & Barbosa, A. R. (2020). *Collapse Fragility Function Development Using Conditional Scenario Spectra: Application to a Multi-story Reinforced Concrete Shear Wall*. Paper presented at the 17th World Conference on Earthquake Engineering, 17WCEE, Sendai, Japan.

Candia, G., Macedo, J., Jaimes, M. A., & Magna-Verdugo, C. (2019). A New State-of-the-Art Platform for Probabilistic and Deterministic Seismic Hazard Assessment. *Seismological Research Letters 90*(6), 2262-2275. doi:https://doi.org/10.1785/0220190025

Cando, M. A., Hube, M. A., Parra, P. F., & Arteta, C. A. (2020). Effect of stiffness on the seismic performance of code-conforming reinforced concrete shear wall buildings. *Engineering Structures, 219*, 110724. doi:https://doi.org/10.1016/j.engstruct.2020.110724

Carrillo, J., & Alcocer, S. M. (2011). Comportamiento a cortante de muros de concreto para vivienda. *Ingeniería Sísmica*(85), 103-126. Retrieved from http://www.scielo.org.mx/scielo.php?script=sci_arttext&pid=S0185-092X2011000200004&lng=es&tlng=es

Carrillo, J., Aperador, W., & Echeverri, F. (2015). Evaluación de los costos de construcción de sistemas estructurales para viviendas de baja altura y de interés social. *Ingeniería, Investigación y Tecnología, 16*(4), 479-490. doi:http://doi.org/10.1016/j.riit.2015.09.001

Carrillo, J., Díaz, C., & Arteta, C. A. (2019). Tensile mechanical properties of the electro-welded wire meshes available in Bogotá, Colombia. *Construction and Building Materials, 195*, 352-362. doi:http://doi.org/10.1016/j.conbuildmat.2018.11.096

CIMOC, & CEDERI. (2002). *Microzonificación Sísmica de la Ciudad de Manizales*. Retrieved from http://idea.manizales.unal.edu.co/gestion_riesgos/descargas/microzon/informe_final.pdf

Coleman, J., & Spacone, E. (2001). Localization Issues in Force-Based Frame Elements. *Journal of Structural Engineering, 127*(11), 1257-1265. doi:http://doi.org/10.1061/(ASCE)0733-9445(2001)127:11(1257)

Comité AIS 100. (2010). Reglamento Colombiano de Construcción Sismo Resistente NSR-10. In. Bogotá, D.C.: Asociación Colombiana de Ingeniería Sísmica–AIS.

Comité AIS 300. (1984). *Estudio General de Amenaza Sísmica de Colombia 1984*. Retrieved from Bogotá, D.C.:

Comité AIS 300. (1996). *Estudio General de Amenaza Sísmica de Colombia 1996*. Retrieved from Bogotá, D.C.:

Comité AIS 300. (2010). *Estudio General de Amenaza Sísmica de Colombia 2009*. Retrieved from Bogotá, D.C.:

Computers and Structures, Inc. (2019). Structural Software for Building Analysis and Design | ETABS (Version 18.0.2).

Cornell, C. A., & Vanmarcke, E. H. (1969). *The major influences on seismic risk.* Paper presented at the Third World Conference on Earthquake Engineering, 3WCEE, Santiago, Chile.

DANE. (2018). *Censo Nacional de Población y Vivienda 2018*. Retrieved from Colombia:

E.030. (2018). Diseño Sismorresistente. In. Lima, Peru: Ministerio de Vivienda, Construcción y Saneamiento.

Elwood, K. J., Pampanin, S., Kam, W. Y., & Priestley, M. J. N. (2014). Performance-Based Issues from the 22 February 2011 Christchurch Earthquake. In M. Fischinger (Ed.), *Performance-Based Seismic Engineering: Vision for an Earthquake Resilient Society* (pp. 159-175). Dordrecht: Springer Netherlands.

FEMA P695. (2009). Quantification of Building Seismic Performance Factors. In. Washington, DC: Federal Emergency Management Agency.

Gogus, A. (2010). *Structural wall systems–Nonlinear modeling and collapse assessment of shear walls and slab-column frames.* (Ph.D. Dissertation). University of California, Los Angeles,

Gogus, A., & Wallace, J. W. (2015). Seismic Safety Evaluation of Reinforced Concrete Walls through FEMA P695 Methodology. *Journal of Structural Engineering, 141*(10). doi:https://doi.org/10.1061/(ASCE)ST.1943-541X.0001221

Gonzales, H., & Lopez-Almansa, F. (2010). Seismic performance of buildings with thin RC bearing walls. *Engineering Structures, 34*, 244-258. doi:https://doi.org/10.1016/j.engstruct.2011.10.007

Guttenberg, B., & Richter, C. F. (1944). Frequency of earthquakes in California. *Bulletin of the Seismological Society of America, 34*(4), 185-188.

Hoult, R., Goldsworthy, H., & Lumantarna, E. (2019). Fragility Functions for RC Shear Wall Buildings in Australia. *Earthquake Spectra, 35*(1), 333-360. doi:10.1193/120717eqs251m

Hsu, T. T. C. (1993). *Unified Theory of Reinforced Concrete*. Boca Raton, FL: CRC Press.

Hube, M. A., Marihuén, A., de la Llera, J. C., & Stojadinovic, B. (2014). Seismic behavior of slender reinforced concrete walls. *Engineering Structures, 80*, 377-388. doi:http://doi.org/10.1016/j.engstruct.2014.09.014

Jayaram, N., Lin, T., & Baker, J. W. (2011). A Computationally Efficient Ground-Motion Selection Algorithm for Matching a Target Response Spectrum Mean and Variance. *Earthquake Spectra, 27*(3), 797-815. doi:https://doi.org/10.1193/1.3608002

Jiang, H., & Kurama, Y. C. (2010). Analytical Modeling of Medium-Rise Reinforced Concrete Shear Walls. *Structural Journal, 107*(4), 400-410. doi:http://doi.org/10.14359/51663812

Jünemann, R., de la Llera, J. C., Hube, M. A., Cifuentes, L. A., & Kausel, E. (2015). A statistical analysis of reinforced concrete wall buildings damaged during the 2010, Chile earthquake. *Engineering Structures, 82*, 168-185. doi:http://doi.org/10.1016/j.engstruct.2014.10.014

Kalkan, E., & Yüksel, S. B. (2008). Pros and cons of multistory RC tunnel-form (box-type) buildings. *The Structural Design of Tall and Special Buildings, 17*(3), 601-617. doi:https://doi.org/10.1002/tal.368

Kellogg, J. N., & Vega, V. (1995). Tectonic development of Panama, Costa Rica, and the Colombian Andes: Constraints from Global Positioning System geodetic studies and gravity. In P. Mann (Ed.), *Geologic and Tectonic Development of the Caribbean Plate Boundary in Southern Central America* (Vol. Special Paper 295, pp. 75-90). Boulder, Colorado: Geological Society of America

Kent, D. C., & Park, R. (1971). Flexural members with confined concrete. *Journal of the Structural Division, 97*(3), 1969-1990.

Kircher, C., Deierlein, G., Hooper, J., Krawinkler, H., Mahin, S., Shing, B., & Wallace, J. W. (2010). *Evaluation of the FEMA P-695 Methodology for Quantification of Building Seismic Performance Factors | NIST GCR 10-917-8*. Retrieved from https://www.nist.gov/publications/

Kishida, T., Darragh, R. B., Chiou, B. S. J., Bozorgnia, Y., Mazzoni, S., Contreras, V., . . . Stewart, J. P. (2020). Chapter 3: Ground Motions and Intensity Measures. In J. P. Stewart (Ed.), *Data Resources for NGA-Subduction Project, PEER Report 2020/02*. Berkeley, CA: Pacific Earthquake Engineering Research Center.

Kolozvari, K., Arteta, C., Fischinger, M., Gavridou, S., Hube, M. A., Isakovic, T., . . . Wallace, J. W. (2018). Comparative Study of State-of-the-Art Macroscopic Models for Planar Reinforced Concrete Walls. *ACI Structural Journal, 115*(6). doi:10.14359/51710835

Kolozvari, K., Orakcal, K., & Wallace, J. W. (2015a). Modeling of Cyclic Shear-Flexure Interaction in Reinforced Concrete Structural Walls. I: Theory. *Journal of Structural Engineering, 141*(5). doi:https://doi.org/10.1061/(ASCE)ST.1943-541X.0001059

Kolozvari, K., Orakcal, K., & Wallace, J. W. (2015b). *Shear-Flexure Interaction Modeling of reinforced Concrete Structural Walls and Columns under Reversed Cyclic Loading | PEER Report No. 2015/12*. Retrieved from https://peer.berkeley.edu/peer-reports

Kolozvari, K., & Wallace, J. W. (2016). Practical Nonlinear Modeling of Reinforced Concrete Structural Walls. *Journal of Structural Engineering, 142*(12). doi:http://doi.org/10.1061/(ASCE)ST.1943-541X.0001492

Lagos, R., Kupfer, M., Lindenberg, J., Bonelli, P., Saragoni, R., Guendelman, T., . . . Yañez, F. (2012). Seismic Performance of High-rise Concrete Buildings in Chile. *International Journal of High-Rise Buildings, 1*(3), 181-194.

Lee, J., & Lopez, M. M. (2014). An Experimental Study on Fracture Energy of Plain Concrete. *International Journal of Concrete Structures and Materials, 8*(2), 129-139. doi:https://doi.org/10.1007/s40069-014-0068-1

Lin, T., Haselton, C. B., & Baker, J. W. (2013). Conditional spectrum-based ground motion selection. Part I: Hazard consistency for risk-based assessments. *Earthquake Engineering & Structural Dynamics, 42*(12), 1847-1865. doi:https://doi.org/10.1002/eqe.2301

Lu, Y., Henry, R. S., Gultom, R., & Ma, Q. T. (2017). Cyclic Testing of Reinforced Concrete Walls with Distributed Minimum Vertical Reinforcement. *Journal of Structural Engineering, 143*(5), 04016225. doi:doi:10.1061/(ASCE)ST.1943-541X.0001723

Lu, Y., & Panagiotou, M. (2014). Three-Dimensional Cyclic Beam-Truss Model for Nonplanar Reinforced Concrete Walls. *Journal of Structural Engineering, 140*(3), 04013071. doi:http://doi.org/10.1061/(ASCE)ST.1943-541X.0000852

Mattock, A. H. (1965). Rotational Capacity of Hinging Regions in Reinforced Concrete Beams. *ACI Symposium Publication*.

McKenna, F., Scott, M. H., & Fenves, G. L. (2010). Nonlinear Finite-Element Analysis Software Architecture Using Object Composition. *Journal of Computing in Civil Engineering, 24*(1), 95-107. doi:doi:10.1061/(ASCE)CP.1943-5487.0000002

Mejia, L. G., Ortiz R., J. C., & Osorio G., L. I. (2004). RC Structural Wall Building | Report 109. In *World Housing Encyclopedia (www.world-housing.net)*. Colombia: Earthquake Engineering Research Institute, International Association for Earthquake Engineering.

Menegotto, M., & Pinto, E. (1973). *Method of analysis for cyclically loaded reinforced concrete plane frames including changes in geometry and non-elastic behavior of elements under combined normal force and bending.* Paper presented at the IABSE Symp. on Resistance and Ultimate Deformability of Structures Acted on by Well-Defined Repeated Loads, Lisbon, Portugal.

Mohammed, M. A., & Barbosa, A. R. (2019). Numerical Modeling Strategy for the Simulation of Nonlinear Response of Slender Reinforced Concrete Structural Walls. *Computer Modeling in Engineering & Sciences, 120*(3), 583-627. doi:http:/doi.org/10.32604/cmes.2019.06052

Mohd Yassin, M. H. (1994). *Nonlinear analysis of prestressed concrete structures under monotonic and cyclic loads.* University Microfilms International, Ann Arbor.

Montalva, G. A., Bastías, N., & Rodriguez-Marek, A. (2017). Ground-Motion Prediction Equation for the Chilean Subduction Zone. *Bulletin of the Seismological Society of America, 107*(2), 901-911. doi:10.1785/0120160221

Nakamura, H., & Higai, T. (2001). Compressive Fracture Energy and Fracture Zone Length of Concrete. In *Modeling of Inelastic Behavior of RC Structures Under Seismic Loads* (pp. 471-487). Reston, VA: American Society of Civil Engineers.

Orakcal, K., & Wallace, J. W. (2006). Flexural Modeling of Reinforced Concrete Walls-Experimental Verification. *ACI Structural Journal, 103*(2), 196-206.

Pacific Earthquake Engineering Research Center. (2017). Guidelines for Performance-Based Seismic Design of Tall Buildings. In.

Pacific Earthquake Engineering Research Center, & Applied Technology Council. (2010). *Modeling and acceptance criteria for seismic design and analysis of tall buildings | PEER/ATC 72-1*. Retrieved from Richmond, CA: https://peer.berkeley.edu/sites/default/files/peer-atc-72-1_report.pdf

Park, R., & Paulay, T. (1975). *Reinforced Concrete Structures*. Canada: John Wiley & Sons, Inc.

Parra, P. F., Arteta, C. A., & Moehle, J. P. (2019). Modeling criteria of older non-ductile concrete frame–wall buildings | SpringerLink. *Bulletin of Earthquake Engineering*(S.I.: Nonlinear Modelling of Reinforced Concrete Structural Walls). doi:http://doi.org/10.1007/s10518-019-00697-y

References

Paulay, T., & Priestley, M. J. N. (1992). *Seismic Design of Reinforced Concrete and Masonry Buildings*. United States: John Wiley and Sons, Inc.

Petrangeli, M., Pinto, P. E., & Ciampi, V. (1999). Fiber Element for Cyclic Bending and Shear of RC Structures. I: Theory *Journal of Engineering Mechanics, 125*(9), 1002-1009. doi:https://doi.org/10.1061/(ASCE)0733-9399(1999)125:9(994)

Priestley, M. J. N., Seible, F., & Calvi, G. M. (1996). *Seismic Design and Retrofit of Bridges*: John Wiley & Sons, Inc.

Pugh, J. S., Lowes, L. N., & Lehman, D. E. (2015). Nonlinear line-element modeling of flexural reinforced concrete walls. *Engineering Structures, 104*, 174-192. doi:https://doi.org/10.1016/j.engstruct.2015.08.037

Quiroz, L. G., Maruyama, Y., & Zavala, C. (2013). Cyclic behavior of thin RC Peruvian shear walls: Full-scale experimental investigation and numerical simulation. *Engineering Structures, 52*, 153-167. doi:https://doi.org/10.1016/j.engstruct.2013.02.033

Restrepo, J. I., & Cowan, H. A. (2000). The "Eje Cafetero" earthquake, Colombia of January 25, 1999. *Bulletin of the New Zealand Society for Earthquake Engineering, 33*(1). doi:10.5459/bnzsee.33.1.1-29

Riva, P., & Franchi, A. (2001). Behavior of reinforced concrete walls with welded wire mesh subjected to cyclic loading. *Structural Journal, 98*(3), 324-334.

Rosso, A., Almeida, J. P., & Beyer, K. (2016). Stability of thin reinforced concrete walls under cyclic loads: state-of-the-art and new experimental findings. *Bulletin of Earthquake Engineering, 14*(2), 455-484. doi:https://doi.org/10.1007/s10518-015-9827-x

Sadigh, K., Chang, C.-Y., Egan, J. A., Makdisi, F., & Youngs, R. R. (1997). Attenuation relationships for shallow crustal earthquakes based on California strong motion data. *Seismological Research Letters, 68*(1), 180-189. doi:https://doi.org/10.1785/gssrl.68.1.180

Salgado-Gálvez, M. A., Bernal, G. A., & Cardona, O. D. (2016). Evaluación probabilista de la amenaza sísmica de Colombia con fines de actualización de la Norma Colombiana de Diseño de Puentes CCP-14. *Revista Internacional de Métodos Numéricos para Cálculo y Diseño en Ingeniería, 32*(4), 230-239. doi:https://doi.org/10.1016/j.rimni.2015.07.001

Sánchez, J. (2019). *Caracterización estadística de muros delgados de concreto reforzado para zonas de amenaza sísmica alta.* (Master Thesis). Universidad del Norte, Barranquilla.

Sánchez, J., & Arteta, C. A. (2017, 2017). *Caracterización estadística de edificios de muros delgados en concreto reforzado para zonas de amenaza sísmica alta.* Paper presented at the VIII Congreso Nacional de Ingeniería Sísmica, Barranquilla, Colombia.

Scott, B. D., Park, R., & Priestley, M. J. N. (1982). Stress-Strain Behavior of Concrete Confined by Overlapping Hoops at Low and High Strain Rates. *Journal Proceedings, 79*(1), 13-27. doi:https://doi.org/10.14359/10875

Segura, C. L., & Wallace, J. W. (2018a). Impact of Geometry and Detailing on Drift Capacity of Slender Walls. *ACI Structural Journal, 115*(3), 885-895. doi:http://doi.org/10.14359/51702046

Segura, C. L., & Wallace, J. W. (2018b). Seismic Performance Limitations and Detailing of Slender Reinforced Concrete Walls. *ACI Structural Journal, 115*(3), 849-859. doi:http://doi.org/10.14359/51701918

Servicio Geológico Colombiano. (2017). *Sismicidad Histórica de Colombia*. Retrieved from: http://sish.sgc.gov.co/visor/

Servicio Geológico Colombiano. (2018). *Mapa Geológico de Colombia - Fallas*. Retrieved from: https://datos.sgc.gov.co/datasets/c05c6dbf27f645eb883bae3a9cd0d08f?layer=1

Servicio Geológico Colombiano. (2020). Sistema de Consulta de la Amenaza Sísmica de Colombia. Retrieved from https://amenazasismica.sgc.gov.co/

Spacone, E., Filippou, F. C., & Taucer, F. F. (1996). Fibre Beam–Column Model for Non-Linear Analysis of R/C Frames: Part I. Formulation. *Earthquake Engineering & Structural Dynamics, 25*(7), 711-725. doi:https://doi.org/10.1002/(SICI)1096-9845(199607)25:7<711::AID-EQE576>3.0.CO;2-9

Takahashi, S., Yoshida, K., Ichinose, T., Sanada, Y., Matsumoto, K., Fukuyama, H., & Suwada, H. (2013). Flexural Drift Capacity of Reinforced Concrete Wall with Limited Confinement. *ACI Structural Journal, 110*(1), 95-104.

Thomsen, J. H., & Wallace, J. W. (2004). Displacement-Based Design of Slender Reinforced Concrete Structural Walls - Experimental Verification. *Journal of Structural Engineering, 130*(4), 618-630. doi:https://doi.org/10.1061/(ASCE)0733-9445(2004)130:4(618)

Tran, T. A. (2012). *Experimental and Analytical Studies of Moderate Aspect Ratio Reinforced Concrete Structural Walls.* (Ph.D. Dissertation). University of California, Los Angeles,

Ugalde, D., & Lopez-Garcia, D. (2017). *Elastic Overstrength of Reinforced Concrete Shear Wall Buildings in Chile*. Paper presented at the 16th World Conference on Earthquake Engineering, 16WCEE 2017, Santiago, Chile. https://www.wcee.nicee.org/wcee/article/16WCEE/WCEE2017-4560.pdf

Ugalde, D., Parra, P. F., & Lopez-Garcia, D. (2019). Assessment of the seismic capacity of tall wall buildings using nonlinear finite element modeling. *Bulletin of Earthquake Engineering*(S.I. : Nonlinear Modelling of Reinforced Concrete Structural Walls). doi:https://doi.org/10.1007/s10518-019-00644-x

Vamvatsikos, D., & Cornell, C. A. (2001). Incremental dynamic analysis. *Earthquake Engineering & Structural Dynamics, 31*(3), 491–514. doi:https://doi.org/10.1002/eqe.141

Vásquez, J. A., de la Llera, J. C., & Hube, M. A. (2016). A regularized fiber element model for reinforced concrete shear walls. *Earthquake Engineering & Structural Dynamics, 45*(13), 2063-2083. doi:https://doi.org/10.1002/eqe.2731

Vecchio, F. J., & Collins, M. P. (1986). The Modified Compression-Field Theory for Reinforced Concrete Elements Subjected to Shear. *Journal of the American Concrete Institute, 83*, 219-231.

Velandia, F., Acosta, J., Terraza, R., & Villegas, H. (2005). The current tectonic motion of the Northern Andes along the Algeciras Fault System in SW Colombia. *Tectonophysics, 399*(1), 313-329. doi:https://doi.org/10.1016/j.tecto.2004.12.028

Wallace, J. W. (1994). New Methodology for Seismic Design of RC Shear Walls. *Journal of Structural Engineering, 120*(3), 863-884. doi:doi:10.1061/(ASCE)0733-9445(1994)120:3(863)

Wallace, J. W. (2011). *February 27, 2010 Chile Earthquake: Preliminary Observations on Structural Performance and Implications for U.S. Building Codes.* Paper presented at the ASCE Structures Congress, Las Vegas.

Wallace, J. W. (2012). Behavior, design, and modeling of structural walls and coupling beams — Lessons from recent laboratory tests and earthquakes. *International Journal of Concrete Structures and Materials, 6*(1), 3-18. doi:http://doi.org/10.1007/s40069-012-0001-4

Wang, Z. (2009). Seismic Hazard vs. Seismic Risk. *Seismological Research Letters, 80*(5), 673–674. doi:https://doi.org/10.1785/gssrl.80.5.673

Welt, T. (2015). *Detailing for Compression in Reinforced Concrete Wall Boundary Elements: Experiments, Simulations, and Design Recom-mendations.* (Ph.D. Dissertation). University of Illinois, Urbana-Champaign,

Wittmann, F. H., Rokugo, K., Brühwiler, E., Mihashi, H., & Simonin, P. (1988). Fracture energy and strain softening of concrete as determined by means of compact tension specimens. *Materials and Structures, 21*(1), 21-32. doi:http://doi.org/10.1007/bf02472525

Wood, S. L. (1991). Performance of Reinforced Concrete Buildings during the 1985 Chile Earthquake: Implications for the Design of Structural Walls. *Earthquake Spectra, 7*(4), 607-638. doi:10.1193/1.1585645

Yañez, D. A. (2006). *Análisis de Respuesta Sísmica en Edificios Tipo Túnel Bajo Régimen Elástico.* (Civil Engineering Bachelor). Universidad de Los Andes, Mérida, Venezuela.

Zhao, J. X., Zhang, J., Asano, A., Ohno, Y., Oouchi, T., Takahashi, T., . . . Fukushima, Y. (2006). Attenuation Relations of Strong Ground Motion in Japan Using Site Classification Based on Predominant Period. *Bulletin of the Seismological Society of America, 96*(3), 898-913. doi:https://doi.org/10.1785/0120050122

Appendix A – Seismic Hazard Model

A.1 *SeismicHazard* Input File

```
Option 0 - Global Parameters
Projection   : WGS84
Image        : colombia.mat
Boundary     : COL_adm1.shp
Layer        :
ShearModulus : 3e11      #dyne/cm2
IM           : PGA Sa(0.001) Sa(0.01) Sa(0.02) Sa(0.03) Sa(0.04) Sa(0.05) Sa(0.075) Sa(0.1)
Sa(0.15) Sa(0.20) Sa(0.25) Sa(0.30) Sa(0.40) Sa(0.50) Sa(0.75) Sa(1.00) Sa(1.50) Sa(2.00)
Sa(3.00) Sa(4.00) Sa(5.00) Sa(7.50) Sa(10.0)
im           : logsp(0.001,10,100)
MaxDistance  : 1000
MagDiscrete  : gauss 10
CGMM         : shuffle MC 500
IM1          : 0.01
IM2          : 0.1 0.2 0.5 1 2
Spatial      : @none_spatial
Spectral     : @none_spectral
LiteMode     : off
Clusters     : off 100 1

Option 1 - Logic Tree Weights
Geom Weight : 1
Gmpe Weight : 1
Mscl Weight : 1

Option 2 - Source Geometry #37 of 38 seismic source
geometry 1 Jaimes&Candia, 2019
COLsp_2BIntermediaII        type area mechanism intraslab  gmpe 3 vertices  6.50000 -76.9000
-40.0000  4.50000 -76.9000 -40.0000  4.50000 -75.0000 -120.000  6.50000 -75.0000 -120.000
COLc7CaucaModifi             type area mechanism crustal  gmpe 1 vertices  5.85000 -75.8000
-5.00000  5.20000 -75.9000 -5.00000  4.62100 -76.1200 -5.00000  3.91000 -76.3800 -5.00000
3.18800 -76.643 -5.000  2.48000 -76.900 -5.000  1.50600 -77.5030 -5.000  1.50400 -77.4430 -
40.00  2.48000 -76.8500 -40.00  3.17900 -76.600 -40.00  3.8680 -76.350 -40.00  4.6070 -76.073
-40.00  5.2000 -75.850 -40.00  5.8500 -75.750 -40.00
Colc27RomeralModifi          type area mechanism crustal  gmpe 1 vertices  6.88000 -75.8000
-5.00000  6.10000 -75.7000 -5.00000  5.55000 -75.5000 -5.00000  5.00000 -75.7000 -5.00000
4.32000 -75.680 -5.000  3.60000 -76.150 -5.000  2.63400 -76.5630 -5.000  1.88000 -76.8870 -
5.000  1.50400 -77.0500 -5.000  1.50400 -77.007 -42.00  1.8760 -76.832 -42.00  2.6420 -76.500
-42.00  3.6000 -76.100 -42.00  4.3200 -75.630 -42.00  5.0000 -75.650 -42.00  5.5500 -75.450
-42.00  6.1000 -75.650 -42.00  6.880 -75.750 -42.00
COLsi2SubCentroModifi       type area mechanism interface  gmpe 2 vertices  6.53000 -78.2580
-5.00000  4.50000 -78.2580 -5.00000  4.50000 -76.9000 -40.0000  6.53000 -76.9000 -40.0000
COLsi3SubSurModifi           type area mechanism interface  gmpe 2 vertices  0.5071 -79.4923
-5  0.5071 -77.9052 -40  2.4938 -77.9052 -40  4.489 -76.9038 -40  4.489 -78.5098 -5  2.4938
-79.4923 -5 #

Option 3 - GMPE Library
at01 handle I_2014_nga mechanism strike-slip
at02 handle ASK_2014_nga  mechanism strike-slip event mainshock Z10 unk Vs30type inferred
region global
at03 handle Zhao2006 mechanism intraslab
at04 handle Zhao2006 mechanism interface
at05 handle MontalvaBastias2017 mechanism intraslab region forearc
at06 handle MontalvaBastias2017 mechanism interface region forearc
at07 handle BCHydro2012 mechanism intraslab region Forearc DeltaC1 Central
at08 handle BCHydro2012 mechanism interface region Forearc DeltaC1 Central
at09 handle Arteta2018 media rock region forearc
at10 handle Arteta2018 media soil region forearc
at11 handle Sadigh1997 mechanism strike-slip media rock
```

```
    at12 handle Sadigh1997 mechanism strike-slip media deepsoil
    at13 handle CB_2014_nga mechanism strike-slip HW include Z25 999 region global

    Option 4 - GMPE GROUPS
    GMPE1     pointers 12 6 3

    Option 5 - MAGNITUDE SCALING RELATIONS
    seismicity 1 Criterio III
    COLsp_2BIntermediaII            handle truncexp NMmin 0.1224  bvalue  0.768  Mmin 6.0 Mmax
    7.0  # beta 1.768
    COLc7CaucaModifi                handle truncexp NMmin 0.1057  bvalue  0.605  Mmin 5.0 Mmax
    7.0  # beta 1.393
    Colc27RomeralModifi             handle truncexp NMmin 0.1057  bvalue  0.605  Mmin 5.0 Mmax
    7.0  # beta 1.393
    COLsi2SubCentroModifi           handle truncexp NMmin 0.0601  bvalue  0.689  Mmin 6.0 Mmax
    9.0  # beta 1.586
    COLsi3SubSurModifi              handle truncexp NMmin 0.0601  bvalue  0.636  Mmin 6.0 Mmax
    9.0  # beta 1.586

    Option 6 - RUPTURE AREA
    COLsp_2BIntermediaII          type circular spacing 30 RA custom 1 4 0 taper false
    COLc7CaucaModifi              type circular spacing 30 RA custom 1 4 0 taper false
    Colc27RomeralModifi           type circular spacing 10 RA custom 1 4 0 taper false
    COLsi2SubCentroModifi         type circular spacing 30 RA custom 1 4 0 taper false
    COLsi3SubSurModifi            type circular spacing 30 RA custom 1 4 0 taper false

    Option 7 - Pre defined sites
    source 300

Armenia       4.5339   -75.6811 1483 Vs30 300.0000
```

Appendix B - Conditional Scenario Spectra Metadata

B.1 CSS Metadata

Metadata related to the selected 348 ground motions used for the construction of the CSS corresponding to each scenario discussed in **Chapter 3** is present in **Table B.1.1** to **Table B.1.3**.

Table B.1.1 – Metadata of Conditional Scenario Spectra set for crustal earthquakes.

HazLevel	Index	RSN	EqID	Mag	Rrup	Vs30	Scale Factor	Rate
1	1	184	50	6.5	5.1	202.3	0.05	1.25E-03
	2	544	102	5.8	23.5	271.4	0.25	5.55E-04
	3	161	50	6.5	10.4	208.7	0.13	6.30E-04
	4	312	71	5.9	24.9	274.5	0.29	9.25E-04
	5	158	50	6.5	0.3	274.5	0.09	1.76E-03
	6	174	50	6.5	12.4	196.3	0.08	3.99E-04
	7	127	42	5.5	12	338.6	0.80	5.58E-03
	8	553	103	6.2	21.1	345.4	0.56	6.79E-05
	9	554	103	6.2	21.1	345.4	0.47	6.30E-03
	10	314	73	5.9	15.4	208.7	0.30	5.01E-04
	11	545	102	5.8	15.1	345.4	0.77	1.06E-03
	12	456	90	6.2	13.7	270.8	0.36	1.43E-05
	13	97	33	5.7	17.7	297.9	0.37	9.53E-04
	14	995	127	6.7	24	316.5	0.13	1.07E-03
2	15	158	50	6.5	0.3	274.5	0.19	4.95E-04
	16	127	42	5.5	12	338.6	1.67	5.98E-03
	17	638	113	6	21.1	315.1	0.46	1.11E-04
	18	149	48	5.7	5.7	221.8	0.23	8.25E-04
	19	554	103	6.2	21.1	345.4	1.00	3.64E-04
	20	806	118	6.9	24.2	267.7	0.31	4.07E-04
	21	545	102	5.8	15.1	345.4	1.63	1.67E-04
	22	1048	127	6.7	12.1	280.9	0.14	1.15E-04
	23	456	90	6.2	13.7	270.8	0.77	8.52E-05
	24	68	30	6.6	22.8	316.5	0.53	2.64E-04
	25	97	33	5.7	17.7	297.9	0.79	1.20E-04
	26	169	50	6.5	22	274.5	0.26	2.02E-04
3	27	184	50	6.5	5.1	202.3	0.22	6.89E-06
	28	161	50	6.5	10.4	208.7	0.54	3.49E-04
	29	312	71	5.9	24.9	274.5	1.21	1.54E-04
	30	158	50	6.5	0.3	274.5	0.38	3.14E-04
	31	127	42	5.5	12	338.6	3.15	7.32E-04
	32	553	103	6.2	21.1	345.4	2.19	3.64E-05
	33	149	48	5.7	5.7	221.8	0.42	1.97E-04
	34	554	103	6.2	21.1	345.4	1.78	2.84E-05
	35	806	118	6.9	24.2	267.7	0.54	1.93E-04
	36	545	102	5.8	15.1	345.4	2.80	3.70E-05
	37	1048	127	6.7	12.1	280.9	0.23	1.01E-04
	38	456	90	6.2	13.7	270.8	1.27	8.70E-05
	39	269	64	6.3	7.3	274.5	2.98	1.78E-05
	40	68	30	6.6	22.8	316.5	0.86	2.05E-05

HazLevel	Index	RSN	EqID	Mag	Rrup	Vs30	Scale Factor	Rate
4	41	161	50	6.5	10.4	208.7	0.82	1.89E-04
	42	312	71	5.9	24.9	274.5	1.85	2.37E-05
	43	158	50	6.5	0.3	274.5	0.58	1.78E-04
	44	167	50	6.5	15.3	274.5	1.24	1.25E-05
	45	730	117	6.8	24	274.5	0.81	1.31E-04
	46	127	42	5.5	12	338.6	4.78	1.66E-04
	47	553	103	6.2	21.1	345.4	3.31	1.40E-05
	48	149	48	5.7	5.7	221.8	0.64	2.01E-04
	49	554	103	6.2	21.1	345.4	2.68	2.37E-05
	50	806	118	6.9	24.2	267.7	0.81	7.48E-05
	51	545	102	5.8	15.1	345.4	4.18	3.15E-05
	52	754	118	6.9	20.8	295	0.96	4.27E-06
	53	1048	127	6.7	12.1	280.9	0.34	1.75E-07
	54	456	90	6.2	13.7	270.8	1.90	4.51E-05
	55	269	64	6.3	7.3	274.5	4.43	4.92E-05
	56	68	30	6.6	22.8	316.5	1.27	5.71E-05
	57	97	33	5.7	17.7	297.9	1.86	3.57E-06
5	58	544	102	5.8	23.5	271.4	2.50	1.07E-05
	59	161	50	6.5	10.4	208.7	1.22	5.68E-05
	60	312	71	5.9	24.9	274.5	2.77	2.05E-06
	61	158	50	6.5	0.3	274.5	0.87	4.12E-05
	62	167	50	6.5	15.3	274.5	1.88	1.56E-05
	63	730	117	6.8	24	274.5	1.22	6.85E-05
	64	127	42	5.5	12	338.6	7.25	1.28E-04
	65	553	103	6.2	21.1	345.4	5.03	7.21E-06
	66	149	48	5.7	5.7	221.8	0.98	1.30E-04
	67	806	118	6.9	24.2	267.7	1.25	6.01E-05
	68	545	102	5.8	15.1	345.4	6.48	4.92E-06
	69	754	118	6.9	20.8	295	1.49	1.75E-07
	70	456	90	6.2	13.7	270.8	2.96	8.32E-06
	71	269	64	6.3	7.3	274.5	6.94	2.36E-05
	72	68	30	6.6	22.8	316.5	1.99	6.85E-07
	73	97	33	5.7	17.7	297.9	2.92	2.02E-05
6	74	184	50	6.5	5.1	202.3	0.77	5.54E-06
	75	161	50	6.5	10.4	208.7	1.89	3.12E-05
	76	312	71	5.9	24.9	274.5	4.25	1.38E-05
	77	158	50	6.5	0.3	274.5	1.33	1.89E-05
	78	730	117	6.8	24	274.5	1.83	3.19E-05
	79	127	42	5.5	12	338.6	10.80	3.99E-05
	80	553	103	6.2	21.1	345.4	7.44	1.13E-05
	81	149	48	5.7	5.7	221.8	1.43	2.01E-05
	82	806	118	6.9	24.2	267.7	1.81	9.04E-06
	83	545	102	5.8	15.1	345.4	9.23	1.56E-06
	84	456	90	6.2	13.7	270.8	4.14	8.85E-07
	85	269	64	6.3	7.3	274.5	9.65	2.45E-05
	86	97	33	5.7	17.7	297.9	4.01	1.12E-05
	87	169	50	6.5	22	274.5	1.30	7.61E-06
7	88	161	50	6.5	10.4	208.7	2.55	1.52E-05
	89	158	50	6.5	0.3	274.5	1.78	2.81E-06
	90	730	117	6.8	24	274.5	2.45	2.61E-05
	91	127	42	5.5	12	338.6	14.44	1.62E-05
	92	553	103	6.2	21.1	345.4	9.94	6.49E-06
	93	806	118	6.9	24.2	267.7	2.40	1.02E-07
	94	269	64	6.3	7.3	274.5	12.69	8.73E-06

HazLevel	Index	RSN	EqID	Mag	Rrup	Vs30	Scale Factor	Rate
	95	97	33	5.7	17.7	297.9	5.26	2.24E-05
	96	169	50	6.5	22	274.5	1.71	2.34E-06
8	97	544	102	5.8	23.5	271.4	6.91	6.22E-07
	98	161	50	6.5	10.4	208.7	3.36	3.12E-06
	99	158	50	6.5	0.3	274.5	2.35	1.79E-06
	100	730	117	6.8	24	274.5	3.25	1.50E-05
	101	127	42	5.5	12	338.6	19.18	5.18E-06
	102	553	103	6.2	21.1	345.4	13.22	2.46E-06
	103	806	118	6.9	24.2	267.7	3.21	3.38E-06
	104	314	73	5.9	15.4	208.7	6.54	2.98E-06
	105	545	102	5.8	15.1	345.4	16.42	2.36E-06
	106	456	90	6.2	13.7	270.8	7.36	4.85E-06
	107	269	64	6.3	7.3	274.5	17.17	6.43E-06
	108	97	33	5.7	17.7	297.9	7.14	6.87E-06
9	109	161	50	6.5	10.4	208.7	4.49	3.50E-06
	110	730	117	6.8	24	274.5	4.25	5.49E-06
	111	314	73	5.9	15.4	208.7	8.31	1.09E-08
	112	545	102	5.8	15.1	345.4	20.76	4.41E-06
	113	269	64	6.3	7.3	274.5	21.34	3.99E-07
	114	97	33	5.7	17.7	297.9	8.80	5.05E-06
10	115	174	50	6.5	12.4	196.3	3.15	1.23E-06
	116	730	117	6.8	24	274.5	5.16	1.38E-07
	117	127	42	5.5	12	338.6	30.36	2.95E-06
	118	806	118	6.9	24.2	267.7	4.96	8.32E-07
	119	314	73	5.9	15.4	208.7	10.05	5.68E-07
	120	545	102	5.8	15.1	345.4	25.09	1.97E-09
	121	456	90	6.2	13.7	270.8	11.09	1.92E-09
	122	269	64	6.3	7.3	274.5	25.72	1.29E-05
	123	995	127	6.7	24	316.5	3.68	1.70E-06

Table B.1.2 – Metadata of Conditional Scenario Spectra set for interface subduction earthquakes.

HazLevel	Index	RSN	EqID	Mag	Rrup	Vs30	Scale Factor	Rate
1	1	6001396	6000079	8.1	106.9	382	0.33	1.60E-02
	2	6001802	6000149	8.8	134.9	495	0.06	2.37E-04
	3	4022913	4000068	8.3	60.5	230.2	0.05	1.19E-04
	4	7004772	7000044	7.1	74.9	266	0.21	3.85E-04
	5	6001799	6000149	8.8	30.4	303	0.08	2.38E-04
	6	6001813	6000149	8.8	36.5	278	0.04	4.19E-04
	7	4022990	4000068	8.3	91.7	372.4	0.46	1.70E-05
	8	4022901	4000068	8.3	157.6	355.5	1.18	4.97E-05
	9	6001825	6000149	8.8	59.1	465	0.11	3.94E-04
	10	6001817	6000149	8.8	65.3	345	0.09	6.68E-04
2	11	4028574	4000068	8.3	92.9	324.3	0.52	4.12E-06
	12	6001396	6000079	8.1	106.9	382	0.72	5.51E-03
	13	3001955	3000271	8	18.4	392	0.40	3.45E-04
	14	6001802	6000149	8.8	134.9	495	0.13	3.16E-04
	15	4032570	4000068	8.3	191.5	337.4	1.68	2.92E-04
	16	4022913	4000068	8.3	60.5	230.2	0.10	1.16E-03
	17	6001378	6000079	8.1	227.6	414	2.01	1.90E-04
	18	4028634	4000068	8.3	197.6	341.4	2.72	3.16E-04
	19	6001799	6000149	8.8	30.4	303	0.17	4.14E-04

HazLevel	Index	RSN	EqID	Mag	Rrup	Vs30	Scale Factor	Rate
	20	4032552	4000068	8.3	60.3	451.1	0.29	1.48E-05
	21	6001825	6000149	8.8	59.1	465	0.25	2.58E-04
	22	6001817	6000149	8.8	65.3	345	0.20	3.94E-04
	23	6002254	6000338	8.3	206	479	2.04	4.69E-05
3	24	6001396	6000079	8.1	106.9	382	1.53	3.86E-04
	25	3001955	3000271	8	18.4	392	0.84	8.01E-06
	26	6001802	6000149	8.8	134.9	495	0.27	1.84E-04
	27	4032570	4000068	8.3	191.5	337.4	3.33	4.72E-05
	28	4022913	4000068	8.3	60.5	230.2	0.20	7.65E-04
	29	3001968	3000272	7.6	24.4	392	1.03	5.28E-05
	30	6001378	6000079	8.1	227.6	414	3.72	4.23E-07
	31	4028634	4000068	8.3	197.6	341.4	4.97	1.58E-05
	32	6001799	6000149	8.8	30.4	303	0.30	2.16E-05
	33	6001813	6000149	8.8	36.5	278	0.15	3.60E-04
	34	4022990	4000068	8.3	91.7	372.4	1.68	4.12E-05
	35	6001825	6000149	8.8	59.1	465	0.40	8.89E-05
	36	6001817	6000149	8.8	65.3	345	0.31	3.08E-04
	37	6002254	6000338	8.3	206	479	3.11	1.49E-05
4	38	6001396	6000079	8.1	106.9	382	2.31	1.57E-04
	39	6001802	6000149	8.8	134.9	495	0.41	8.68E-05
	40	4022913	4000068	8.3	60.5	230.2	0.30	3.44E-04
	41	3001968	3000272	7.6	24.4	392	1.52	5.13E-06
	42	6001799	6000149	8.8	30.4	303	0.44	6.49E-05
	43	6001813	6000149	8.8	36.5	278	0.22	1.54E-04
	44	4022990	4000068	8.3	91.7	372.4	2.42	2.20E-05
	45	4022901	4000068	8.3	157.6	355.5	6.01	4.90E-06
	46	6001825	6000149	8.8	59.1	465	0.57	3.28E-05
	47	6001817	6000149	8.8	65.3	345	0.45	2.05E-04
	48	6002254	6000338	8.3	206	479	4.41	4.10E-05
5	49	6001396	6000079	8.1	106.9	382	3.30	7.02E-05
	50	6001802	6000149	8.8	134.9	495	0.59	3.47E-05
	51	4022913	4000068	8.3	60.5	230.2	0.43	2.08E-04
	52	6001799	6000149	8.8	30.4	303	0.64	1.44E-05
	53	6001813	6000149	8.8	36.5	278	0.32	1.21E-04
	54	4022990	4000068	8.3	91.7	372.4	3.57	6.46E-06
	55	6001825	6000149	8.8	59.1	465	0.85	1.43E-05
	56	6001817	6000149	8.8	65.3	345	0.67	6.73E-05
	57	6002254	6000338	8.3	206	479	6.58	2.53E-05
6	58	6001396	6000079	8.1	106.9	382	4.84	1.90E-05
	59	6001802	6000149	8.8	134.9	495	0.85	6.76E-06
	60	4032570	4000068	8.3	191.5	337.4	10.25	8.50E-07
	61	4022913	4000068	8.3	60.5	230.2	0.61	6.66E-05
	62	6001799	6000149	8.8	30.4	303	0.89	9.02E-06
	63	6001813	6000149	8.8	36.5	278	0.44	3.30E-05
	64	4022990	4000068	8.3	91.7	372.4	4.80	4.83E-06
	65	4022901	4000068	8.3	157.6	355.5	11.85	4.97E-07
	66	6001825	6000149	8.8	59.1	465	1.12	8.39E-06
	67	6001817	6000149	8.8	65.3	345	0.88	3.55E-05
	68	6002254	6000338	8.3	206	479	8.61	1.69E-05
7	69	6001396	6000079	8.1	106.9	382	6.32	7.03E-06
	70	6001802	6000149	8.8	134.9	495	1.11	2.64E-06
	71	4022913	4000068	8.3	60.5	230.2	0.80	3.05E-05
	72	6001799	6000149	8.8	30.4	303	1.15	6.60E-06
	73	6001813	6000149	8.8	36.5	278	0.57	2.90E-05

HazLevel	Index	RSN	EqID	Mag	Rrup	Vs30	Scale Factor	Rate
	74	4022990	4000068	8.3	91.7	372.4	6.18	1.64E-07
	75	6001825	6000149	8.8	59.1	465	1.44	6.37E-06
	76	6001817	6000149	8.8	65.3	345	1.12	1.09E-05
	77	6002254	6000338	8.3	206	479	11.02	1.29E-05
8	78	6001396	6000079	8.1	106.9	382	8.14	1.24E-06
	79	6001802	6000149	8.8	134.9	495	1.43	2.39E-06
	80	4022913	4000068	8.3	60.5	230.2	1.04	9.50E-06
	81	6001799	6000149	8.8	30.4	303	1.51	7.59E-07
	82	6001813	6000149	8.8	36.5	278	0.75	2.77E-05
	83	4022990	4000068	8.3	91.7	372.4	8.24	3.14E-07
	84	6001825	6000149	8.8	59.1	465	1.93	2.78E-06
	85	6001817	6000149	8.8	65.3	345	1.51	7.04E-06
	86	6002254	6000338	8.3	206	479	14.86	2.22E-06
9	87	6001396	6000079	8.1	106.9	382	10.85	1.16E-06
	88	6001802	6000149	8.8	134.9	495	1.90	1.38E-07
	89	4022913	4000068	8.3	60.5	230.2	1.36	6.27E-06
	90	3001968	3000272	7.6	24.4	392	6.84	7.87E-07
	91	6001813	6000149	8.8	36.5	278	0.96	3.85E-06
	92	4022990	4000068	8.3	91.7	372.4	10.36	7.20E-07
	93	4032552	4000068	8.3	60.3	451.1	2.90	2.67E-07
	94	6001825	6000149	8.8	59.1	465	2.40	2.60E-07
	95	6001817	6000149	8.8	65.3	345	1.87	1.57E-06
	96	6002254	6000338	8.3	206	479	18.32	6.96E-09
10	97	6001396	6000079	8.1	106.9	382	13.36	5.39E-06
	98	6001802	6000149	8.8	134.9	495	2.33	4.21E-07
	99	4032570	4000068	8.3	191.5	337.4	27.93	3.06E-07
	100	7004772	7000044	7.1	74.9	266	7.45	8.78E-07
	101	3001968	3000272	7.6	24.4	392	8.39	2.09E-06
	102	6001813	6000149	8.8	36.5	278	1.17	1.67E-06
	103	4022990	4000068	8.3	91.7	372.4	12.65	6.88E-06
	104	4032552	4000068	8.3	60.3	451.1	3.54	1.06E-08
	105	6001817	6000149	8.8	65.3	345	2.28	3.02E-06
	106	6002254	6000338	8.3	206	479	22.32	4.78E-06

Table B.1.3 – Metadata of Conditional Scenario Spectra set for intraslab subduction earthquakes.

HazLevel	Index	RSN	EqID	Mag	Rrup	Vs30	Scale Factor	Rate
1	1	4032461	4000092	7.6	141.7	262.3	0.46	2.12E-04
	2	2000889	2000014	6.6	43.2	362	0.46	1.65E-03
	3	5001515	5000150	6.7	219.2	555	4.90	1.79E-03
	4	3001523	3000188	6.5	100.1	429	2.27	1.56E-03
	5	7006532	7000049	6.9	35	381.2	0.23	5.14E-04
	6	5003989	5000274	6.1	50.3	700	0.31	3.86E-03
	7	7005096	7000045	6.6	151.7	597.1	4.16	2.10E-03
	8	2000905	2000014	6.6	43.2	362	0.67	2.29E-03
	9	2000062	2000004	6.8	159.4	333	3.64	2.06E-03
	10	7005904	7000048	7	137.9	508	4.18	1.51E-03
	11	4032632	4000092	7.6	263.7	254	0.58	2.42E-03
	12	4032460	4000092	7.6	107.3	260.2	0.06	1.26E-03
2	13	4032461	4000092	7.6	141.7	262.3	0.83	3.84E-04
	14	2000889	2000014	6.6	43.2	362	0.84	5.68E-04
	15	5001515	5000150	6.7	219.2	555	8.87	6.46E-04

HazLevel	Index	RSN	EqID	Mag	Rrup	Vs30	Scale Factor	Rate
	16	5001497	5000150	6.7	158.3	200	4.15	2.45E-04
	17	3001523	3000188	6.5	100.1	429	4.10	2.38E-04
	18	5003989	5000274	6.1	50.3	700	0.57	3.30E-03
	19	7005096	7000045	6.6	151.7	597.1	7.52	5.36E-04
	20	2000905	2000014	6.6	43.2	362	1.22	3.26E-04
	21	2000062	2000004	6.8	159.4	333	6.58	5.20E-04
	22	7005904	7000048	7	137.9	508	7.54	3.44E-04
	23	4032632	4000092	7.6	263.7	254	1.04	1.43E-04
	24	2000081	2000004	6.8	47.2	399	1.88	1.87E-04
	25	4032460	4000092	7.6	107.3	260.2	0.11	1.94E-03
	26	1000040	1000003	7.3	205.2	635	3.07	1.91E-04
3	27	4032461	4000092	7.6	141.7	262.3	1.44	1.21E-04
	28	2000889	2000014	6.6	43.2	362	1.43	9.59E-05
	29	5001515	5000150	6.7	219.2	555	14.99	2.86E-04
	30	5001497	5000150	6.7	158.3	200	6.89	1.77E-04
	31	3001523	3000188	6.5	100.1	429	6.71	4.24E-05
	32	5003989	5000274	6.1	50.3	700	0.90	6.07E-04
	33	7005096	7000045	6.6	151.7	597.1	11.54	1.57E-04
	34	2000062	2000004	6.8	159.4	333	9.78	2.40E-04
	35	7005904	7000048	7	137.9	508	11.03	8.09E-05
	36	4032632	4000092	7.6	263.7	254	1.50	2.21E-04
	37	2000081	2000004	6.8	47.2	399	2.66	4.24E-05
	38	4032460	4000092	7.6	107.3	260.2	0.15	3.11E-04
	39	1000040	1000003	7.3	205.2	635	4.22	8.29E-05
4	40	4032461	4000092	7.6	141.7	262.3	1.97	4.25E-05
	41	2000889	2000014	6.6	43.2	362	1.95	6.98E-05
	42	5001515	5000150	6.7	219.2	555	20.35	7.80E-05
	43	5001497	5000150	6.7	158.3	200	9.33	1.06E-04
	44	3001523	3000188	6.5	100.1	429	9.06	1.04E-05
	45	5003989	5000274	6.1	50.3	700	1.21	2.67E-04
	46	7005096	7000045	6.6	151.7	597.1	15.40	4.56E-05
	47	2000905	2000014	6.6	43.2	362	2.45	2.35E-05
	48	2000062	2000004	6.8	159.4	333	12.98	8.80E-05
	49	7005904	7000048	7	137.9	508	14.59	6.51E-05
	50	4032632	4000092	7.6	263.7	254	1.97	1.47E-04
	51	2000081	2000004	6.8	47.2	399	3.50	3.70E-05
	52	4032460	4000092	7.6	107.3	260.2	0.20	2.90E-04
	53	1000040	1000003	7.3	205.2	635	5.51	2.10E-05
5	54	4032461	4000092	7.6	141.7	262.3	2.59	1.86E-05
	55	2000889	2000014	6.6	43.2	362	2.57	4.96E-05
	56	5001515	5000150	6.7	219.2	555	26.88	3.26E-05
	57	5001497	5000150	6.7	158.3	200	12.35	3.87E-05
	58	3001523	3000188	6.5	100.1	429	12.02	1.38E-05
	59	5003989	5000274	6.1	50.3	700	1.61	1.12E-04
	60	7005096	7000045	6.6	151.7	597.1	20.63	2.37E-05
	61	2000062	2000004	6.8	159.4	333	17.48	2.58E-05
	62	7005904	7000048	7	137.9	508	19.70	4.44E-05
	63	4032632	4000092	7.6	263.7	254	2.67	3.43E-05
	64	2000081	2000004	6.8	47.2	399	4.75	1.45E-05
	65	4032460	4000092	7.6	107.3	260.2	0.27	1.97E-04
	66	1000040	1000003	7.3	205.2	635	7.52	2.47E-05
6	67	4032461	4000092	7.6	141.7	262.3	3.49	7.19E-06
	68	2000889	2000014	6.6	43.2	362	3.44	2.34E-05
	69	5001515	5000150	6.7	219.2	555	35.79	2.34E-05

HazLevel	Index	RSN	EqID	Mag	Rrup	Vs30	Scale Factor	Rate
	70	5001497	5000150	6.7	158.3	200	16.35	8.78E-06
	71	3001523	3000188	6.5	100.1	429	15.83	6.93E-06
	72	5003989	5000274	6.1	50.3	700	2.10	5.33E-05
	73	7005096	7000045	6.6	151.7	597.1	26.53	6.07E-06
	74	2000905	2000014	6.6	43.2	362	4.20	2.67E-06
	75	2000062	2000004	6.8	159.4	333	22.21	2.07E-06
	76	7005904	7000048	7	137.9	508	24.89	1.32E-05
	77	4032632	4000092	7.6	263.7	254	3.35	2.19E-05
	78	4032460	4000092	7.6	107.3	260.2	0.33	4.03E-05
7	79	4032461	4000092	7.6	141.7	262.3	4.30	8.29E-07
	80	2000889	2000014	6.6	43.2	362	4.24	4.76E-06
	81	5001515	5000150	6.7	219.2	555	44.01	1.09E-05
	82	5001497	5000150	6.7	158.3	200	20.09	6.01E-06
	83	3001523	3000188	6.5	100.1	429	19.43	2.27E-06
	84	5003989	5000274	6.1	50.3	700	2.57	2.49E-05
	85	7005096	7000045	6.6	151.7	597.1	32.45	2.84E-06
	86	2000062	2000004	6.8	159.4	333	27.11	5.83E-06
	87	7005904	7000048	7	137.9	508	30.36	8.44E-06
	88	4032632	4000092	7.6	263.7	254	4.09	1.83E-05
	89	2000081	2000004	6.8	47.2	399	7.22	3.83E-06
	90	4032460	4000092	7.6	107.3	260.2	0.40	4.31E-05
	91	1000040	1000003	7.3	205.2	635	11.27	1.78E-06
8	92	4032461	4000092	7.6	141.7	262.3	5.25	2.38E-06
	93	2000889	2000014	6.6	43.2	362	5.19	2.94E-06
	94	5001515	5000150	6.7	219.2	555	54.04	3.52E-06
	95	5001497	5000150	6.7	158.3	200	24.73	1.69E-06
	96	3001523	3000188	6.5	100.1	429	23.97	2.30E-06
	97	5003989	5000274	6.1	50.3	700	3.19	1.33E-05
	98	2000062	2000004	6.8	159.4	333	33.98	6.00E-06
	99	7005904	7000048	7	137.9	508	38.15	2.13E-06
	100	4032632	4000092	7.6	263.7	254	5.15	9.13E-06
	101	4032460	4000092	7.6	107.3	260.2	0.51	1.89E-05
	102	1000040	1000003	7.3	205.2	635	14.31	7.01E-06
9	103	5001515	5000150	6.7	219.2	555	67.49	1.98E-06
	104	5003989	5000274	6.1	50.3	700	3.92	5.24E-06
	105	2000062	2000004	6.8	159.4	333	41.06	6.69E-07
	106	7005904	7000048	7	137.9	508	45.90	3.47E-06
	107	4032632	4000092	7.6	263.7	254	6.17	2.10E-06
	108	2000081	2000004	6.8	47.2	399	10.88	4.65E-07
10	109	4032461	4000092	7.6	141.7	262.3	7.81	1.56E-06
	110	2000889	2000014	6.6	43.2	362	7.69	3.38E-06
	111	5003989	5000274	6.1	50.3	700	4.62	3.82E-06
	112	7005096	7000045	6.6	151.7	597.1	58.05	1.84E-06
	113	2000905	2000014	6.6	43.2	362	9.17	3.00E-06
	114	2000062	2000004	6.8	159.4	333	48.31	4.63E-06
	115	7005904	7000048	7	137.9	508	53.98	3.00E-06
	116	4032632	4000092	7.6	263.7	254	7.25	2.35E-06
	117	2000081	2000004	6.8	47.2	399	12.78	3.85E-06
	118	4032460	4000092	7.6	107.3	260.2	0.71	1.75E-06
	119	1000040	1000003	7.3	205.2	635	19.88	3.70E-07